DEVELOPMENT OF A SOLAR FURNACE HELIOSTAT

Preyen Agasthian Perumall

In fulfilment of the academic requirements for the degree of Master of Science in Mechanical
Engineering, College of Agriculture, Engineering and Science,
University of KwaZulu-Natal.

December 2016

Supervisor: Mr. Jean-Francois Pitot de la Beaujardiere

Co-Supervisor: Dr. Michael. J. Brooks

DECLARATION 1– PLAGIARISM

I, Preyen Agasthian Perumall, declare that:

1. The research reported in this thesis, except where otherwise indicated, is my original research.

2. This thesis has not been submitted for any degree or examination at any other university.

3. This thesis does not contain other persons' data, pictures, graphs or other information, unless specifically acknowledged as being sourced from other persons.

4. This thesis does not contain other persons' writing, unless specifically acknowledged as being sourced from other researchers. Where other written sources have been quoted, then:

   a. Their words have been re-written but the general information attributed to them has been referenced

   b. Where their exact words have been used, then their writing has been placed inside quotation marks, and referenced.

5. This thesis does not contain text, graphics or tables copied and pasted from the Internet, unless specifically acknowledged, and the source being detailed in the thesis and in the References sections.

Signed: _____ Date: _____

Mr. Preyen Agasthian Perumall

As the candidate's supervisor, I have approved this dissertation for submission.

Signed: _____ Date: _____

Mr. Jean-François Pitot de la Beaujardiere

As the candidate's co-supervisor, I have approved this dissertation for submission.

Signed: _____ Date: _____

Dr. Michael Brooks

DECLARATION 2 – PUBLICATIONS

Perumall, P. A., Brooks, M. J. and Pitot de la Beaujardiere, J. P. "A New Measurement-Based Algorithm for the Temporal Resolution of the Clear-Sky Solar Resource". *R & D Journal of the South African Institute of Mechanical Engineers,* 31, pp. 27-34, (2015)

Perumall, P. A., Brooks, M. J. and Pitot de la Beaujardiere, J. P. "An Introduction to the University of KwaZulu-Natal's Solar Energy Research Amplified Flux Facility - SERAFF". *13th International Energy Conversion Engineering Conference, AIAA Propulsion and Energy Forum,* Orlando, Florida, 27-29 July, (2015)

Signed: _____ Date: _____

Mr. Preyen Agasthian Perumall

ACKNOWLEDGEMENTS

ABSTRACT

The Solar Energy Research Amplified Flux Facility (SERAFF) is the flagship project of University of KwaZulu-Natal's Group for Solar Energy Thermodynamics (GSET). SERAFF will assume an on-axis optical configuration, common in solar furnaces around the world, comprising a flat, non-imaging heliostat reflector and a paraboloidal primary concentrator. At design-point conditions, a thermal power output of approximately 5 kW is expected with a peak flux in the region of 3 MW/m^2. The facility will provide the University of KwaZulu-Natal with a platform to undertake wide-ranging research in disciplines including concentrating solar power, materials testing and processing, and solar thermochemistry, amongst others. The primary goal of this research was to design and fabricate a flat heliostat which will enable SERAFF to meet the specified thermal requirements.

The first phase of this study was to characterise the available solar resource for Durban, South Africa, where SERAFF will be installed. A statistical algorithm was developed that processes historical ground-based solar measurements to generate a continuous function that estimates clear-sky direct normal irradiance (DNI) as a function of solar time and day number over a typical year. The three-dimensional surface that results from this function is termed a temporal DNI topograph (TDT) and can be used to define solar flux input for the modelling of concentrator systems.

The heliostat dimensions are dependent on the size of the concentrator aperture it is tasked with illuminating. As such, sizing the concentrator was key. A geometrically based approximation of the maximum theoretical power output of a parabolic primary concentrator was developed. This model was used to calculate the diameter of the parabolic concentrator needed to achieve SERAFF's specified power output. The model was validated against real solar furnaces around the world and it was found that the model approximated the power output for these solar furnaces within 12% of their published power output values. Following an optical analysis and illumination study, and after taking into consideration the practical and financial constraints placed on the project, it was decided that 3 m x 3 m was the most suitable size for SERAFF's heliostat.

A finite element analysis was used in the design process to assess the survivability (under load from a worst-case wind speed of 100 km/hr) and the rigidity (under load from an operational wind speed of 20 km/hr) for the different heliostat design concepts considered. After analyses of the FEA results it was decided that a classical T-shape design with an aluminium mirror backing frame would be employed.

Fabrication of the structural components was undertaken at the department of Mechanical Engineering's workshop and assembled at a temporary site in close proximity. Consideration was given to the effect the fabrication process would have on the tracking and optical accuracy of the heliostat.

The total cost of fabrication was R91,655, exceeding the budget of R85,000 by R6,655. This was due to high import taxes paid on the slewing drive actuator and polished aluminium mirror facets. The actual cost of materials and components was R70,353 excluding the import taxes.

TABLE OF CONTENTS

LIST OF FIGURES

LIST OF TABLES

NOMENCLATURE

Symbol	Description	Unit
A	solar azimuth angle	degrees
a_0	atmospheric transmittance constant	-
a_1	atmospheric transmittance constant	-
A_h	heliostat azimuth angle	degrees
A_m	fixed monthly coefficient for ASHRAE model	-
A_{surf}	total surface area	m^2
B_m	fixed monthly coefficient for ASHRAE model	-
C	number of days in any given month	-
D	rim diameter	m
D_{month}	matrix of raw DNI values per month of a generic year	W/m^2
$D_{monthly\_average}$	matrix of average minutely DNI values for a month	W/m^2
$DNI_{measured}$	measured value of DNI	W/m^2
DNI_{minute}	6th order polynomial for DNI per minute of generic year	W/m^2
DNI_{model}	DNI value predicted by radiometric model	W/m^2
E_0	extra-terrestrial irradiance constant	W/m^2
f	focal length	m
h	site elevation	m
H	horizontal plane containing observer and central solar ray	-
k	total number of data points	-
m_f	air mass factor	-
m_k	function of solar zenith angle and pressure ratio at sea-level	-

N	day number	-
P	observer point on Cartesian coordinate system	-
P_0	standard pressure at sea-level	bar
p_1	polynomial coefficient	-
q	polynomial coefficient	-
R	actual Sun-Earth distance	km
R_{av}	average Sun-Earth distance	km
T_a	aerosol absorptance/scattering factor	-
T_b	bulk atmospheric transmittance factor	-
T_o	ozone absorption factor	-
T_r	Rayleigh scattering factor	-
t_s	solar time	minutes
T_u	uniform mixed gas factor	-
T_w	water vapor absorption factor	-
V_{air}	nominal design wind velocity	m/s
Z	solar zenith angle in ASHRAE model	degrees
α	solar elevation angle	degrees
α_h	heliostat elevation angle	degrees
δ	solar declination angle	degrees
$\theta_{incident}$	angle of incidence	degrees
$\theta_{reflected}$	angle of reflection	degrees
ρ_{air}	mass density of air	kg/m^3
σ_{slope}	slope error	mrad
$\sigma_{specular}$	specularity error	mrad

φ	latitude	degrees
ϕ	rim angle	degrees
ω	hour angle	degrees
ϑ	slope error sensitivity	MW/m^2

Subscript	**Description**
a	aerosol
av	average
f	factor
n	solar minute within a specified period
o	ozone
r	Rayleigh
s	solar
$surf$	surface
u	uniform
w	water

ACRONYMS

ASHRAE	American Society of Heating, Refrigerating and Air-Conditioning Engineers
CAD	computer aided design
CFD	computational fluid dynamics
CNC	computer numerical control
CSP	concentrating solar power
DHI	diffuse horizontal irradiance
DLR	Deutsches Zentrum für Luft- und Raumfahrt

DNI	direct normal irradiance
EOT	equation of time
FEA	finite element analysis
GHI	global horizontal irradiance
GIS	geographic information systems
GRADRAD	Greater Durban Radiometric Network
GSET	Group for Solar Energy Thermodynamics
GUI	graphical user interface
LC	longitude correction
LCT	local clock time
MBD	mean bias difference
NIP	normal irradiance pyrheliometer
NREL	National Renewable Energy Laboratory
NSTTF	National Solar Thermal Test Facility
PCD	pitch circle diameter
PSA	Plataforma Solar de Almería
PSI	Paul Scherrer Institute
RBE2	rigid body element
RMSD	root mean square difference
SABS	South African Bureau of Standards
SAURAN	South African Universities Radiometric Network
SERAFF	Solar Energy Research Amplified Flux Facility
STERG	Solar Thermal Energy Research Group
TDT	temporal DNI topograph
TMY	typical meteorological year
UKZN	University of KwaZulu-Natal

Chapter 1. Introduction

1.1 Background

Considering its outstanding solar resource, South Africa is rapidly becoming a significant player in the global concentrating solar power (CSP) landscape (Fluri, 2009). Currently, a total 600 MW in CSP plant capacity is either operational, under construction or has been earmarked for construction in the country. In addition, numerous opportunities exist for the use of high-flux solar heating in several South African industries. Table 1-1 lists information on current CSP projects in South Africa as reported by the United States National Renewable Energy Laboratory (NREL, 2016).

Table 1-1: List of CSP projects in South Africa (NREL, 2016).

Project Name	City (Province)	Technology	Capacity (MW)	Status
Bokpoort	Groblershoop (Northern Cape)	Parabolic Trough	50	Operational
Ilanga I	Upington (Northern Cape)	Parabolic Trough	100	Under Development
Kathu Solar Park	Kathu (Northern Cape)	Parabolic trough	100	Under construction
KaXu Solar One	Poffadder (Northern Cape)	Parabolic trough	100	Operational
Khi Solar One	Upington (Northern Cape)	Power tower	50	Operational
Redstone	Postmasburg (Northern Cape)	Power tower	100	Under development
Xina Solar One	Poffadder (Northern Cape)	Parabolic trough	100	Under construction

Globally, researchers and engineers are developing the scientific and engineering capabilities required to generate electricity through such CSP projects as well as the production of solar fuels, advanced materials and chemicals using solar energy. To facilitate these developments, solar furnaces are typically employed for laboratory-scale testing of associated equipment and processes (Perumall et. al, 2015a). A solar furnace can be defined as an assembly of optical components used to collect and concentrate solar irradiance to a stationary, localised area.

It is therefore of strategic importance that South Africa develops a robust high-flux solar energy research capability for it to properly exploit the available solar resource. In aid of developing such a capability, access to a solar furnace that can support experimental research is of fundamental importance. However, at present, no facility of this type exists in South Africa and a review of the literature suggests that the same can be assumed for the continent of Africa (Perumall et. al, 2015a).

In this context, the Solar Energy Research Amplified Flux Facility (SERAFF) solar furnace project was initiated at the start of 2014, by the University of KwaZulu-Natal's Group for Solar Energy Thermodynamics (GSET). The primary objective of the project was to develop a cost-effective high-flux platform capable of catering for some of the University's and, to an extent, the country's immediate experimentation needs.

1.1.1 Solar furnace operating principles

The primary purpose of a solar furnace is to concentrate incident solar irradiance to a finite area at a stationary location in a controllable manner. There are three major components of solar irradiance that can strike a horizontal flat plate placed on the surface of the earth, these are: global horizontal irradiance (GHI), diffuse horizontal irradiance (DHI) and direct irradiance. The time integrated value of irradiance (measured in W/m^2) is irradiation, measured in (J/m^2).

A solar furnace harnesses only the direct component of solar irradiance thus it must have the ability to either collect or redirect this incident direct irradiance and then concentrate it by means of some optical device. In almost all solar furnaces, certainly in the case of solar furnaces reviewed in this study, the direct component of solar irradiance is redirected by a primary reflector towards a primary concentrator. The primary reflector is called a heliostat, labelled (1) in Figure 1-1. The heliostat's purpose is to reflect direct irradiance onto the stationary concentrator aperture (2). The heliostat must be able to track the sun in either a single axis (azimuthal or elevation) or dual axis (both azimuthal and elevation) to maintain a steady reflection on the concentrator aperture throughout the sun's trajectory across the sky. The concentrator then focuses (concentrates) this sunlight onto the focal spot (3). The optical axes of the heliostat and the concentrator are collinear thus this optical configuration is said to be an on-axis configuration.
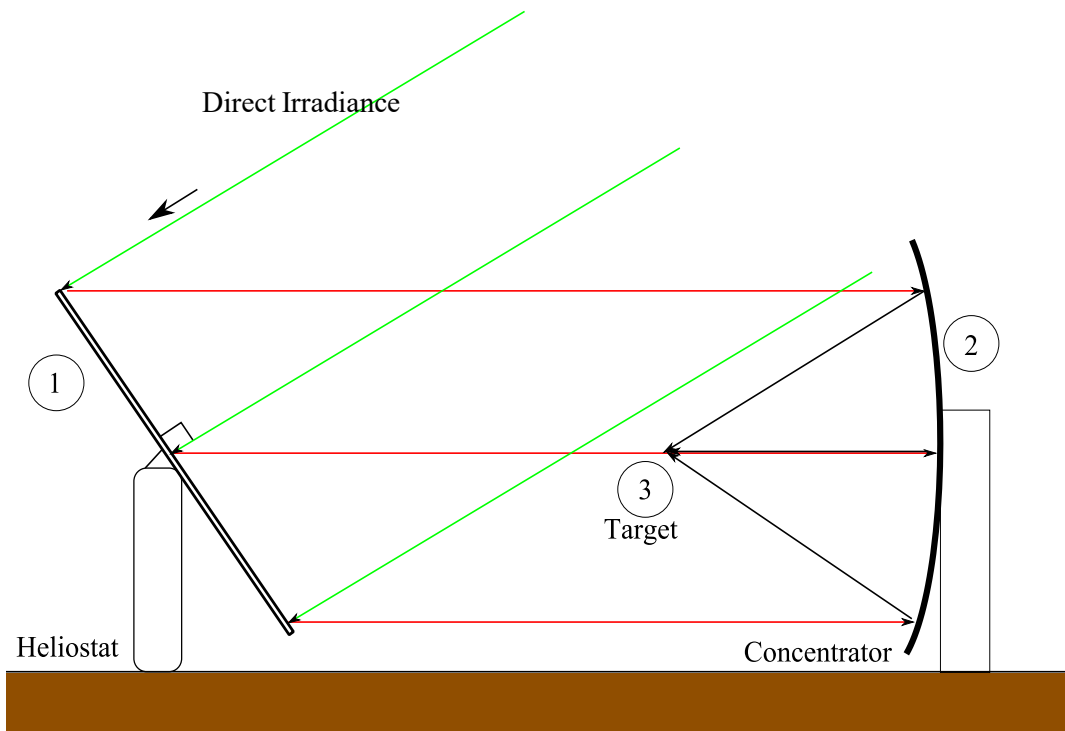
Figure 1-1: On-axis solar furnace schematic.

If the primary concentrator had the capability of tracking the sun in two axes then there would be no need for a heliostat, however, this would lead to a complex and expensive configuration for typical solar furnace applications. The heliostat is a vital component in the solar furnace for this reason and an improperly designed heliostat can result in substantial optical aberrations that reduce the overall concentration ratio of the solar furnace.

1.1.2   SERAFF specifications

It is envisaged that SERAFF will primarily support research into CSP receiver technologies, advanced materials, and solar process heating applications. There are several well-established research-based solar furnaces around the world and are each utilised in a variety of applications. Table 1-2 lists some of the characteristics and capabilities of solar furnaces around the world.

Table 1-2: Applications and capabilities of solar furnaces around the world.

Name	Primary Applications	Thermal Power (kW)	Peak Thermal Flux (MW/m²)	Reference
DLR	- Materials testing - Materials sintering - Materials treatment	28	4.5	Neumann and Grouer, 1996
PSI	- Production of solar fuels	40	5	Haueter et. al, 1999
NREL	- CSP receiver/equipment testing.	10	2.5	Steinfeld et. al, 1992
PSA	- Thermochemical processing	60	3	Fernandez-Reche et. al, 2006
Quarter Master	- Materials testing - Materials sintering - Materials treatment	27	3	Davies et. al, 1957

The thermal power output of a solar furnace is directly associated with heliostat and primary concentrator sizes, which in turn have a major bearing on facility cost. After reviewing anticipated costs and considering the impact of facility size on experimental practicality, it was decided to select a target thermal power output of 5 kW as a design specification. In relation to the values reflected in Table 1-2 it is clear that SERAFF will operate at the lower end of the spectrum (Perumall et. al, 2015a).

The peak flux of a solar furnace is predominantly dependent on concentrator optical characteristics. Poor quality optical materials and surfaces will result in low peak flux performance; however, high quality optical characteristics are expensive to attain in practice. The data in Table 2-1 suggests that a mid-range peak flux of 3 MW/m² would be sufficient to support activities in the major application categories outlined above, which are consistent with GSET's areas of interest. Figure 1-2 shows a 3D CAD rendering of SERAFF in its entirety.
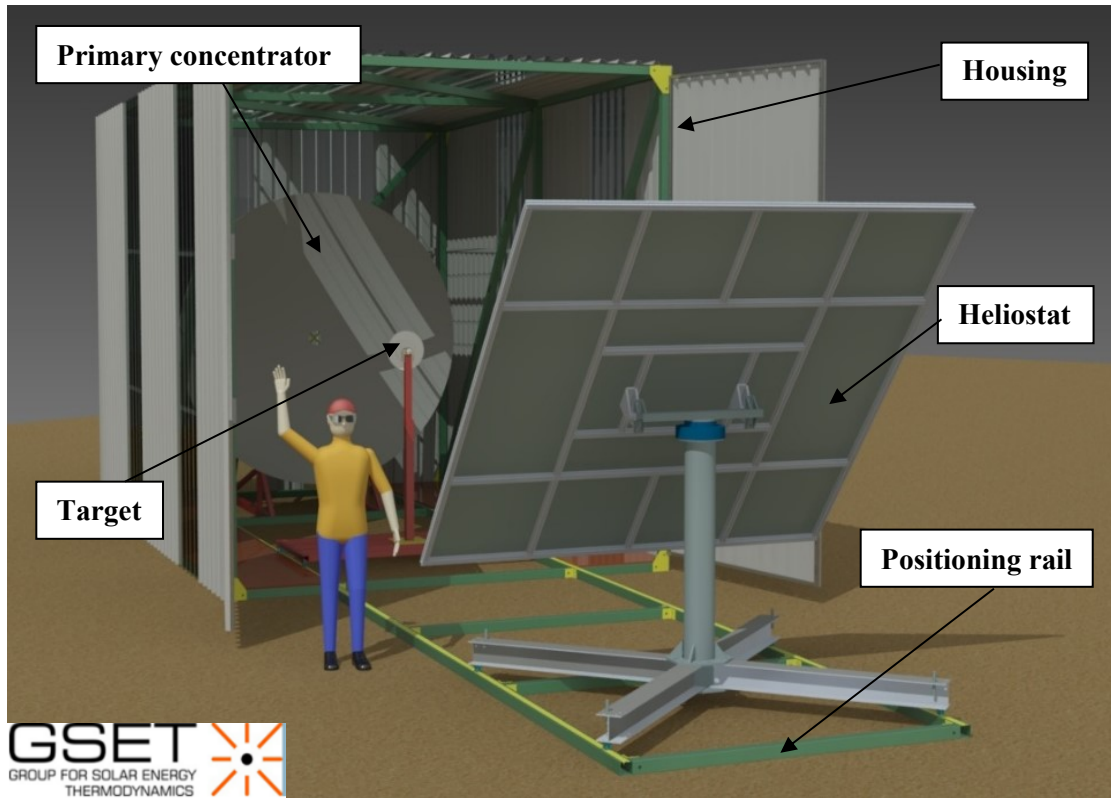
Figure 1-2: 3D CAD rendering of the proposed SERAFF confguration.

1.2 Research objectives

This study's primary objective is to design and fabricate a flat, fully functional, dual-axis sun-tracking heliostat for use in the Solar Energy Research Amplified Flux Facility at the University of KwaZulu-Natal. A heliostat design is proposed for fabrication. This study had the following research objectives:

1. Describe the optical design of a flat heliostat that would allow SERAFF to attain its desired thermal specifications.
2. Describe the mechanical design of a flat heliostat in which all design requirements are met within financial and practical constraints.
3. To fabricate, assemble and install the heliostat (within SERAFF) with consideration to the effects that these processes could have on the heliostat's tracking and optical performance.

The heliostat must track the sun whilst maintaining satisfactory illumination of the primary concentrator aperture, thus a dual-axis tracking algorithm was employed and integrated into a

control system. Further research aims added to the function and structure of the control system include:

4. Real-time calculation of the solar position vector based on an integrated solar position algorithm.
5. Utilise the solar position vector to calculate the required heliostat position (heliostat azimuth and elevation angle) and translate this heliostat position vector into executable motor control.
6. Implement closed-loop feedback control to minimise the difference in the measured heliostat position and the required heliostat position.
7. A simple prototype user-interface needed to be developed to operate the heliostat whilst displaying relevant information to the user such as current heliostat orientation, time of day inputs and graphical output of current solar position and predicted trajectory of the solar disk.

1.3 Methodology

Following on from the research objectives, the overall research methodology is summarised into the following phases:

1. Characterisation of Durban's solar resource and assessment of its suitability as a site of installation for a solar furnace facility, such as SERAFF, through a statistical approach based on historical ground-based solar measurements.
2. An investigation and review into literature highlighting different aspects of heliostat design in the context of solar furnace characteristics and thermal performance.
3. Sizing of SERAFF's parabolic concentrator using a geometrical model to predict the total power output for varying structural and optical parameters. The heliostat size was then determined based on the size of the concentrator aperture through an illumination study using optical ray tracing software (TracePro™).
4. Formulation of conceptual designs through a review of current heliostats within the CSP landscape as well as those utilised in other solar furnaces. A selection matrix was used to determine the most suitable design elements to be incorporated into the design of SERAFF's heliostat.
5. Use of finite element analysis (FEA) to determine the best performing concept under operational loading conditions as well as survivability under worst-case loading. A wind load model was used to determine the load inputs to be used in the FEA.

6. Development of final working designs. The fabrication, assembly and installation processes for the chosen heliostat design were developed and implemented.

1.4 Thesis outline

Chapter 2 describes a novel algorithm in which local radiometric ground-based measurements of direct normal irradiance was transformed into a three-dimensional temporal DNI map for Durban. The chapter outlines the mechanics of this algorithm and explains how it can be applied in the characterisation of the solar resource as well as identifying windows of operation for solar equipment that harness direct irradiance, an example being a solar furnace.

Chapter 3 details the design methodology employed in the design of the heliostat with respect to both the optical and mechanical. Along with the design of the heliostat, solar tracking is discussed and various mathematical procedures are outlined that enabled the calculation of the solar position vector as well as transforming solar azimuth and elevation angles into an ideal heliostat orientation vector.

Chapter 4 describes how the heliostat components were fabricated, assembled and installed.

Chapter 5 discusses the control system used to control the heliostat orientation based on the current solar position. The functionality of the user interface is explained.

Chapter 6 concludes the study and summarises the key results.

Chapter 2. Local solar resource characterisation

2.1 Introduction

The work presented in this chapter was taken primarily from the published journal article by Perumall et al. (2015) titled "A New Measurement-Based Algorithm for the Temporal Resolution of the Clear-Sky Solar Resource" This work formed part of the heliostat design process. The study aimed to understand and characterise Durban's clear-sky solar resource, where SERAFF and consequently the heliostat is to be operated.

For solar concentrating systems, such as CSP plants, the overall performance is characterised over a year-long period using radiometric and meteorological measurements that are representative of typical, location-specific conditions. Typical meteorological year (TMY) data files, for example, are a source of such data.

In solar concentrating equipment or systems, the direct normal component of solar irradiance provides a key input to a system performance analysis. Diurnal, seasonal and meteorological variations in direct normal irradiance (DNI) need to be captured to make an accurate estimation of energy outputs. The DNI data considered in annual analyses can therefore be termed "all-sky" DNI data, as DNI records associated with both clear and cloudy days are used to calculate the expected energy yield of the system.

On the other hand, clear-sky DNI data is a subset of all-sky DNI data that is exclusively associated with cloudless conditions. Although clear-sky DNI data are not in themselves sufficient to predict annual system performance, they are of importance in the design of solar concentrator systems and associated equipment.

Applications of clear-sky DNI data

There are numerous examples of applications of clear-sky DNI data found in literature. A few of these examples include the study performed by Bader et al. (2015) where a model is used to describe a parabolic trough tubular cavity receiver in which the clear-sky DNI is modelled for Seville, Spain, "*at the summer solstice at solar noon*" and again "*for the equinox at 8 am solar time*". The algorithm proposed here produced similar time and date-specific solar radiometric data to be used in solar concentrating studies, such as the design of a solar furnace and its primary components. In another example of cavity receiver performance simulations, by Samanes and

Garcia-Barberena (2014), utilise clear-sky DNI curves as an input to their simulations. In the absence of a clear-sky DNI prediction model they selected a run of five clean daily profiles from a Baseline Surface Radiation Network ground station in Nevada, USA, to use as the DNI input. Yilmaz and Söylemez (2014) describe a parabolic trough collector model that uses as its energy input "*a typical beam radiation measured in the summer solstice for Gaziantep (Turkey)*". Once again, their DNI input is a clear-sky profile.

Similar non-empirical methods of modelling clear-sky DNI, such as that proposed here, were employed by Huang et al. (2012) in generating specific direct normal irradiance values for parabolic trough performance simulations.

Apart from simulation studies, knowledge of site-specific clear-sky DNI is also required during the planning and execution phases of a solar furnace test programme. A practical problem that arises is structuring the test programme such that reasonable baseline DNI is available throughout the testing window at a given location, accounting for daily and seasonal variability, but excluding cloud effects. The handbook ASHRAE (1972) and the British Standard "BS EN 12975-1" (2006) stipulate irradiance levels required during collector evaluation, so knowledge of the clear-sky DNI is essential. For example, Brooks (2005) used a solar position algorithm to generate a graph of incidence angles covering the period of a parabolic trough test programme in Durban.

Solar furnaces typically operate under clear-sky conditions with high DNI level and minimal disruption by cloud. To appropriately schedule test campaigns, it is important to be able to forecast the clear-sky DNI resource available at the facility's location at any time during the year. This is because the diurnal and seasonal variation of this parameter impacts directly upon the nature of and duration over which testing can be conducted in the context of minimum threshold values.

An established approach to provide such forecasts is the use of clear-sky radiative models which estimate clear-sky DNI as a function of time and location, based upon attenuation parameters. Whilst these models are quite simple and are not generally reliant upon ground-based measurements, the uncertainty associated with their predictions is typically high. For high-fidelity system design and performance calculations, this level of uncertainty is not desirable.

The difficulties associated with the processing and subsequent visualization of ground based measurements (logged once every minute) was considered in the development of this model. In particular, the development of a novel algorithm for formulating a continuous function describing the daily and seasonal variation of clear-sky DNI based on such data is detailed.

The algorithm is implemented to derive TDT models for Durban and Stellenbosch, and the value of the information revealed by these models is illustrated in the specific context of considerations associated with solar furnace operation. In addition, the TDT results derived above are compared on a statistical basis to predictions made by a variety of clear-sky radiative models, allowing the fidelity and applicability of these models to be evaluated. Finally, the effectiveness of using TDT models to tune the attenuation parameters of one such radiative model to enhance its prediction accuracy is also demonstrated.

2.2 Methodology

The following sections of this chapter will detail the method in which the TDT was derived for both Durban and Stellenbosch. It was useful to compare Durban's TDT with that of another South African location to evaluate the sensitivity of the technique to climate. The validity of the model can be supported by analysing the trends observed in TDT's representing both Durban and Stellenbosch. Also, a statistical comparison is made between the model presented here and other clear-sky radiative models.

2.2.1 Measurement of DNI

The temporal DNI topographs were obtained from measurements of down-welling short-wave irradiance taken by instruments located at two ground stations. The Durban station is located at the University of KwaZulu-Natal's Howard College campus and includes an Eppley Laboratory Normal Incidence Pyrheliometer (NIP) (serial # 35649E6) and a Kipp and Zonen CHP1 pyrheliometer (serial # 120791) for DNI measurement. The NIP has measurement uncertainty of approximately 1.5 to 2%. The CHP1 exhibits similar but slightly lower uncertainties. Most of the Durban data used in this study were obtained from the GRADRAD archive (Kunene et al., 2013). The Stellenbosch data was measured using a Kipp and Zonen CHP1 (Serial # 100235) and downloaded from the SAURAN website (SAURAN, 2014). Data used in the study were recorded as minute-averaged values between the year 2010 and 2013 at both sites.

The data process flow for the study are given in Figure 2-1. Blocks (A) to (D) illustrate the steps followed in acquiring and preparing the raw DNI data and blocks (E) to (G) represent the processing required to generate the temporal DNI topographs.
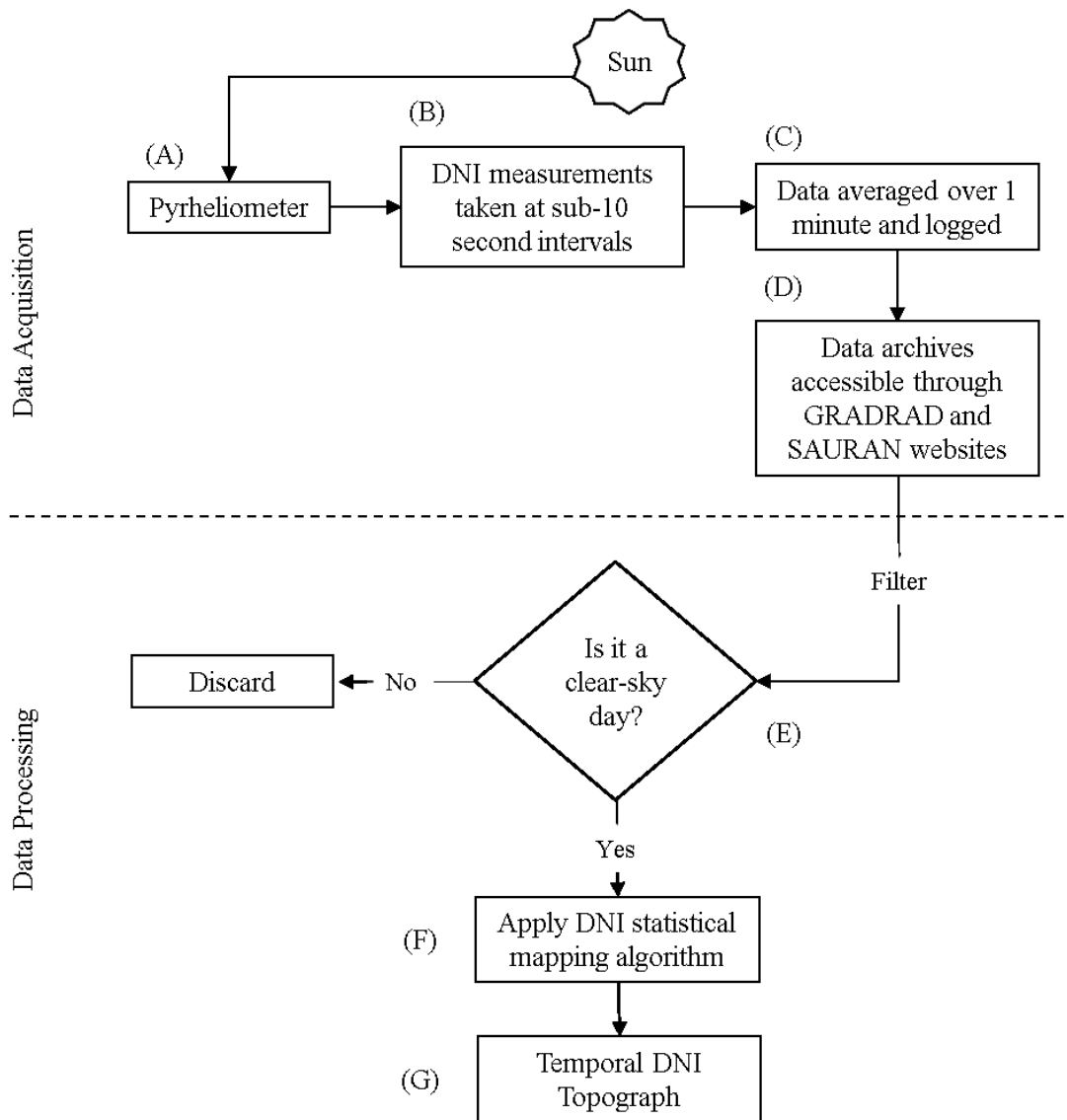
Figure 2-1: Overview of DNI measurement data flow.

2.2.2 Extraction of clear-sky data

Block (E) of Figure 2-1 represents a screening process in which the raw DNI data files for each day were categorised as either clear or cloudy. The filtering process was done by visual inspection of DNI as a function of solar time for each day. Clear-sky days exhibit the typical profile shown in red in Figure 2-2, which displays the DNI measured on the vertical axis and the normalised solar time (as a fraction of a 24-hour period) on the horizontal axis. Partly cloudy days produce significant stochastic variation in the data trace, as shown in blue in Figure 2-2. Although visual inspection is somewhat subjective, it is commonly used in radiometric studies (Salazar and Raichijk, 2014) and was applied here to isolate days with radiometric profiles consistent with the clear-sky day in Figure 2-2.

Once the database of clear-sky days was formed, the more complex task of transforming the measurements into a useful representation of sun strength spanning a full calendar-year was undertaken.
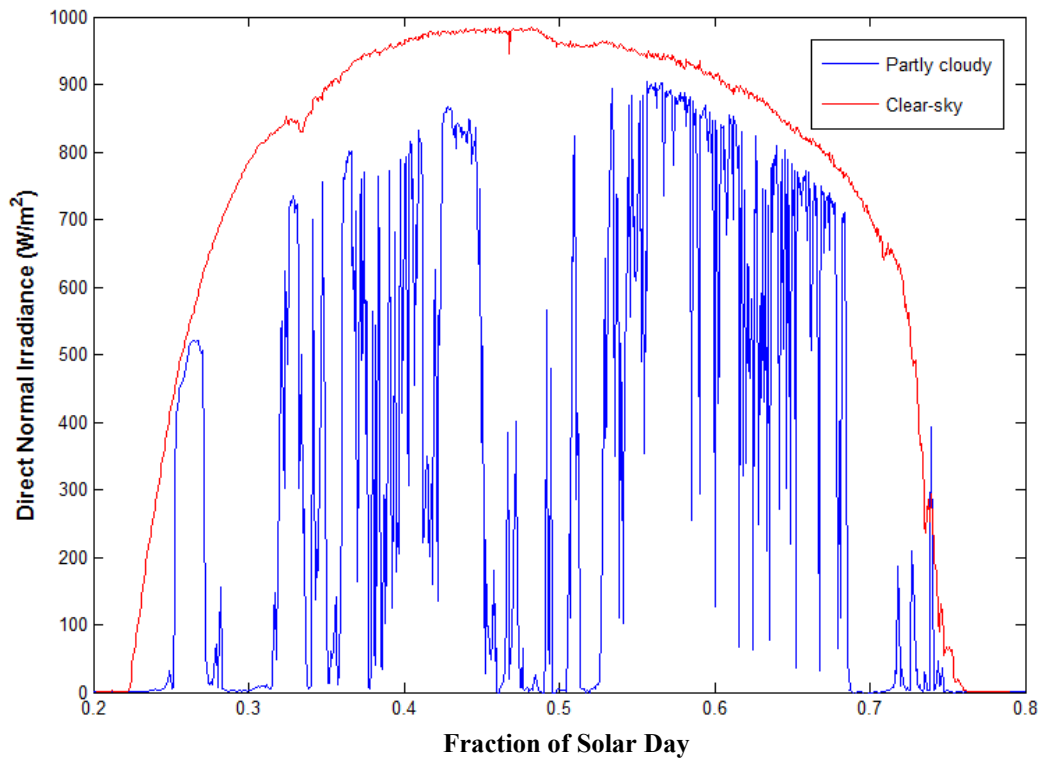
Figure 2-2: Comparative traces of DNI measured under clear and partly cloudy sky conditions.

2.2.3 Temporal DNI topograph mapping algorithm

The intention of the TDT algorithm was to utilise high frequency DNI measurements to build a map correlating clear-sky DNI magnitude with daily and seasonal changes with time. This multivariate approach resulted in a three-dimensional surface or topograph of DNI that excludes partly cloudy conditions.

The number of cloud-free days in the dataset was limited by the influence of weather conditions. In total, 59 clear-sky days were used for the Durban station's analysis spanning all 12 months of a generic year. This number was increased to 96 for Stellenbosch where weather conditions result in more frequent cloud-free conditions.

The manipulation of data was undertaken using matrix-algebra, as follows. Twelve matrices were generated, one for each month (D_{month}) of a generic year. Each consisted of raw, minute-averaged values of clear-sky DNI running from 08:00 to 16:00 (solar time), that is, from solar minute 480 to solar minute 960. This period is consistent with the practical daily operating window of a specialised concentrating system, such as a solar furnace. The column entries represent all available clear-sky day numbers from 1 to a maximum of C in a particular month. This utilised all data, that is, January measurements from 2010 to 2013, all February measurements from 2010 to 2013, and so on up to and including December.

$$D_{month} = \begin{pmatrix} a_{480,1} & \cdots & a_{480,C} \\ \vdots & \ddots & \vdots \\ a_{960,1} & \cdots & a_{960,C} \end{pmatrix} \tag{a}$$

Once matrix (a) was constructed for the 12 months of the year, a second matrix was generated (b) to represent the average DNI per minute for all clear-sky days in a particular month. In essence, this is the average measured clear-sky DNI for a particular month as a function of solar time.

$$D_{monthly\_Average} = \begin{pmatrix} b_{n,1} \\ \vdots \\ b_{481,1} \end{pmatrix} \tag{b}$$

Element $b_{n,1}$ was given by equation (1), noting that $n \in (1:481)$ where $n = 1$ corresponds to 8:00AM and $n = 481$ corresponds to 16:00PM.

$$b_{n,1} = \frac{\sum_{i=1}^{C}(a_{n,i}+a_{n,i+1}+a_{n,i+2}+\cdots+a_{n,C})}{C} \tag{1}$$

A 6th order polynomial was used to curve fit the average clear-sky DNI plots for each month. A set of twelve polynomial equations were thus formed to represent the average clear sky DNI profile (DNI_{minute}) as a function of solar minute for each of the 12 months of the generic year. Equation (2) is the general form of these equations:

$$DNI_{minute} = p_1 m^6 + p_2 m^5 + p_3 m^4 + p_4 m^3 + p_5 m^2 + p_6 m + p_7 \tag{2}$$

Here m is the solar time in minutes; $m = 1$ corresponds to 08:00 and p_1 to p_7 are the polynomial coefficients.

These 12 equations were assembled around the mean day number of that month to achieve an unbiased average clear-sky DNI per minute for that month. The MATLAB™ software package (MATLAB User Guide, 2014) was used to interpolate between the 12 equations using a 6th order polynomial. This produced a new set of equations of the form given in equation (3), to approximate clear-sky DNI explicitly as a function of day number (*N*) and implicitly as a function of solar time. These equations were used to generate the TDT.

$$DNI = q_1 N^6 + q_2 N^5 + q_3 N^4 + q_4 N^3 + q_5 N^2 + q_6 N + q_7 \tag{3}$$

2.2.4 Temporal DNI topograph

A mapping algorithm was used to generate the TDT showing both seasonal and daily variations in clear-sky DNI. Figure 2-3 and Figure 2-4 give the resulting temporal DNI topographs for Durban and Stellenbosch, respectively.
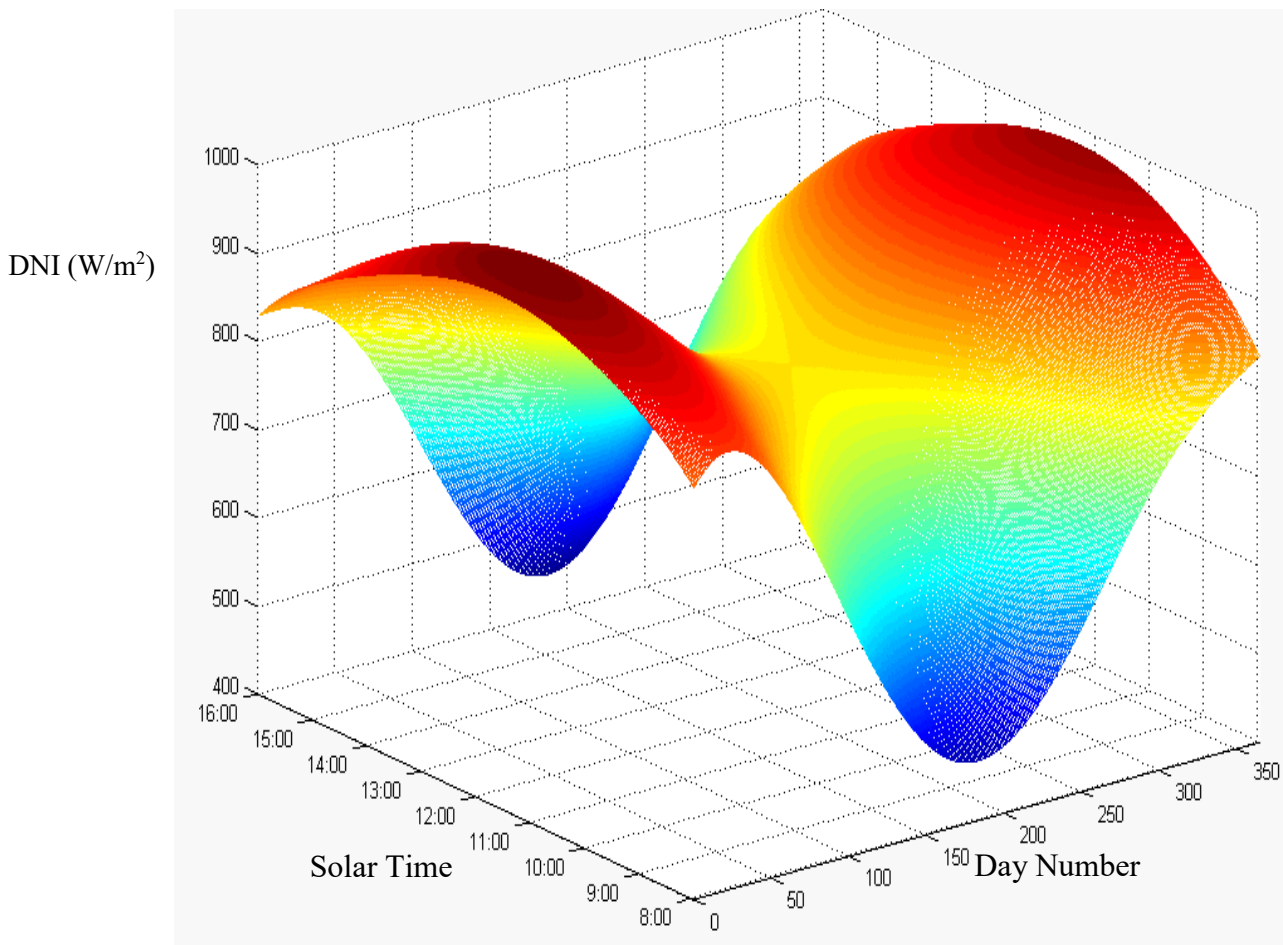
Figure 2-3: Temporal DNI topograph for Durban.
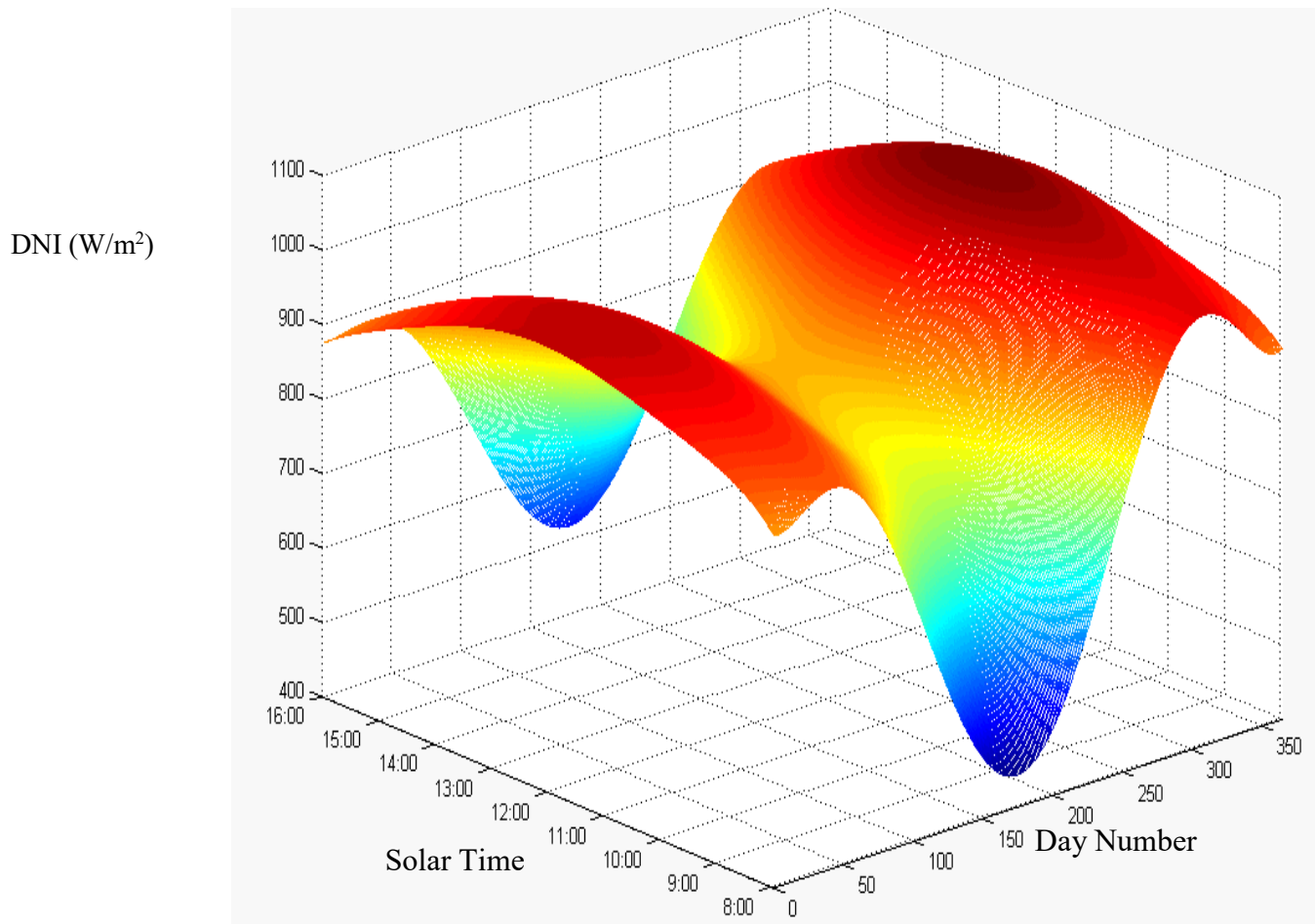
Figure 2-4: Temporal DNI topograph for Stellenbosch.

Stellenbosch receives, on average, higher levels of clear-sky DNI throughout the year. This is consistent with the different weather patterns experienced at each site. As expected, both receive maximum clear-sky DNI in summer and minimum levels in winter as indicated by the depression in the saddle-shaped TDT. With minimal further analysis, the map can be used to identify the range of days throughout the year in which a solar furnace or any concentrating solar equipment can be run if a minimum DNI threshold must be exceeded. This is not possible with spatial or annually-averaged all-sky DNI maps, nor is it easily achievable using data from conventional solar resource assessment studies. As well as enabling the observation of seasonal variations, the map also allows the observation of daily variability, which is useful in gauging an optimum window of operation for solar concentrators. Cross sections of the map illustrate the usefulness of the TDT in identifying solar irradiance trends and limits, as shown in Figure 2-5 and Figure 2-6.
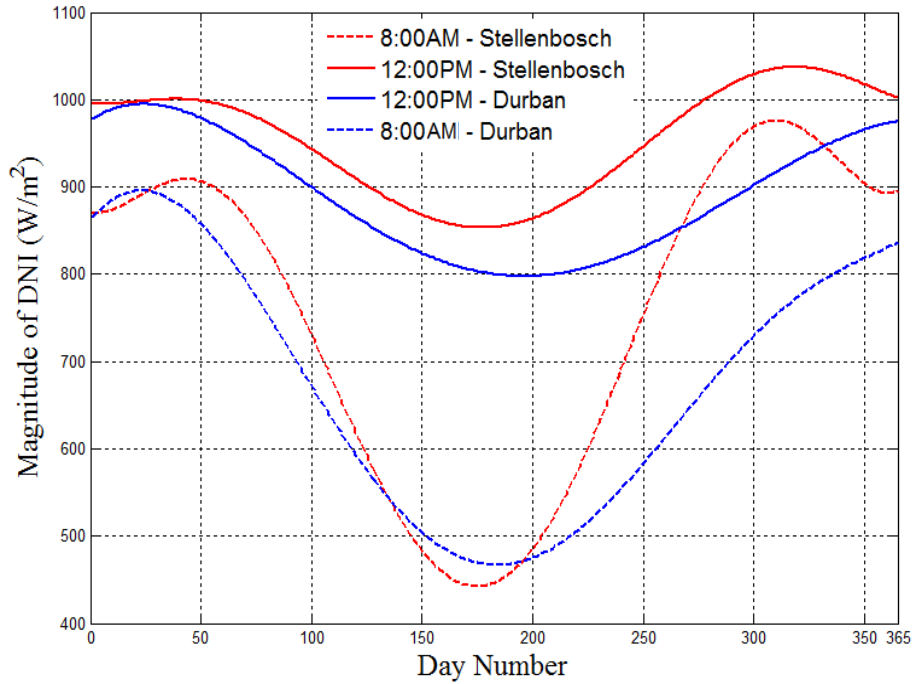
Figure 2-5: TDT cross-section for 08:00 and 12:00 at Durban and Stellenbosch showing seasonal variation.
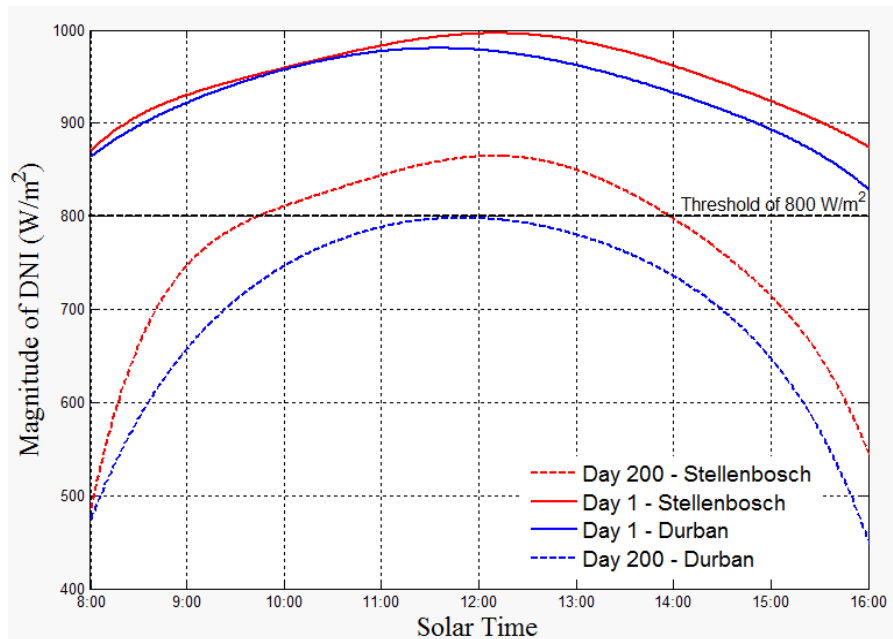
Figure 2-6: TDT cross-section taken for Day 1 (summer) and Day 200 (winter) for Durban and Stellenbosch showing daily variation.

Among other trends, Figure 2-6 shows the steeper seasonal gradient in clear-sky DNI at 08:00 for both Durban and Stellenbosch versus that at 12:00. This illustrates the reduced operational window for SERAFF, which must be operated nearer to solar noon as winter approaches, for the hypothetical case of an 800 W/m^2 flux threshold. Summer offers the opportunity for an earlier

16

start in the morning. Figure 2-6 gives the daily variation for Day 1 (summer day) and Day 200 (winter Day). In early January, there are more hours available in which to run SERAFF, with respect to the flux threshold, as compared to Day 200 where there are fewer hours available that meet or exceed this threshold. In the case of Durban for Day 200, it is unlikely that SERAFF would achieve the thermal flux corresponding to the hypothetical DNI threshold at any time of the day.

Apart from inspecting cross-sections of the TDT, a more powerful application would be to use the individual clear-sky DNI points, which make up the mapped surface, as inputs to an optical system model. This can be a model simulating the optical behaviour of any specialised solar concentrating equipment that harnesses DNI.

In this case, the TDT can be directly applied to the design of a solar furnace such as SERAFF. For instance, it would prove useful to apply the temporal map to an optical model of the heliostat, where, for example, the total collected aperture irradiance over the course of a day is to be considered – specifically during the window of operation.

2.2.5 Clear-sky radiative models

In the absence of ground-based radiometric measurements, solar energy design engineers may use one of the many clear-sky radiative models to estimate the local solar resource (Gueymard, 2012b). These are time and location-dependent and can therefore provide the estimated energy input to solar concentrator performance analyses for different sites. An obvious drawback is that they carry uncertainties in comparison to measured data that compromise the fidelity of equipment performance simulations results. In some cases, a radiometric model may need to be tuned to a specific site to improve its accuracy. Four such models are therefore included in this study to illustrate the improvement in clear-sky DNI prediction that might be expected from the empirically derived TDT.

The most accurate clear sky models are based on the attenuation of solar irradiance by scattering and absorption as sunlight traverses the atmosphere to the ground (Bird and Hulstrom, 1981). Their statistical uncertainty is therefore related to their complexity and generally also to the number of inputs to the model. As an example of the general form, Bird and Hulstrom (1981) proposed the following model of beam irradiance.

$$\text{DNI} = E_0 \cdot 0.9662 \cdot T_r \cdot T_a \cdot T_w \cdot T_0 \cdot T_u \qquad (4)$$

Here T_r, T_a, T_w, T_0 and T_u are transmittance factors that describe Rayleigh scattering, aerosol absorptance/scattering, water vapor absorption, ozone absorption and uniformly mixed gas absorption, respectively. E_0 is the extra-terrestrial irradiance at the mean Earth-Sun distance. These factors are not easily obtained for a site without a ground-based measurement station, and their use in concentrator performance modelling and design is therefore problematic. Simpler models eliminate the problem and there are several in common use.

2.2.6 Selected radiative models

Four clear-sky models that require fewer measured inputs than the attenuation variety are those presented in ASHRAE (1972), Fu and Rich (1999), Hottel (1976) and Kumar (1997).

These models were applied to estimate clear-sky DNI for Durban and Stellenbosch for comparison with their TDT maps presented in this study. To demonstrate the usefulness of the TDT algorithm, the model proposed by Fu and Rich is tuned to local conditions so that it more accurately represents the clear-sky DNI resource for Durban and Stellenbosch. This includes adjusting the bulk atmospheric transmittance parameter as determined by the TDT analysis.

The chosen models require few or no atmospheric inputs. Their primary input variable is the solar zenith angle which, for the present study, was obtained at 1-minute intervals for the period of 2010 to 2013, using the US National Renewable Energy Laboratory (NREL) Solar Position Algorithm (SPA, 2014).

ASHRAE model

The ASHRAE model is used in industry to calculate solar heat gains and cooling loads in buildings and in the design of simple solar systems. It is presented in the form of a simple decaying function that is dependent on the solar zenith angle, *Z* but is independent of atmospheric data. Clear-sky DNI is obtained from:

$$DNI = A_m e^{\left(\frac{-B_m}{\cos Z}\right)} \tag{5}$$

where A_m and B_m are fixed monthly coefficients that are determined empirically (ASHRAE, 1972).

Hottel model

The model of Hottel has been successfully utilised in estimating clear-sky solar irradiances for sites around the world (Lingamgunta and Veziroglu, 2004) ;(Aziz and Gamil,1990). The direct component is obtained from:

$$DNI = E_0(a_0 + a_1 \cdot e^{-k.\sec Z}) \qquad (6)$$

The constants placed in parenthesis are collectively regarded as an atmospheric transmittance factor, where constants a_0, a_1 and k are calculated using the following equations based on the urban 5 km visibility haze model as per Hottel (1976).

$$a_0 = 0.4237 - 0.00821(6-A)^2 \qquad (7a)$$
$$a_1 = 0.5055 + 0.00595(6.5-A)^2 \qquad (7b)$$
$$k = 0.2711 + 0.01858(2.5-A)^2 \qquad (7c)$$

The atmospheric transmittance constants are functions of site altitude, *A*, only. E_0 is the extra-terrestrial irradiance given by:

$$E_0 = 1367. \left(\frac{R_{av}}{R}\right)^2 \qquad (8)$$

The ratio R_{av}/R is the ratio of the mean Sun-Earth distance to the actual sun-earth distance as a function of the day number (*N*) of the year. This ratio is obtained from the Fourier series representation of the sun's position given by Spencer (1971).

Kumar model

The model proposed by Kumar (1997) has been used in the agriculture and ecology sectors to estimate solar irradiance (Spadavecchia et al., 2008). Clear-sky DNI is obtained as follows:

$$DNI = 0.56. E_0. (e^{-0.65.m_k} + e^{-0.095.m_k}) \qquad (9)$$

where the term m_k is given by:

$$m_k = \left(\frac{p}{p_0}\right)[(1229 + (614\cos Z)^2)^{0.5}614\cos Z) \qquad (10)$$

The term m_k is a function of the solar zenith angle and the ratio of local barometric pressure to standard pressure at sea level, p/p_0. For this study, this ratio was set to unity because Durban and Stellenbosch are situated close to sea level. As a check on this assumption, model sensitivity was tested by applying a variable pressure ratio to equation (10), based on meteorological data for multiple clear-sky days. The resulting clear-sky DNI estimations were shown to exhibit no significant difference as compared to approximations with an assumed pressure ratio of 1.

Fu and Rich model

The clear-sky model proposed by Fu and Rich (1999) was developed for Geographic Information Systems (GIS) applications. The model requires only solar zenith angle and site elevation. Clear-sky DNI is obtained from:

$$DNI = E_0 . T_b{}^{m_f} \tag{11}$$

where T_b is the bulk atmospheric transmittance factor with a recommended value of 0.5, and air mass factor, given by:

$$m_f = \frac{e^{(-0.000118.h - 1.638x10^{-9}.h^2)}}{cosZ} \tag{12}$$

The air mass factor is a function of solar zenith angle and the site elevation, h in meters.

2.2.7 Three-dimensional temporal DNI maps based on radiative model approximations

In this section, the DNI topographs derived from pyrheliometric ground-based measurement are compared to similar surfaces generated using artificial clear-sky DNI data from the radiative models. This is useful in highlighting the models' failure to capture physical trends in the local solar resource, versus the empirically-based TDTs.

Figure 2-7 and Figure 2-8 show individual maps generated using the models mentioned, as well as the TDT illustrated in Section 2.2.4
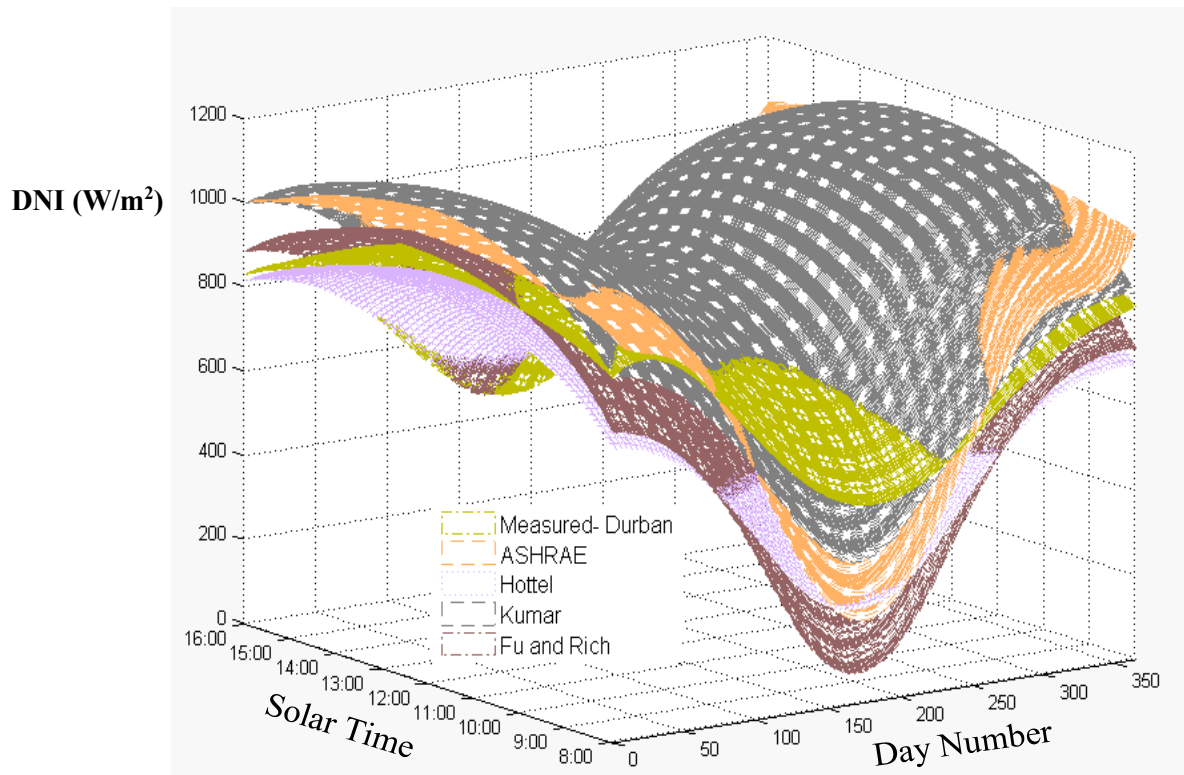
Figure 2-7:Comparison of model-generated surfaces and the empirically derived TDT for Durban.
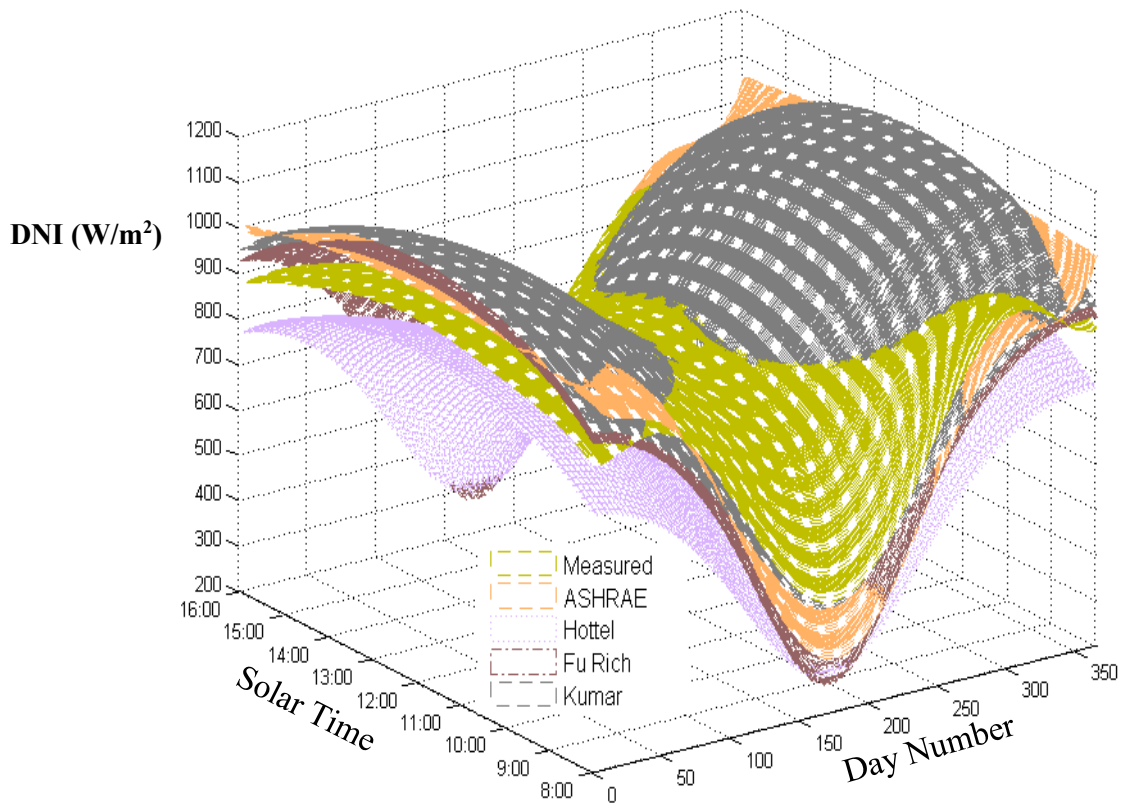
Figure 2-8: Comparison of model-generated surfaces and the empirically derived TDT for Stellenbosch.

Upon inspection, the modelled maps and measured maps show fairly tight grouping and in some instances, overlap one another. The general 'saddle' shape is exhibited for all instances of the modelled maps, as expected.

2.2.8 Mean bias difference and root mean square difference

The differences between the modelled and measured maps are quantified statistically using the mean bias difference (MBD) and the root mean square difference (RMSD). Table 2-1 gives the cumulative RMSD and MBD values, expressed as a percentage of the mean measured irradiance in W/m^2, and derived as follows:

$$\text{MBD} = \frac{\sum_{i=1}^{k}(DNI_{model,i} - DNI_{measured,i})}{k} \tag{13}$$

$$\text{RMSD} = \sqrt{\frac{\sum_{i=1}^{k}(DNI_{model,i} - DNI_{measured,i})^2}{k}} \tag{14}$$

Where DNI_{model} and $DNI_{measured}$ are, the predicted and measured clear-sky DNI magnitudes for each interval (i), respectively. The variable k represents the total number of data points used in the calculation. For example, for a seasonal (or per day) analysis, $k = 365$, whereas for a daily (or per minute) analysis, $k = 480$.

Table 2-1: Annual cumulative MBD and RMSD statistics for Durban and Stellenbosch.

#	Model	Durban		Stellenbosch	
		MBD (%)	RMSD (%)	MBD (%)	RMSD (%)
1	ASHRAE	+6.8	9.8	-2.7	8.1
2	Hottel	-6.5	8.1	-15.9	16.9
3	Kumar	+13.8	15.3	+3.2	6.7
4	Fu and Rich	-0.4	10.2	-0.3	6.7

The bulk atmospheric transmittance factor (T_b) associated with equation (11) cannot be determined independently of atmospheric data, therefore a recommended default value of 0.5 is given in the literature (Gueymard, 2012a). The MBD based on the entire dataset, for model 4, is

minimised such that it approaches zero as the bulk atmospheric transmittance factor goes to unity. By minimizing the MBD, a value of T_b for both Durban and Stellenbosch was found, alternate to the default value given in literature. The value of T_b for both Durban and Stellenbosch is 0.72 and 0.77, respectively. The mean bias difference of model 4 is considerably lower than those of models 1, 2 and 3 for Durban and Stellenbosch as the model was tuned to these specific locations against the measured TDT.

Models 1 and 2 perform similarly for Durban, but largely differ for Stellenbosch. This could be due to Model 2's dependence on the haze model of equation (7) where various atmospheric parameters are approximated.

Although the cumulative statistics indicate a measure of error over the entire dataset, it is instructive to investigate the performance of the models at each minute and over an entire day. These statistics appear in Figure 2-9 to Figure 2-16.
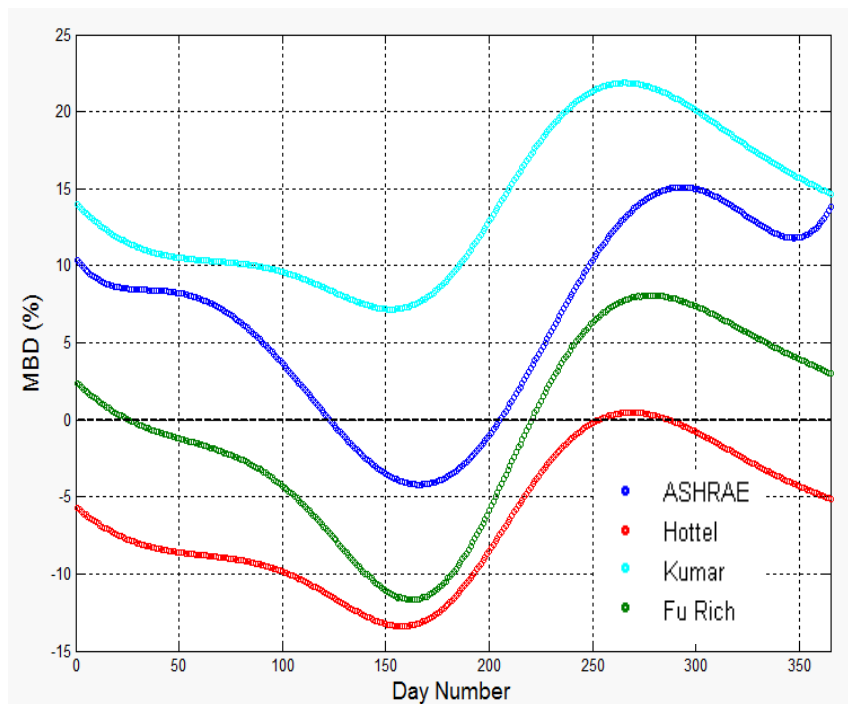
Figure 2-9: MBD as a percentage of mean measured clear-sky DNI per day for Durban.
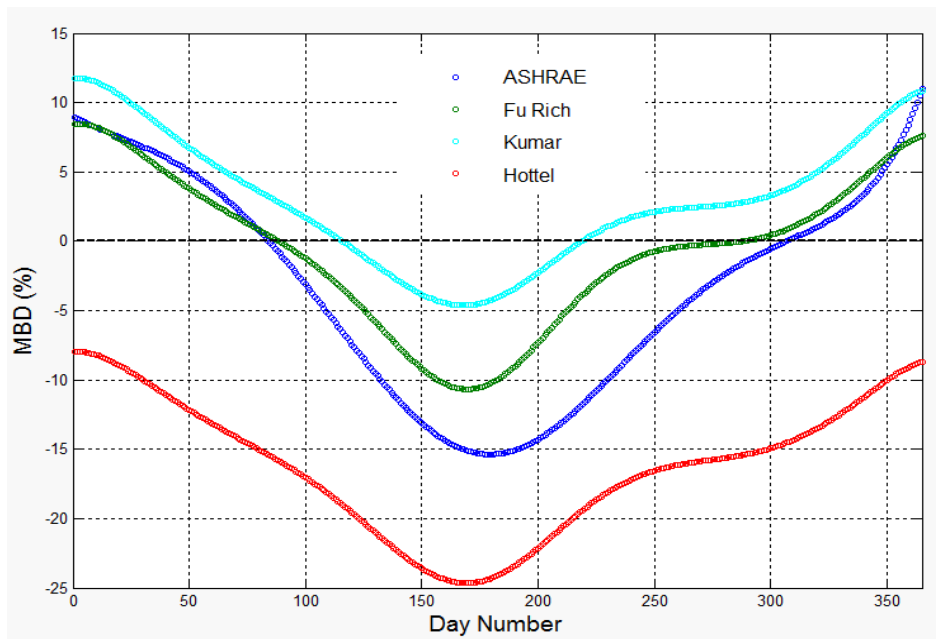
Figure 2-10: MBD as a percentage of mean measured clear-sky DNI per day for Stellenbosch.
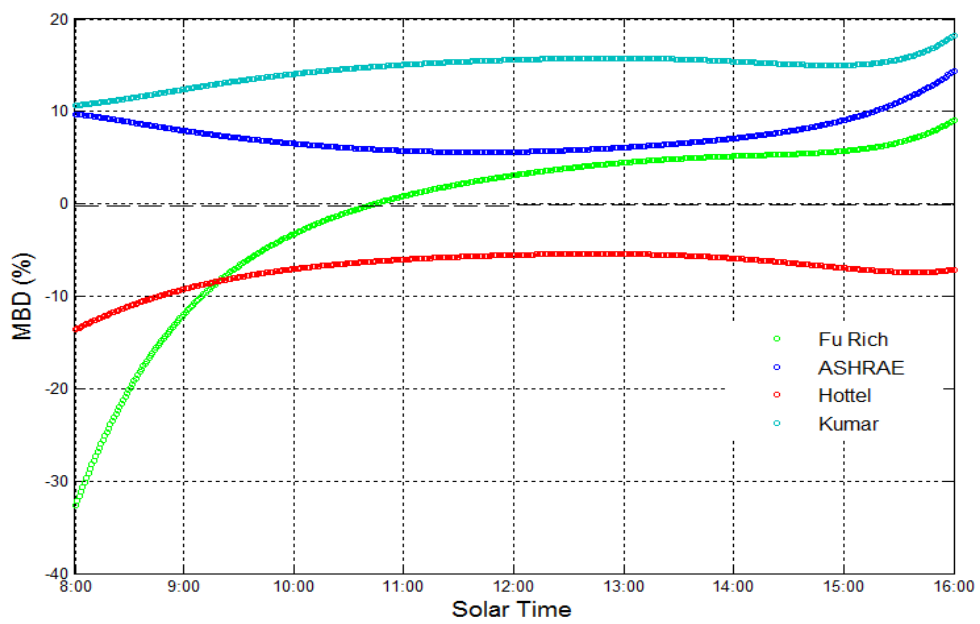
Figure 2-11: MBD as a percentage of mean measured clear-sky DNI per day for Durban.
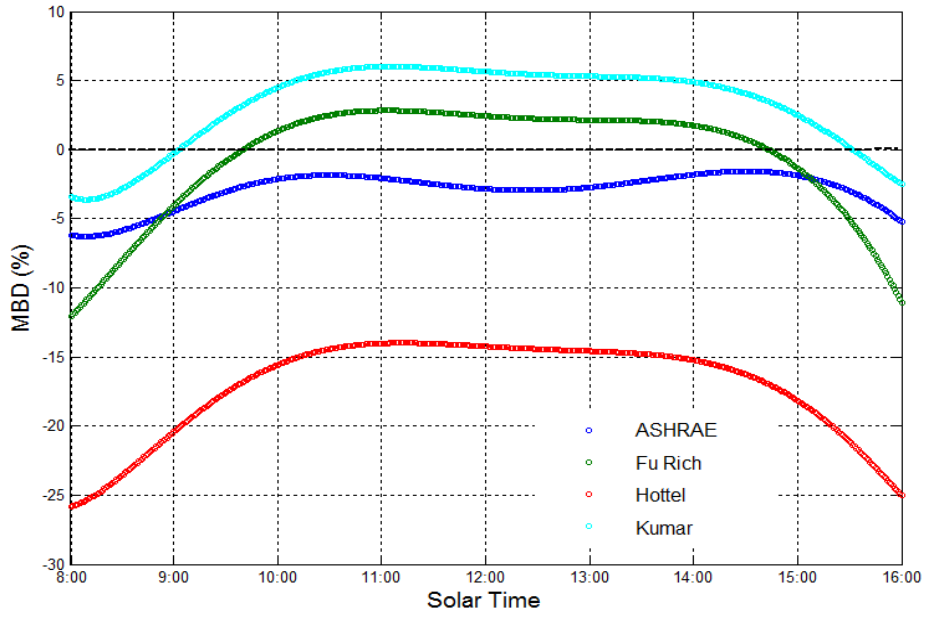
Figure 2-12: MBD as a percentage of mean measured clear-sky DNI per minute for Stellenbosch.
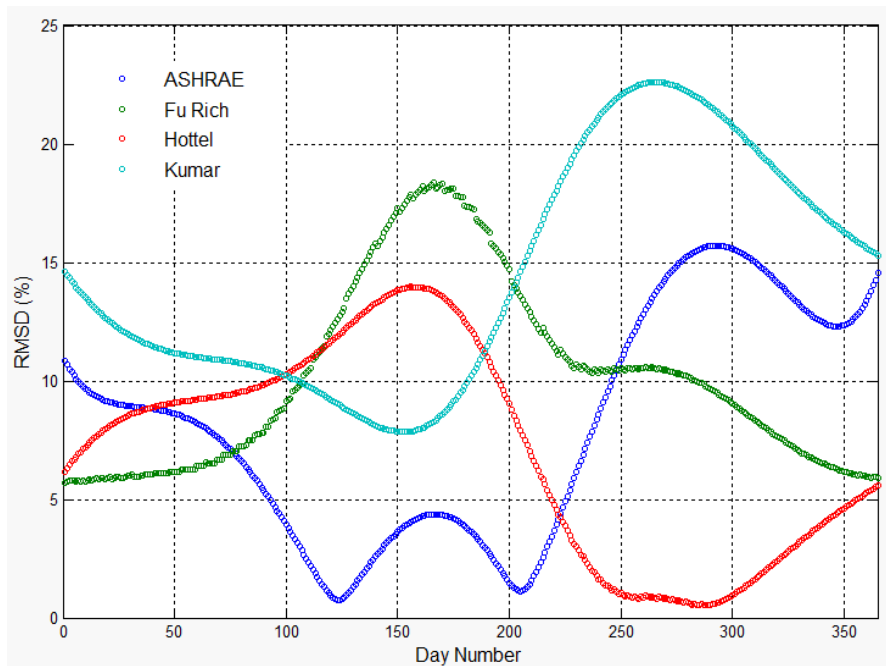
Figure 2-13: RMSD as a percentage of mean measured clear-sky DNI per day for Durban.
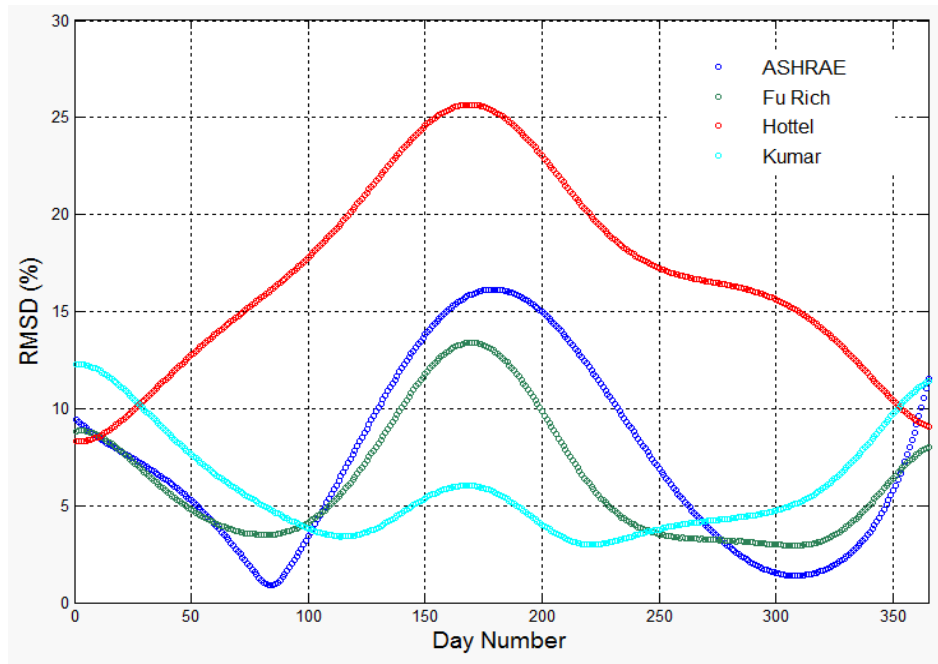
Figure 2-14: RMSD as a percentage of mean measured clear-sky DNI per day for Stellenbosch.
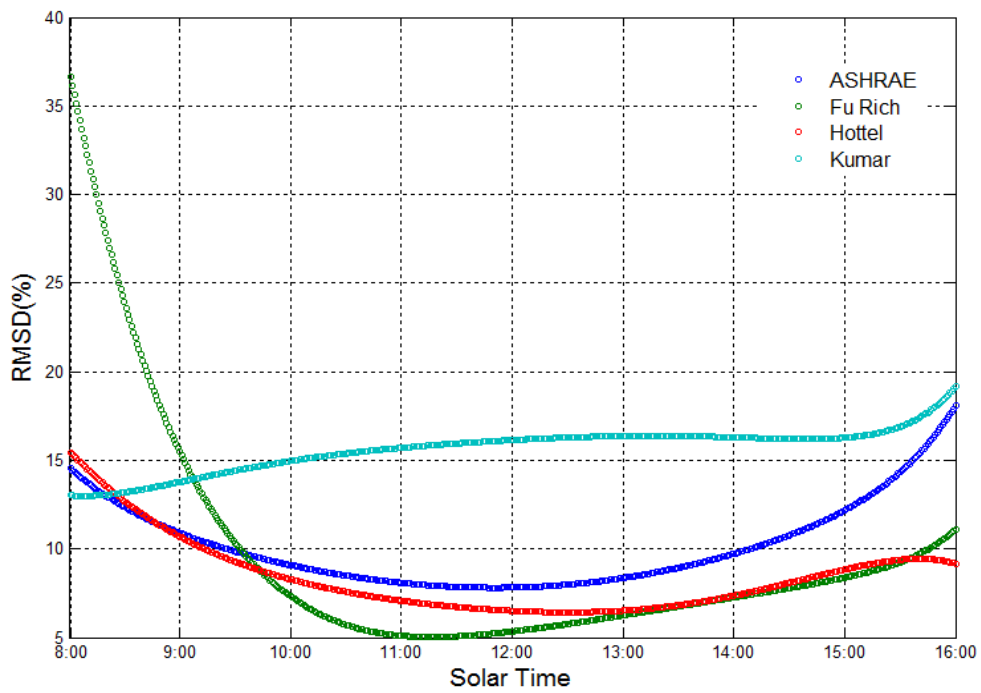
Figure 2-15: RMSD as a percentage of mean measured clear-sky DNI per minute for Durban.
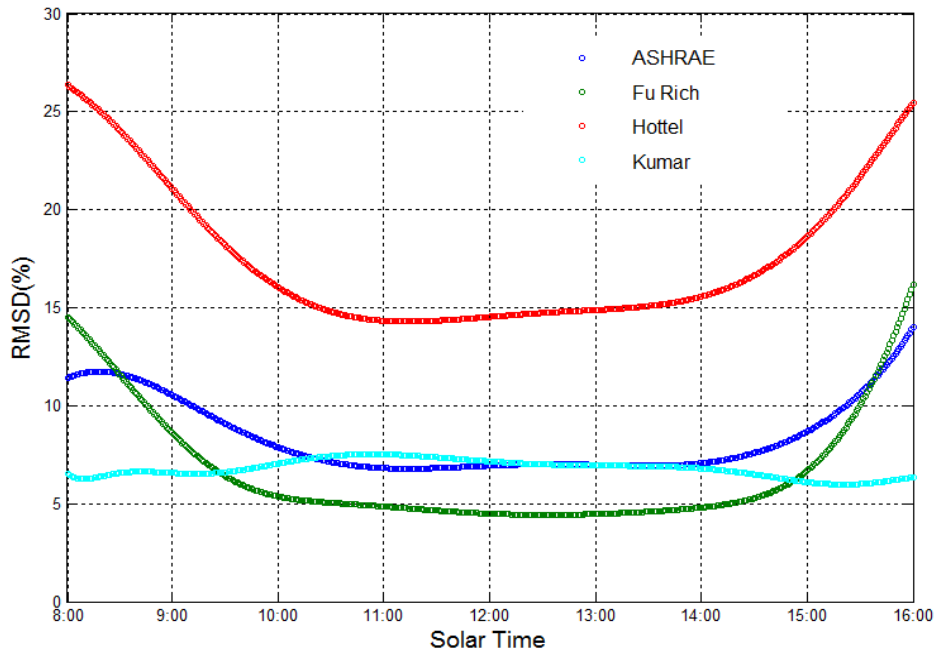
Figure 2-16: RMSD as a percentage of mean measured clear-sky DNI per minute for Stellenbosch

A solar furnace is typically operated within an appropriate period of time to successfully conduct an experiment or testing procedure. Therefore, in applying a model to predict clear-sky DNI in the absence of ground-based measurements it is critical to gauge the performance of the models on an annual and daily basis.

All models underestimate clear-sky DNI throughout winter and tend to overestimate it in summer. Certainly, this is suggestive of the inability of these simple radiative models to accurately predict seasonal variations in clear-sky DNI. However, the ASHRAE and Kumar models, as well as the tuned Fu Rich models, correlate well with the per minute TDT predictions for both Durban and Stellenbosch. These models exhibit fairly constant bias and RMSD for approximately 75% of the day. All four models become inaccurate during early morning periods and towards late afternoon. This could be because they do not include atmospheric data; therefore, modifications cannot be made to account for factors such as high levels of particulate matter in the air. The ASHRAE and tuned Fu Rich models tend to be the most stable and accurate per minute approximations of clear-sky DNI, in the absence of ground-based measurements.

2.3 Conclusion

The development and implementation of a novel algorithm for the formulation of a measurement-based model that can predict the daily and seasonal variation of clear-sky DNI at a specific location has been detailed.

The three-dimensional surface generated by the model – termed a temporal DNI topograph– reveals seasonal variations in clear-sky DNI as well as daily variability. Although it excludes the effect of opaque cloud, the model includes the effect of other attenuation sources such as site-specific, seasonal pollution phenomena. It can thus indicate the temporal and seasonal limits that bound operating windows associated with solar concentrator systems such as solar furnaces, where the clear-sky DNI must generally exceed a particular threshold value. This is achieved more accurately using the TDT algorithm than using clear-sky radiative models in which clear-sky DNI is modelled primarily as a function of air mass.

Since the empirically-derived TDT algorithm offers an alternative prediction capability to clear-sky models, four such models were used to generate comparative maps for Durban and Stellenbosch. A statistical analysis showed that the ASHRAE and the tuned Fu Rich models performed best when approximating clear-sky DNI on a daily per-minute basis, estimating values within ±5% for Stellenbosch and ±10% for Durban. However, the same models did not perform as well in predicting seasonal variations of clear-sky DNI, underestimating values by as much as 25% in winter. With the aid of the algorithm, the above radiative models can be used for preliminary solar concentrating equipment design studies at sites where there is an absence of ground-based measurements.

An exhaustive comparison of the algorithm with ground-based measurements of clear-sky DNI is necessary to further quantify the uncertainties associated with the TDT modelling approach. This will become possible as the clear sky datasets for Durban and Stellenbosch are expanded over time and inter-annual variability in the underlying measurements is better understood. In addition, it may be possible to increase the input data to the TDT algorithm by incorporating clear-sky trace segments from otherwise partly cloudy days. This would augment the underlying data, but the filtering process for selecting such measurements may require a more robust approach than the visual method used here. These issues may be addressed in future studies.

Values of DNI extracted from the TDT, for Durban, were used as inputs into an optical simulation in which SERAFF's thermal performance was approximated. These results are described in Chapter 3

Chapter 3. Heliostat Design Methodology

3.1 Introduction

There are many different heliostat designs employed in concentrating solar power plants and solar research facilities. The methodology used in sizing the heliostat, formulating design concepts and developing final designs for fabrications are detailed here.

3.2 Solar tracking

There are two primary techniques with which one can track the sun through its path across the sky. The first method uses opto-mechanical techniques and the second uses astronomical equations to approximate the sun's position. The opto-mechanical technique relies on an array of photosensitive electronic components, such as photosensitive resistors, which are used to 'sense' the direction of incoming direct solar irradiance. The extent of this technique's tracking accuracy is largely reliant on the accuracy of the photosensitive resistors as well as a high degree of accuracy in the mechanical mounting of the sensors. This study utilises a solar position algorithm based on Earth-Sun geometries that is described in the work of Stine and Harrigan (1985).

3.2.1 Earth-Sun angles

To calculate the position of the sun relative to an observer at point P, as shown in Figure 3-1, on the surface of the earth, the following Earth-sun Sun angles are to be computed.
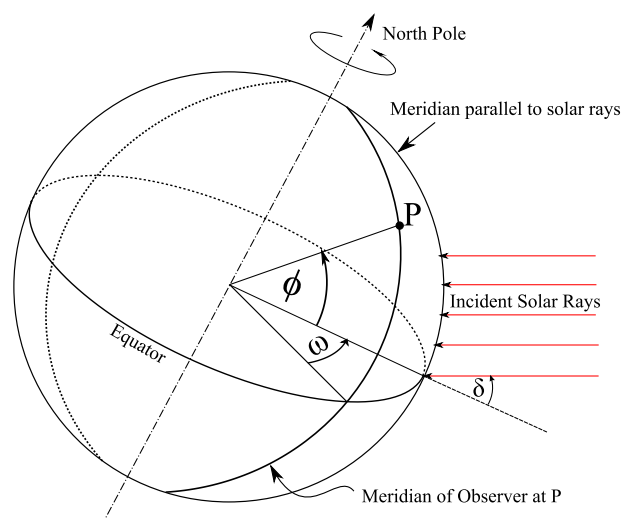
Figure 3-1:Earth-Sun angles adapted from (adapted from Stine and Harrigan, 1985).

Hour angle (ω)

The hour angle is used to describe the earth's angle of rotation about the polar axis. To quantify this angle, it is measured from the meridian of the observer at P to the meridian of a plane that contains parallel solar rays. It can then be deduced that the hour angle will be zero when the sun is at its highest point in the sky as seen from the observer. This time is termed the solar noon. It is also observed that the hour angle increases by 15° every hour. The hour angle is given by equation (15):

$$\omega = 15(t_s - 12) \tag{15}$$

The term t_s is the solar time in hours. Solar time is different from local clock time (LCT) but are related by equation (16) in hours:

$$t_s = LCT + \frac{EOT}{60} - LC \tag{16}$$

The term LC is the longitude correction factor and the term EOT is the Equation of Time, in minutes. The EOT is the difference between solar time and mean solar time and varies 17 minutes either side of solar noon throughout an annual cycle (Stine and Harrigan, 1985). For this study, as well as per recommendations made by Stine and Harrigan (1985) ,the approximation of solar time proposed by Woolf (1968) was used, which is accurate to within 30 seconds during daylight hours. The EOT is approximated in minutes using equation (17):

$$EOT = 0.258 \cdot \cos(x) - 7.416 \cdot \sin(x) - 3.648 \cdot \cos(x) - 9.228 \cdot sin2(x) \tag{17}$$

where x is, an angle defined as a function of the day number (N) shown in equation (18):

$$x = \frac{360(N - 1)}{365.242} \tag{18}$$

Declination angle (δ)

The angle between a plane through the earth's equator, called the equatorial plane, and a line drawn from the centre of the earth to the centre of the sun is called the declination angle, as illustrated in Figure 3-2.
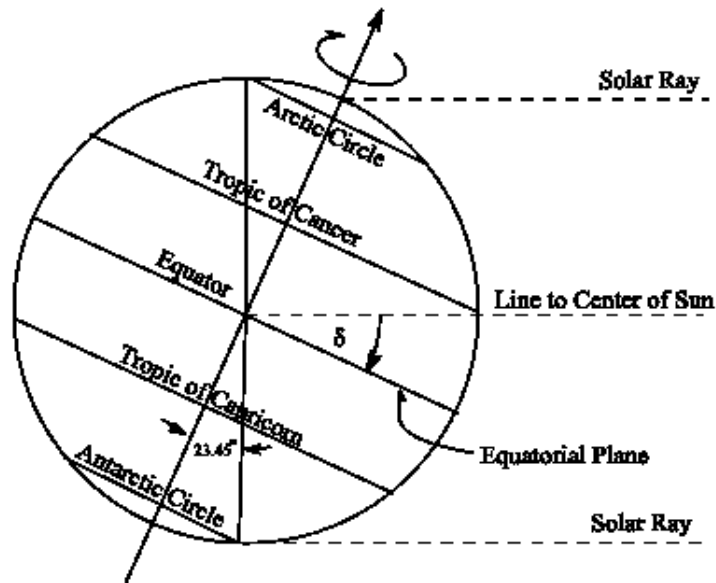
Figure 3-2: Illustration of the declination angle (Stine and Harrigan, 1985).

As in the case of the equation of time, one can use an approximation for the declination angle. An adequate approximation for most solar design tasks is given in equation (19) (Stine and Harrigan, 1985).

$$\delta = \sin^{-1}(0.39795 \cdot cos[0.98563(N - 173)])\tag{19}$$

Latitude angle (φ)

The latitude angle is the angle between a line from the centre of the earth to an observer on the surface of the earth, at *P*, and the equatorial plane, shown in Figure 3-1. Every location on the surface of the earth has a unique latitude angle. The North and South pole have latitude angles of 90° and -90°, respectively. Durban's latitude angle is -29.8579°.

3.2.2 Observer-Sun angles

Following the description of the Earth-Sun angles it is possible to fully describe the calculation of the two primary observer-Sun angles: the solar azimuth and elevation angles. Figure 3-3 shows the coordinate system used to describe the solar azimuth and elevation angle.
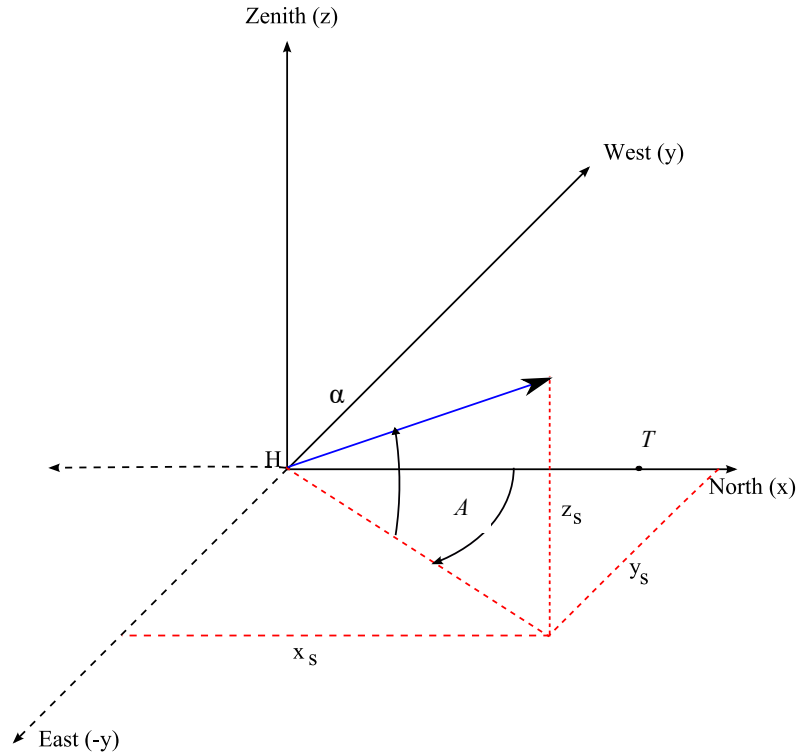
Figure 3-3: Coordinate system used in describing solar azimuth and elevation angles for the southern hemisphere.

Solar Elevation angle (α)

The solar elevation (or altitude) angle is the angle measured between the horizontal plane containing the observer, at *H*, and the central solar ray. The solar elevation angle is always positive and is a function of the declination angle (δ) (a function of date), the latitude angle (ϕ) (a function of location) and the hour angle (ω) (a function of solar time), and is described in equation (20) (Stine and Harrigan, 1985):

$$\alpha = \sin^{-1}(\sin(\delta) \cdot \sin(\phi) + \cos(\delta) \cdot \cos(\omega) \cdot cos(\phi)) \tag{20}$$

Solar Azimuth angle (A)

The solar azimuth angle is the angle measured, on the horizontal plane, from due north to the central solar ray. Equation (21) describes the azimuth angle of the sun for any position on the surface of the earth as a function of the declination angle (δ) (date), the latitude angle (ϕ) (location), hour angle (ω) (time) and the solar elevation angle (α). A test must be executed to ascertain if the solar azimuth angle is in the correct trigonometric quadrant.

$$A' = \cos^{-1}(\frac{\sin(\delta) \cdot \sin(\phi) - \cos(\delta) \cdot \cos(\omega) \cdot cos(\phi)}{\cos(\alpha)}) \qquad (21)$$

where if: $\sin(\omega) > 0$ then $A = 360° - A'$

otherwise: $\sin(\omega) < 0$ then $A = A'$

3.3 Sizing the heliostat

The size of the heliostat is primarily dependent on the size of the solar furnace's primary concentrator, as the primary concentrator should ideally be fully illuminated by light reflected from the heliostat during operation. In the case of SERAFF, the sizing of the primary concentrator is essentially governed by the thermal power output specification. For paraboloidal concentrators, the concentration ratio is proportional to the rim angle. It is possible to relate the concentrator diameter to power output in order to size the primary concentrator correctly (Punatar, 1967). The power output (P) for a given focal length (f) and rim angle (ϕ) is given by equation (22).

$$P = \pi.I_0.f.(\sin\emptyset)^2 \qquad (22)$$

The rim diameter (D) is related to the focal length of the concentrator by the geometrical relationship given in equation (23).

$$f = (\frac{D}{4(\frac{1 - cos\emptyset}{1 + cos\emptyset})^{0.5}}) \qquad (23)$$

Substituting Eq. (23) into Eq. (22) one gets an approximation of the power output as a function of the concentrator diameter and rim angle, equation (24).

$$P = \pi.I_0. \quad f = (\frac{D}{4(\frac{1-cos\emptyset}{1+cos\emptyset})^{0.5}}) . (\sin\emptyset)^2 \qquad (24)$$

The above model is a geometrically-based approximation of maximum theoretical power output of a parabolic concentrator, thus to evaluate its appropriateness it is useful to compare the rated power output of existing solar furnace concentrators to that approximated by the model, according the specific rim angles associated with each concentrator. Table 3-1 shows a list of furnaces used in the analysis. Figure 3-4 shows a plot of thermal power output versus concentrator diameter for different rim angles for several existing solar furnaces.

Table 3-1: List of solar furnaces used in power output comparison in Figure 3-4.

Name of Solar Furnace	Location	Reference
NREL Solar Furnace	United States of America	Bingham et al., 1995
PSI Solar Furnace	Switzerland	Haueter et al., 1999
PSA Solar Facility	Spain	Fernandez-Reche et al., 2006
DLR Solar Furnace	Germany	Neumann and Groer, 1996
Mont Louis Furnace	France	Open Nature, 2005
SSI-8	Ukraine	Trefilov et al., 1999
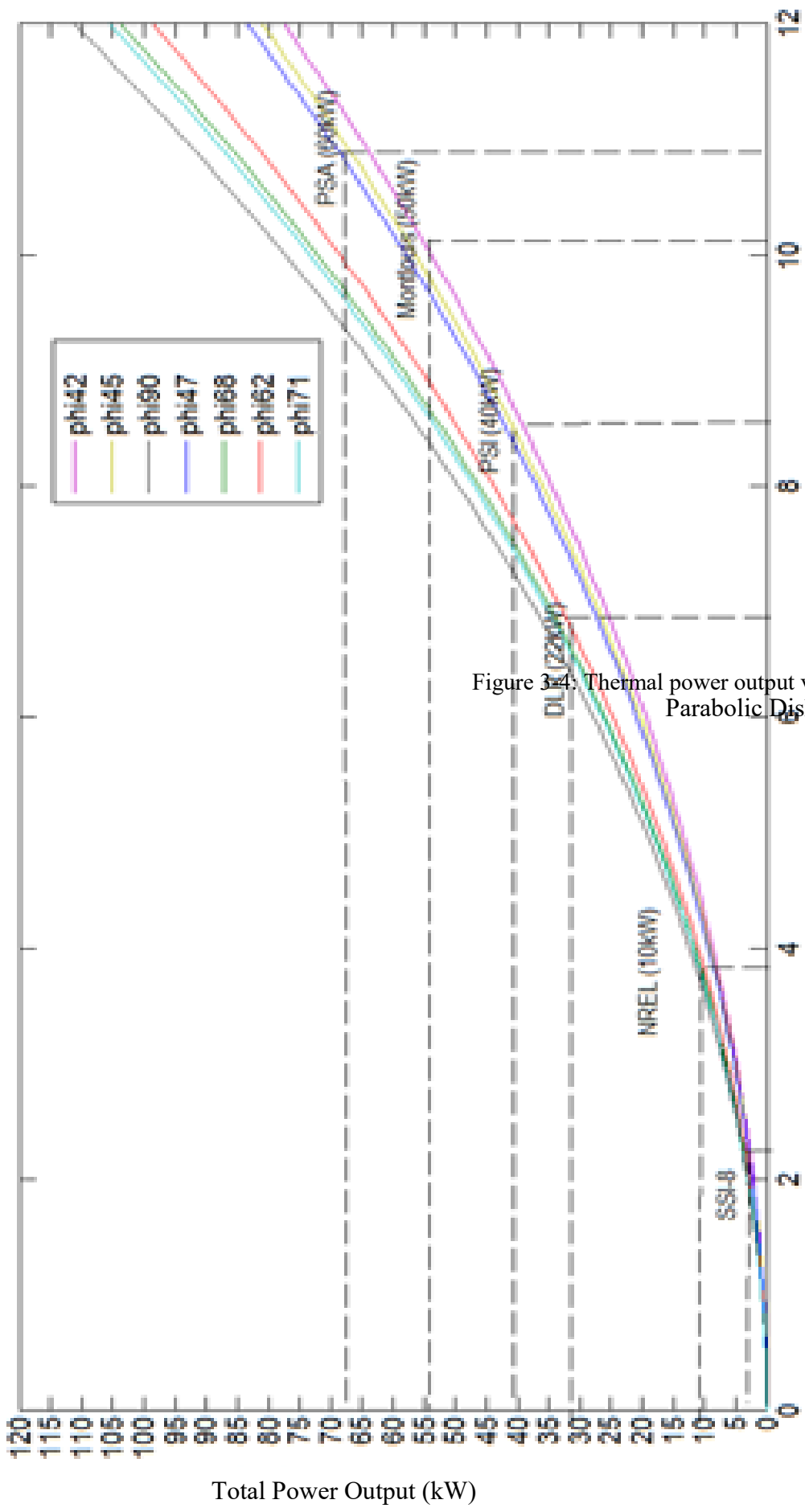
Figure 3-4: Thermal power output vs concentrator diameter for

It is interesting to note that all approximated values for thermal power output lie within 12% of measured values, which suggests that the model provides a reasonable representation of real paraboloidal concentrators. For a specified maximum thermal power output of 5 kW, it is calculated that a paraboloidal concentrator approximately 3 m in diameter is required, assuming an ideal rim angle of 45°.

Ideally, the heliostat should fully illuminate the primary concentrator aperture throughout the day or particular window of operation. After reviewing the expected costs and practical limitations in fabricating a large heliostat it was decided, in accordance to the above theoretical model, that a 3 m x 3 m flat heliostat would be sufficient for the facility.

To evaluate the energetic performance of the optical system, further optical studies were required. These included a study on the effect that optical errors can have on the performance of the heliostat, as well as the determination of the degree to which the heliostat can illuminate the primary concentrator throughout the year. These optical studies are described in Section 3.4.

3.4 Optical analysis

Ray tracing procedure

The ray tracing method is commonly used in optical design and analysis. It involves the tracing of a single narrow beam or ray through the various stages of an optical system. With the availability of substantial computing power, it is possible to trace and observe the optical interactions that a multitude of rays would encounter throughout their path through an optical system. Some of these optical interactions are probabilistic in nature, for example the sun-shape or angular distribution, and some are deterministic, where resultant deflections from ray intersections with analytically-described surfaces are determined. For a complete ray trace analysis, there are a few components that needed to be characterised within the ray tracing environment. For this work, the commercial ray tracing software TracePro™ was used due to its established reputation, versatility and ease of use. Figure 3-5 shows the general procedure that was applied in setting up and running a ray trace operation within the TracePro environment.
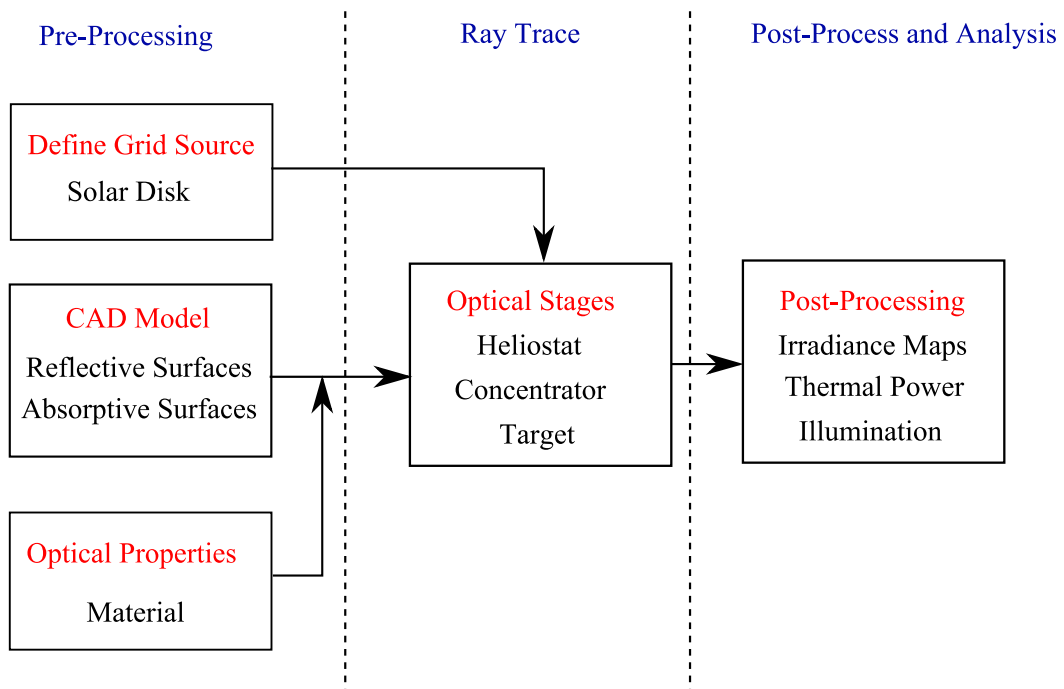
Figure 3-5: General Ray tracing procedure.

The pre-processing stage involved creating a three-dimensional model of the optical components which make up the overall optical system. These needed to be to-scale and in the correct spatial configuration, and were imported from Siemens NX™ parametric modelling software as primitive shapes. Primitive shapes were used to reduce computational expense. Optical properties were configured by selecting a material type for each of the reflecting surfaces as well as the target absorptive area, which allowed TracePro™ to automatically configure the required optical properties, such as reflectivity and slope distribution, per the material selected. In the case of this study, polished aluminium was selected for the reflecting surfaces and the target area was assumed to be a perfect absorber.

Another important aspect of the pre-processing stage was configuring a suitable light source from which the rays were to emanate. TracePro™ utilises a grid source that assumes a probabilistic Gaussian distribution of sun intensity of the solar disk with a 5 mrad half angle, as illustrated in Figure 3-6.
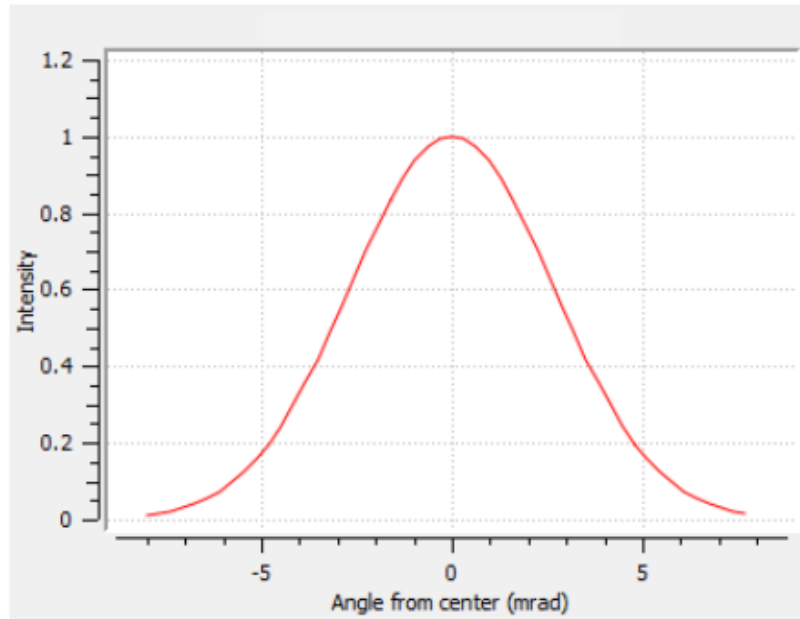
Figure 3-6: Gaussian distribution of sun intensity.

The last primary property to configure before executing the ray traces was to initiate the number of rays to trace. The accuracy of a ray trace simulation is directly proportional to the number of rays running through the optical system, but this increase in accuracy is at the expense of computational solution time. Thus, it is important to find the point at which the accuracy of the solution ceases to increase with a further increase in the total number of rays propagating through the optical system. Finding this number required an iterative process in which a simulation output variable, for example, the average flux at the target of the solar furnace, was monitored as the number of traced rays was increased. When this monitored value was found to plateau then it was assumed that no further increase in the number of rays would lead to an increase in accuracy. As a result of this process a value of ten million rays was chosen for all ray trace simulations.

The post-processing capabilities of TracePro™ are broad, but there are a few key features that were relevant to and useful in the design of the solar furnace heliostat. The most useful of these were found to be the irradiance/illuminance maps which show irradiance incident to, absorbed by, or exiting from a selected surface, such as the parabolic concentrator aperture or target area. The post processing results were used to validate the appropriateness of a heliostat 3 m x 3 m in size from a purely optical perspective.

Optical errors

There are certain optical errors encountered when working with real-world reflectors. The two primary optical errors are slope error (σ_{slope}) and specularity error ($\sigma_{specular}$). These are illustrated in Figure 3-7.
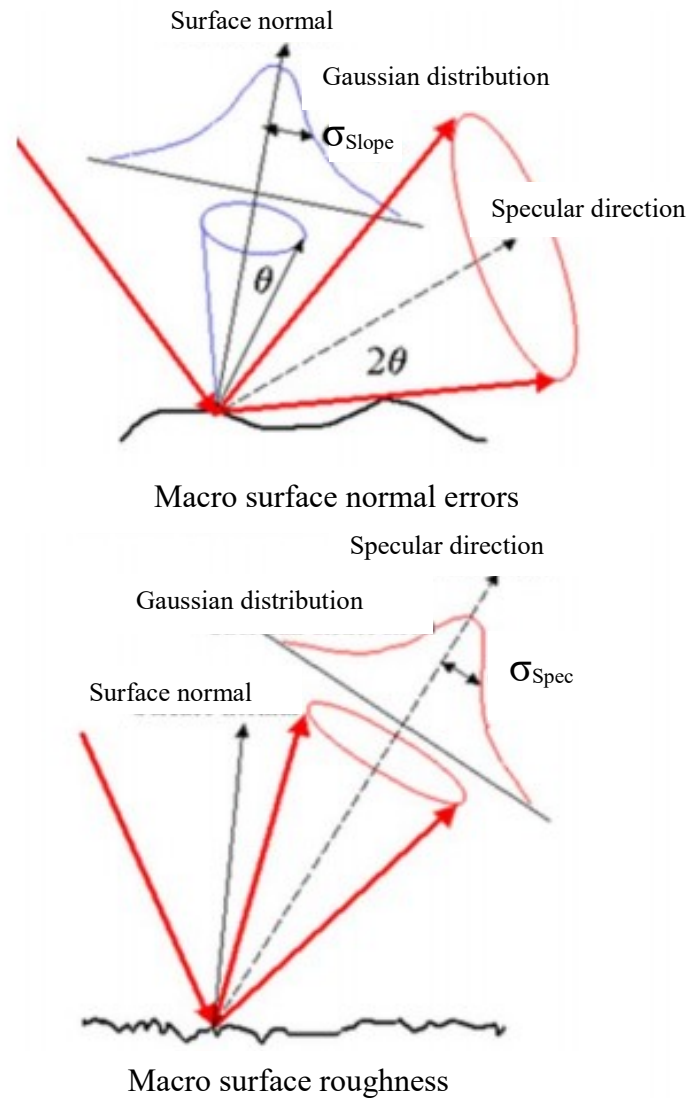
Figure 3-7:Effects of Gaussian distributed slope and specularity error on reflected ray (Wendelin et al., 2013).

Both errors lead to a deviation of the reflected ray from its specular direction by some degree, typically measured in milliradians. Both errors are probabilistic and typically described by a Gaussian distribution. A Gaussian distribution of the specularity error for polished aluminium (and other common optical materials) was modelled by TracePro™. Slope error is a difficult property to physically measure on real-world reflectors. Since physically measuring slope error is difficult it is useful to look to the literature. According to the literature, a slope error range of

approximately 1.2 to 1.5 milliradians is typical for real-world heliostats which utilise polished aluminium reflectors (SolarPACES, 2000a). Using this range in conjunction with TracePro™ it is possible to understand how slope error can affect the performance of solar furnace's which comprise of heliostats of varying size.

An optical system was setup within TracePro™ that matches SERAFF's intended configuration which includes a parabolic concentrator with a diameter of 3 m, flat non-focusing heliostat and an absorber (10 cm x 10 cm square black body). An increase in slope error will cause a reduction in the amount of solar irradiance the absorber intercepts and thus absorbs. The amount of intercepted irradiance can be either calculated directly or, the effect of the reduction in intercepted irradiance can be observed through monitoring the average flux on the absorber. Thus, the average thermal flux on the absorber was monitored to observe the effects of varying slope error and heliostat size for the winter solstice day (June 22nd) using DNI data extracted from the TDT derived in Chapter 2. The results of the ray traces are shown in Figures 3 to 11.
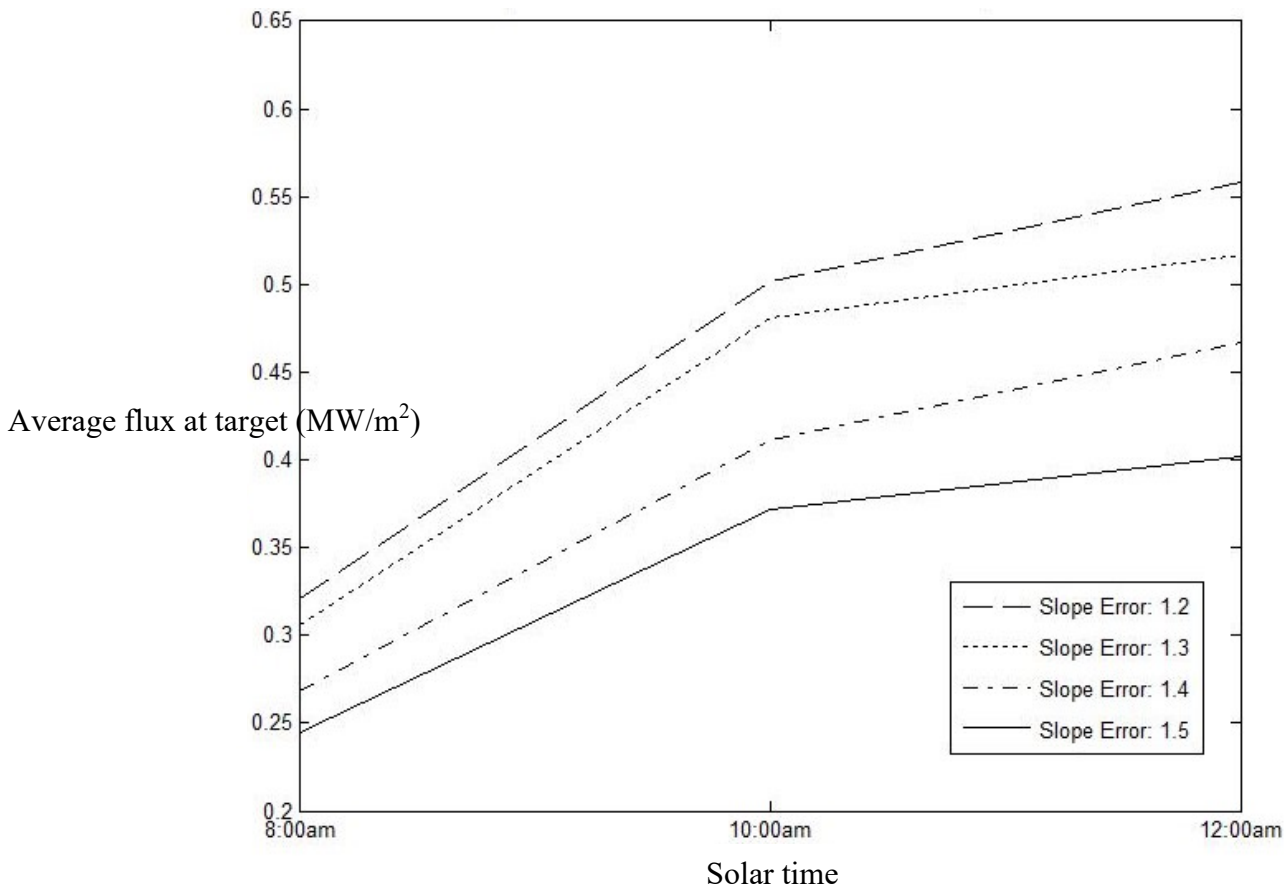
Figure 3-8:Average flux as a function of slope error for a 2.5 m x 2.5 m heliostat.

Average flux at target (MW/m^2)

Solar time
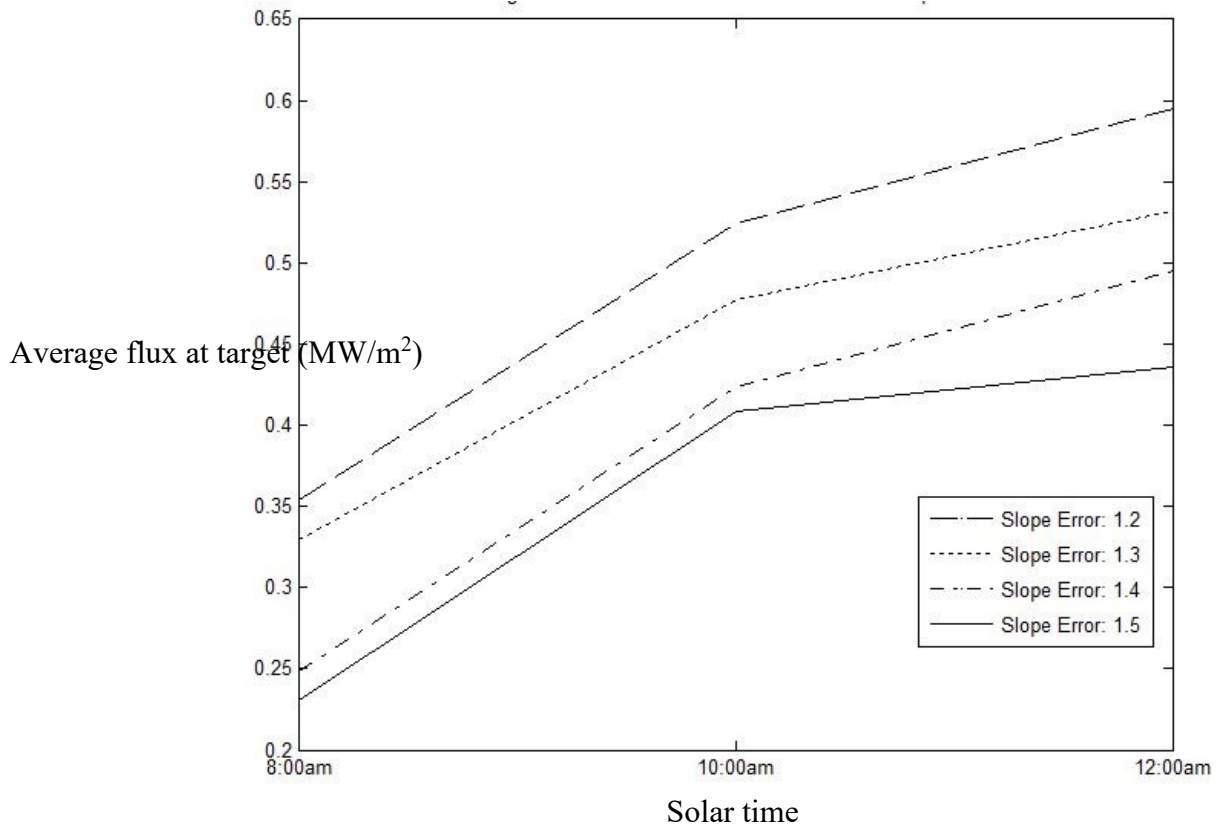
Figure 3-9:Average flux as a function of slope error for a 3 m x 3 m heliostat.

Average flux at target (MW/m^2)

Solar time
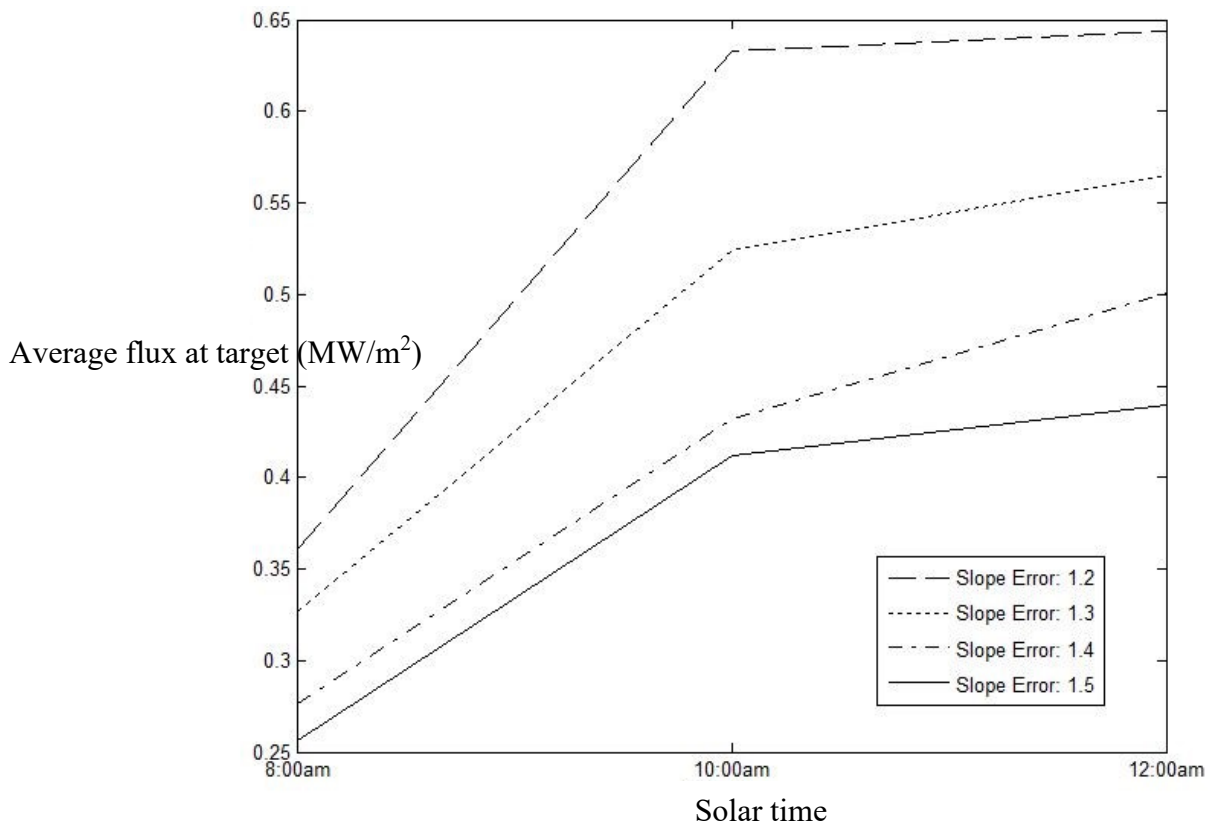
Figure 3-10: Average flux as a function of slope error for a 3.5 m x 3.5 m heliostat.
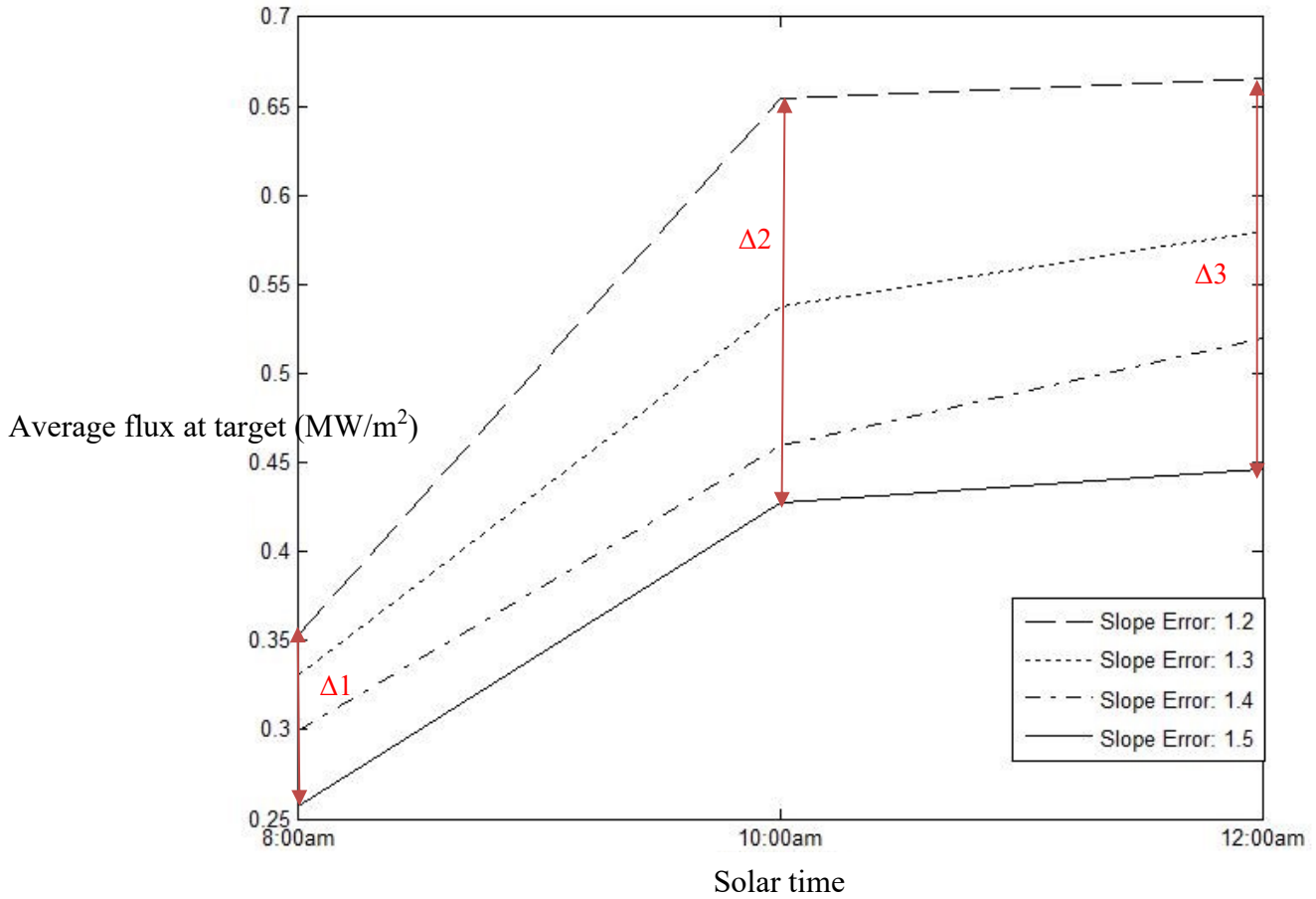
Figure 3-11:Average flux as a function of slope error for a 4 m x 4 m heliostat.

A useful observation that can be made from these results is that the size of the heliostat affects the sensitivity of a solar furnace's performance to optical slope error. An indication of this sensitivity can be determined by calculating the average decrease ($\Delta 1$, $\Delta 2$ and $\Delta 3$) in average thermal flux from 8:00am to 12:00am for four different sizes of heliostat. The sensitivity (ϑ) is given by equation (25) and the results are listed in Table 3-2.

$$\vartheta = \frac{\Delta 1 + \Delta 2 + \Delta 3}{3} \tag{25}$$

Table 3-2: Slope error sensitivity for different heliostat sizes

Heliostat Size	Sensitivity (ϑ) (MW/m^2)
2.5 m x 2.5 m	0.1206
3 m x 3 m	0.1323
3.5 m x 3.5 m	0.1762
4 m x 4 m	0.1804

If average flux is considered as the metric in analysing the results of the ray trace then it can be understood that the larger the heliostat is within a solar furnace, the more sensitive it is to the effects of heliostat slope error. Slope error is a function of macro-surface irregularities, thus it is intuitive to conclude that a larger reflective surface area will amplify the effects of slope error on the reflected light rays and thus decrease the flux performance of the solar furnace, as observed in the results. If the heliostat size is decreased, then the sensitivity of solar furnace flux performance to heliostat slope error decreases.

A 4 m x 4 m heliostat would certainly intercept a larger fraction of total incoming direct solar irradiance than, say, a 2.5 m x 2.5 m heliostat, hence achieving a good amount of thermal flux on the absorber. However, a 4 m x 4 m was not chosen due to considerations made based on financial and practical constraints.

A 2.5 m x 2.5 m heliostat would never illuminate a 3 m diameter concentrator aperture even under the most ideal conditions therefore it was not a viable heliostat size for this application.

To strike a balance between heliostat optical accuracy and solar furnace performance, a 3 m x 3 m heliostat presented itself as the most suitable option, with all financial and practical constraints considered. However, an *illumination study* was needed to prove the 3 m x 3 m heliostat would achieve a satisfactory level of concentrator aperture illumination through all angles of solar incidence throughout the year. This was proved and illustrated in the *illumination study* using a ray tracing simulation.

Illumination study

The fundamental task of a solar furnace heliostat is to illuminate the aperture of the primary concentrator and continue to do so whilst the sun changes its position in the sky. Multiple ray traces were needed to confirm that the 3m x 3m heliostat could achieve a satisfactory level of concentrator aperture illumination. Executing a ray trace for everyday of the year would be time consuming and tedious. However, much of SERAFF's operation would take place during winter due to Durban's climate, therefore making the winter solstice day an appropriate 'reference' day in which to design for. Using winter solstice as the 'reference' day may yield a slightly larger concentrator than what is absolutely necessary, however, it was decided that it would be easier to upsize the heliostat with an already larger concentrator rather than having to, both, upsize the heliostat and concentrator at once. Using the same optical setup in TracePro™ as the one used for slope error analyses, it is possible to visualise the light rays that enter the aperture of the primary

concentrator. Figure 3-12 shows the irradiance distribution over the primary concentrator as received from a 3 m x 3 m heliostat from 7:00am to 12:00am.
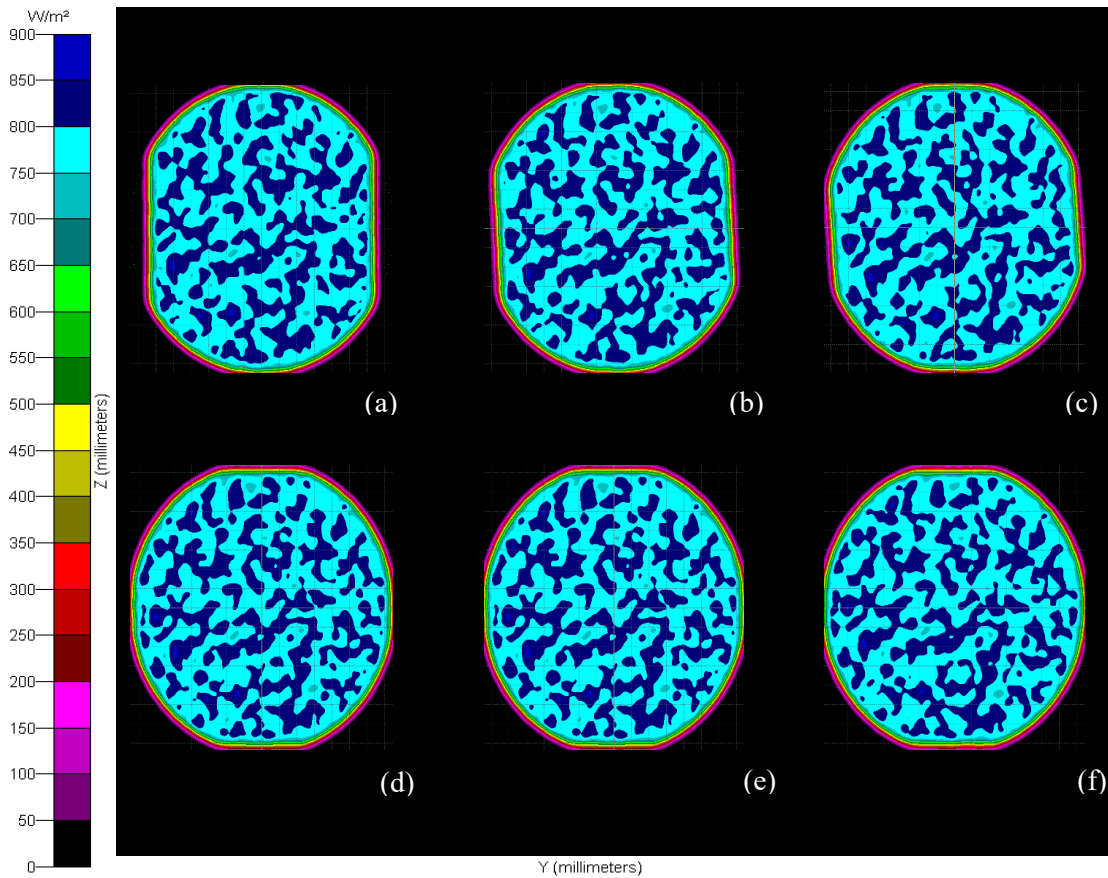
Figure 3-12: Total flux entering the primary concentrator aperture. (a) 7:00am (b) 8:00am (c) 9:00am(d) 10:00am (e) 11:00am (f) 12:00am.

At 7:00am there is a "squashed" image cast onto the concentrator aperture, this is largely due to the very low solar azimuth angles. This shape can be neglected as the solar furnace will not be operated at this early hour. The heliostat dimension of 3 m x 3 m was selected based on practicality, although in the worst-case scenario, the incident rays illuminate concentrator aperture almost entirely.

3.5 Conceptual designs and final design selection

3.5.1 Conventional heliostat designs

A common structural configuration for large heliostats in the CSP industry is the "T" design. This comprises a vertical steel or concrete pillar firmly attached to the ground through a subterranean

foundation, and a horizontal steel torque tube running the width of the heliostat reflecting surface, which forms the iconic "T" shape. The pillar allows for azimuthal rotation of the heliostat reflecting surface and change in elevation angle occurs about the torque tube. Figure 3-13 shows a conventional heliostat design used in both a solar furnace facility and in central receiver plants.
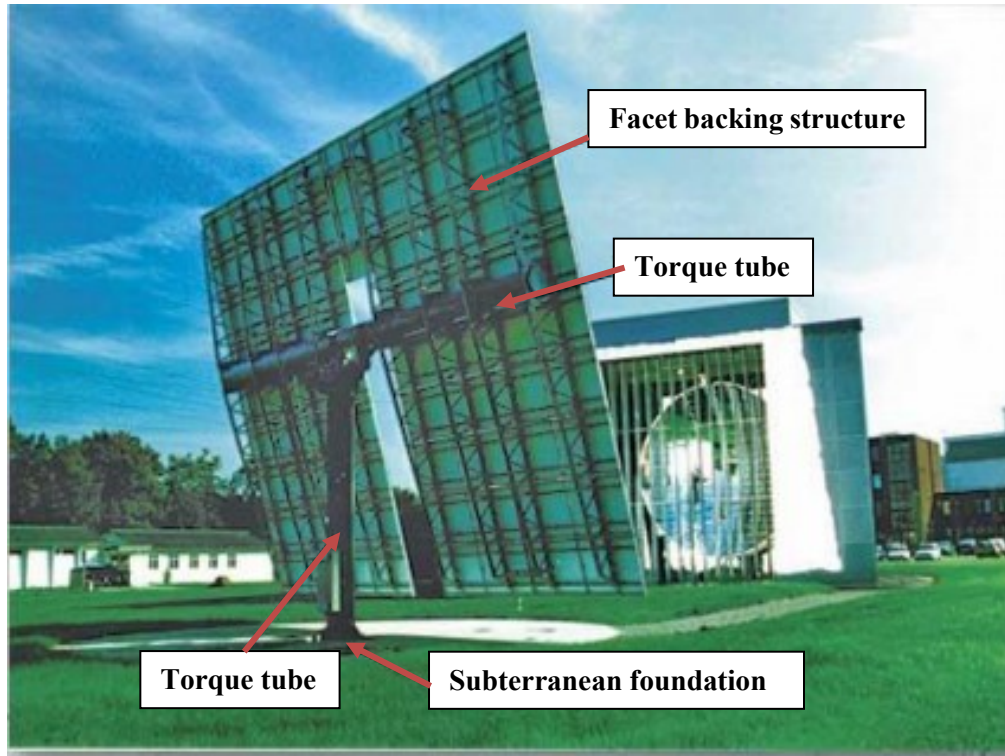
Figure 3-13: PSI Solar furnace facility (Haueter et al., 1999).

An advantage of the "T" design is that the pillar diameter is scalable with respect to the overall dimensions of the heliostat and can be attached to the ground through firm concrete foundations. However, the use of custom drives and concrete foundations often leads to high heliostat costs. The overall weight of the heliostat is also increased with the need for a rigid steel lattice used to support the reflective surface.

A disadvantage of a conventional heliostat is that it is particularly sensitive to wind loading, which results in high levels of material stresses and a drop in optical performance unless the support structures are suitably sized and reinforced (Chuncheng et al., 2012).

The conventional heliostat design has been made popular for large scale heliostat arrays because it is considerably easier to manufacture and install than more complex, unconventional heliostat configurations. Heliostats account for approximately 40-50% of a CSP plant's initial capital (SolarPACES, 2000b), hence the prolific use of conventional heliostat design in industrial

applications. Table 3-3 shows the approximate cost fraction of major heliostat components in a conventional heliostat.

Table 3-3: Relative cost fraction for major heliostat components.

Component	% of Total Heliostat Cost
Azimuth and Elevation Drives	30-35%
Mirror Assemblies	25-30%
Structural Support	15-20%
Assembly and Install	10-15%
Pedestal and Foundation	10-15%
Control Software and Electronics	5-10%

Up to 35% of a conventional heliostat cost can be attributed to the actuation system employed. This is largely due to the nature of the configuration, which require the actuators to act as structural components as they bear high stresses due to the weight of the reflecting surface and wind loads.

3.5.2   Unconventional heliostat designs

Unconventional heliostat designs are usually motivated by the aim of reducing the high capital cost of conventional heliostats in CSP projects (Coventry and Pye, 2014). In particular, unconventional heliostat designs typically seek to reduce the quantity of structural material, overall mass and to simplify the actuation system (Brender, 2013). Most of the unconventional heliostat designs reviewed in this chapter have not been implemented in long-term commercial or research applications. An exception is, for example, the heliostat array developed for CSP research by SANDIA National Laboratories and illustrated in Figure 3-14.

Figure 3-14: SANDIA's National Solar Thermal Test Facility (NSTTF) heliostat (SANDIA, 2008).

The heliostat design implemented at SANDIA's NSTTF employs an alternate support pillar design. It uses a "U-beam" to support the reflecting surface and a slew drive actuator at the base of the pillar. This allows for minimal offset of the centroid of the reflecting surface to the axis of rotation. This increases tracking accuracy thus increasing optical performance. Another example of an unconventional design is the HELLAS 01 (SolarPACES, 2000a) heliostat which employs an aluminium and steel frame as the mirror backing structure.

Figure 3-15: HELLAS 01 heliostat (SolarPACES, 2000b).

Several other unconventional designs were reviewed, including a heliostat developed for the DLR solar furnace (Pfahl et al., 2013) and the Titan Tracker (Titan, 2014).

3.5.3   Concept selection

An effort to combine the most attractive and suitable elements of both the conventional and unconventional design approaches was made. This was accomplished by pairing core structural design elements from each of the reviewed heliostats and scoring them against certain criteria. The design criteria included material quantity, mass (without foundation) and practicality (ease of manufacture). A heliostat can be grouped into the following three core structural components:

- Foundation (ground anchoring)
- Pillar (upright support structure)
- Mirror backing structure (includes torque tube in some cases)

There are both common and unique design elements attributed to these three core structural groups. In Table 3-4, each common element is labelled F_n, P_n, B_n, where F, P and B denote the

foundation, pillar and backing structure, respectively. If a design element within each of the three core structural groups is unique then it is denoted by either F_{n+1}, P_{n+1} or B_{n+1} and so on. For example, a common foundation element shared among the reviewed heliostats may be denoted as F_1 whereas if a foundation element is unique for a particular heliostat then that element is denoted by F_2. The heliostats reviewed are referenced using the Heliostat Catalog presented at SolarPACES (2000a).

Table 3-4: Design elements assigned to each core structural group.

Heliostat	Foundation	Pillar	Backing Structure
Colon 70	F_1	P_1	B_1
PSI 120 Heliostat	F_1	P_1	B_1
Sanlucar 90	F_1	P_1	B_1
ATS H100	F_1	P_1	B_1
ATS H150	F_1	P_1	B_1
HELLAS 01	F_1	P_2	B_2
SAIC Multi Facet	F_1	P_1	B_1
AMS H150	F_2	P_1	B_1
Titan Tracker	F_2	P_1	B_3
SANDIA	F_1	P_3	B_1

F_1 – Subterranean foundation $\qquad$ F_2 – Concrete rails $\qquad$ P_1 – Steel tube
P_2 – Concrete pillar $\qquad$ P_3 – U-shaped beam $\qquad$ B_1 – Steel trusses
B_2 – Aluminium tubing $\qquad$ B_3 – Steel frame

After each design element is assigned to its respective core structural group, it is then possible to configure a heliostat design concept containing each of the three core structural components.

It must be noted that the proposed site of installation for UKZN's heliostat does not allow for permanent subterranean foundations since the site is atop a water reservoir with approximately 500 mm of topsoil. This eliminates the possibility of using design elements F_1 and F_2 in any configuration. A custom configuration for the foundation had to be developed to suit the particular site location, and for completeness the custom foundation is labelled F_c. This left the potential configurations reflected in Table 3-5.

Each individual design element was given a score out of 5 (1 being desirable and 5 being undesirable) for the categories: material quantity, manufacturability and mass, respectively. For example: P_1 received a score of: 2 for material quantity, 2 for manufacturability and 3 for weight. These individual scores formed the following triplet of scores:

$$P_1\{2,2,3\}, \ P_2\{3,5,6\}, \ P_3\{3,3,3\}, \ B_1\{5,5,4\}, \ B_2\{3,2,2\}, \ B_3\{3,3,4\}\}$$

The individual scores that form the triplet were added to the corresponding score of its partnering design element; for example, if P_1 were to be paired with B_1 then that configuration would score 7 (2+5) for material quantity.

Table 3-5: Heliostat concept configuration selection matrix.

#	Configuration	Material Quantity	Manufacturability	Weight	Total
1	$F_c + P_1 + B_1$	7	7	6	20
2	$F_c + P_1 + B_2$	7	4	5	16
3	$F_c + P_1 + B_3$	5	5	7	17
4	$F_c + P_2 + B_1$	8	10	9	27
5	$F_c + P_2 + B_2$	6	7	7	20
6	$F_c + P_2 + B_3$	6	8	9	23
7	$F_c + P_3 + B_1$	8	8	7	23
8	$F_c + P_3 + B_2$	6	5	5	16
9	$F_c + P_3 + B_3$	6	6	7	19

Using this approach, it was found that configurations #2, a steel tube pillar with an aluminium tube mirror backing structure, and #8, a U-shaped beam pillar with an aluminium tube mirror backing structure, offer the best characteristics since they were the two lowest scoring configurations. It must be noted that this selection algorithm did not consider the overall rigidity and strength of the heliostat assembly.

3.6 Final heliostat design

To finalise the design of the heliostat, from concept to a working design, virtual CAD modelling and finite element analysis was utilised. The software package used in this study for these purposes was Siemens NX™. The concepts were compared and selected using wind loading as the primary design loading factor. Thus, a full characterization of wind loading was carried out for Durban. Figure 3-16 illustrates the workflow employed from concept to final working design.
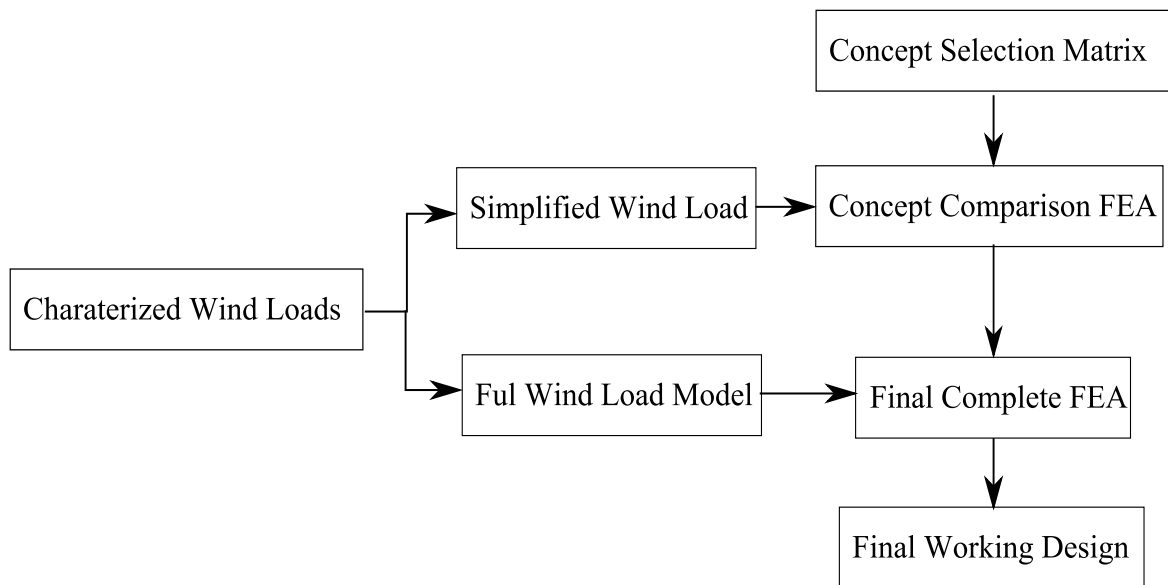
Figure 3-16: Final design workflow using wind loading schedule.

The following sections will cover the characterization of wind loads for Durban, utilising both a simplified and a more complex wind loading model. The simplified model was used in the concept comparison FEA, whilst the more complex model was used for the final complete FEA on which the final working design was based.

3.6.1 Characterizing wind loads

The South African Bureau of Standards (SABS) has published guidelines on evaluating wind loading on structures and buildings. The South African National Standard (SANS) 10160-3 (SABS, 2011) provides wind loading factors and offers a mean design wind speed for coastal locations such as Durban. Figure 3-17 shows the mean wind speed upon which structural design calculations are to be based, in accordance with the standard.
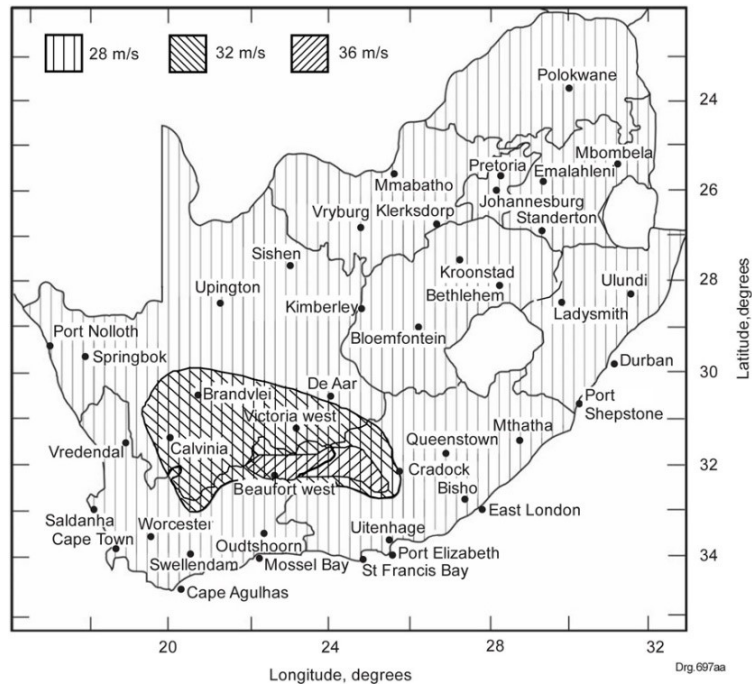
Figure 3-17: Nominal design wind speeds in South Africa (SABS, 2011).

The South African wind climate is complex, especially regarding strong frontal winds in coastal areas and intense thunderstorms in the inland areas (SABS, 2011). To overcome this complexity, the standard uses a conversion factor computed from hourly and 10-minute based wind speed measurement averages to attain a nominal design wind speed. For the case of Durban, this value is 28 m/s.

Wind acts most significantly as a pressure normal to a confronting surface. However, shear forces are also present. In the specific case of buildings and complex structures, both internal and external pressures are considered.

Simplified wind load model

The simplified wind model considers only the resultant external normal pressure on the heliostat reflecting surface. Since the heliostat reflective area has been determined, the resultant pressure on a 9 m^2 flat plate (assuming a coefficient of drag being unity) was calculated per the bluff body drag force determined by equation (26):

$$F_x = \frac{1}{2}.\rho_{air}.V_{air}{}^2.A_{surf} \tag{26}$$

ρ_{air}, V_{air} and A_{surf} are the air density, nominal design wind velocity and the total surface area of the heliostat reflective surface, respectively. At 28 m/s, or 100 km/h, this force is equivalent to

3.819 kN. Volumes calculated using virtual CAD models of the heliostat backing frame and mirror modules were used to evaluate their respective masses. In this manner, an approximated weight of 3 kN was determined and applied to the structure to represent the effect of gravity loading.

Full wind load model

Equation (26) assumes that the worst-case wind loading scenario (coefficient of drag is unity) occurs when the heliostat reflecting surface is perpendicular to the wind direction. However, in real world application the heliostat will be subjected to winds approaching at varying directions and wind-ground interactions will occur. To account for the different wind angles and other phenomena, it is important to utilise a more accurate model to characterise the wind loading on the heliostat.

Although not practical, it would have been advantageous to be able to perform a wind tunnel test on the chosen heliostat design to gather data on its performance under different wind loads. As an alternative, correlations from the comprehensive wind tunnel test study by Peterka and Derickson (1992) were used. The study generated force and moment coefficients for an isolated heliostat, such as that being designed in this study, which are summarised in Figure 3-18. A study conducted by Hariram (2015) aimed to build a comprehensive computational fluid dynamic (CFD) model to be utilised in wind load analysis on heliostats. The CFD model was built upon some of the fundamental findings and equations from the work of Peterka and Derickson (1992).
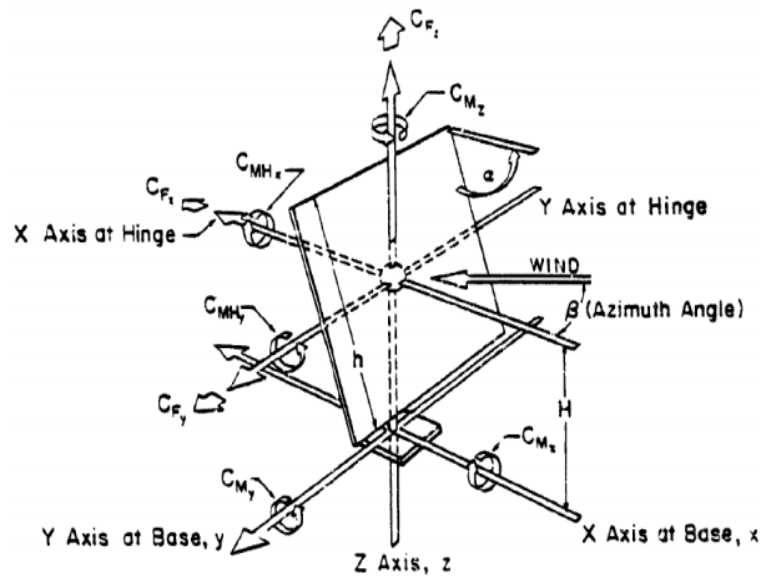
	Fx, My Max	Fz, MHy Max	Mz Max	Stow Loads
PEAK LOADS				
α, degrees	90	30	90	0
β, degrees	0	0	65	0
Fx	4.0	2.1	3.7	0.6
Fz	1.0	2.8	0.5	0.9
MHy	0.25	0.6	0.15	0.2
Mz	0.29	0.06	0.7	0.02
MEAN LOADS				
α, degrees	90	30	90	0
β, degrees	0	0	65	0
Fx	2.0	1.0	1.6	0.1
Fz	0.3	1.35	0.3	0.1
MHy	0.02	0.25	0.02	0.02
Mz	0	0	0.25	0

n = 0.15   Tu = 18%   Zo = 0.03 meters

Figure 3-18: Published drag and force coefficients and reference coordinate system used in the study (Peterka and Derickson, 1992).

The study determined coefficients for various wind directions during operation, as well as during heliostat stowage. To understand the significance of wind loading on the heliostat, it is instructive to plot the relationship between the various forces and moments as a function of the nominal design wind speed, shown in Figures 3-19 to 3-21.
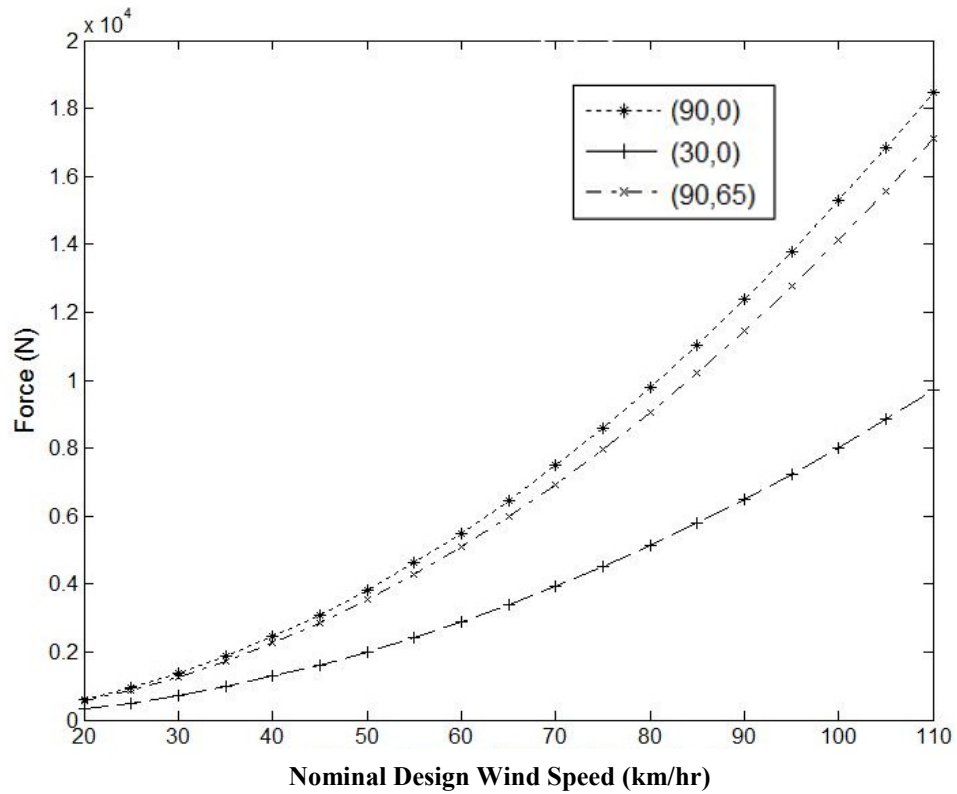
Figure 3-19: Normal force (*Fx*) as a function of nominal design wind speed for different azimuth and elevation angles.
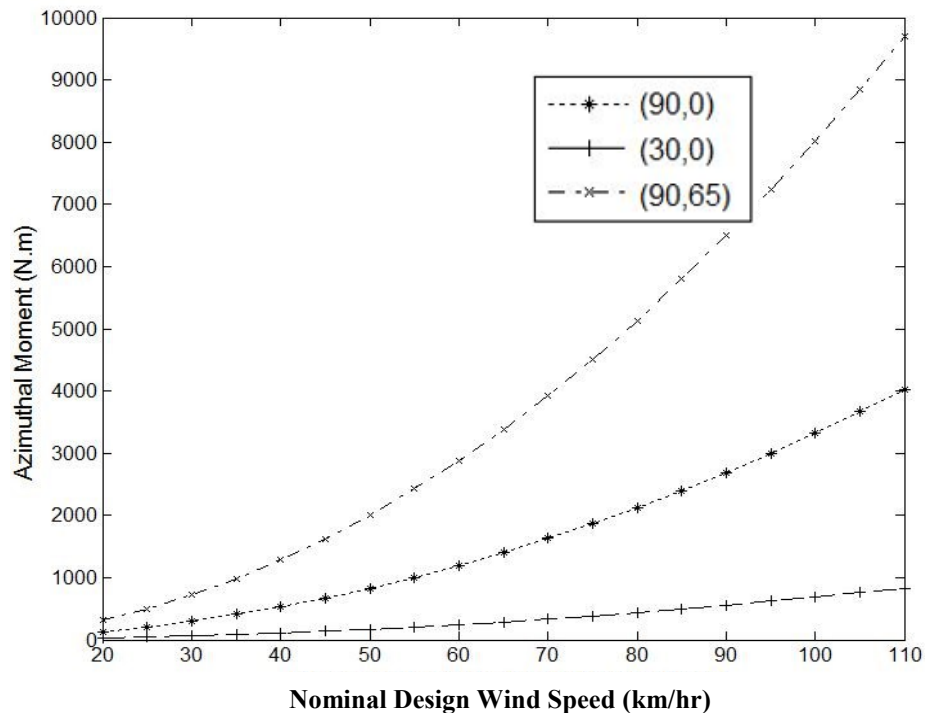
Figure 3-20: Azimuthal moment as a function of nominal design wind speed for different azimuth and elevation angles.
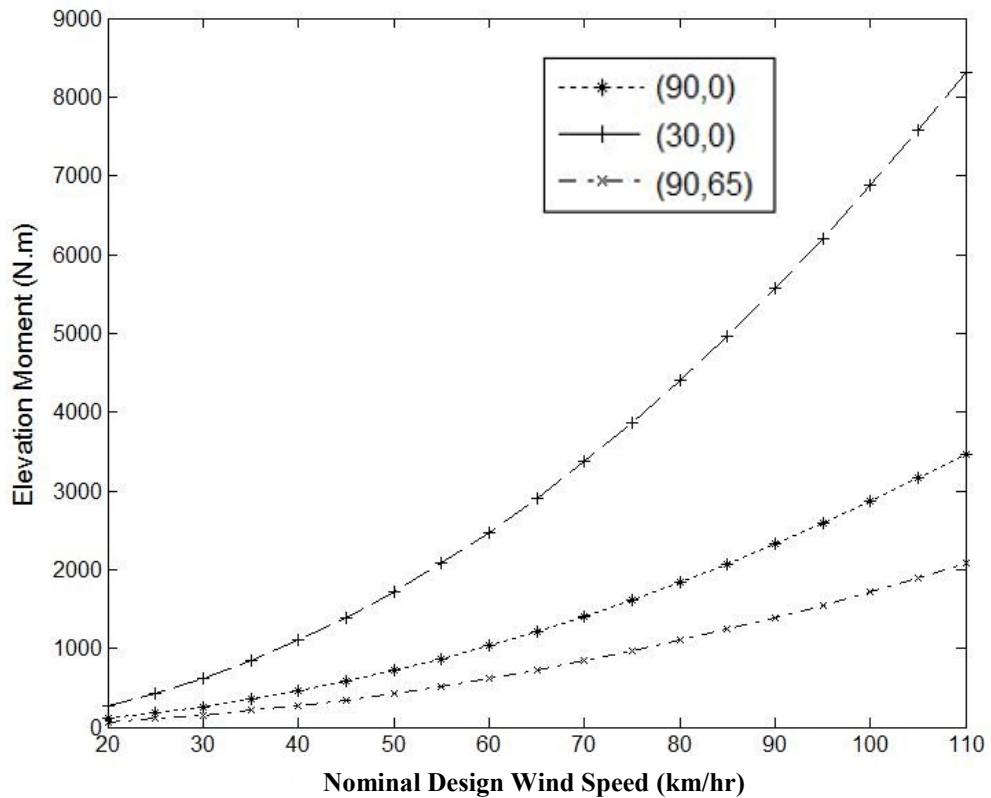
Figure 3-21: Elevation moment as a function of fundamental design wind speed for different azimuth and elevation angles.

The maximum azimuthal, elevation and normal forces are all observed for different heliostat orientations. Thus, for the purposes of designing the structure for survivability, it is reasonable to take the maximum azimuthal and elevation moments and normal force presented in the plots. This will ensure that, regardless of the assumed heliostat orientation, the wind loads applied in the analysis are conservative.

3.6.2 Pillar concept comparison FEA

A finite element was used to determine which of the two chosen configurations offered the highest rigidity and strength under the specified loading conditions. This section covers the method by which a final configuration was chosen. Virtual models of the configuration are shown in Figure 3-22.
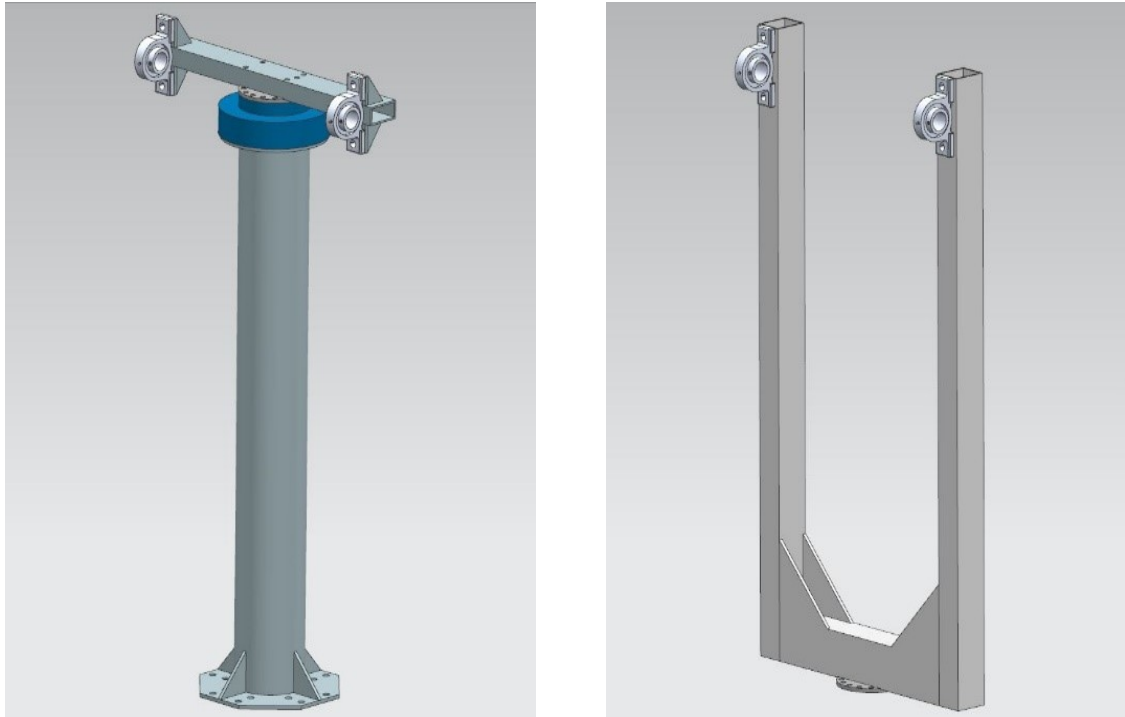
(a) Single steel tube pillar   (b) U-shaped rectangular tube steel pillar

Figure 3-22: Virtual models of the two candidate concepts.

Figure 3-22a shows the single steel tube pillar concept design with a rectangular steel tube cross member to mount the mirror facet backing structure. The selection of the slew drive actuator (shown in blue), which provides the azimuthal rotation required, is detailed in Section 3.6.6. Figure 3-22b shows the alternative, less conventional concept that incorporates a U-shaped rectangular tube steel pillar instead of a single pillar tube. In this concept the slew drive is installed at the bottom flange of the U-beam.

It is important to maintain backing structure and base mounting geometric similarity, to allow for an instructive comparison between the two pillar concepts. The two pillow block bearings are common facet backing structure mounting points, and both concepts are attached to a base foundation through a flange connection (shown in Figure 3-24).

An FEA model was constructed and subjected to the simplified wind loading model normal loads. Fixed constraints where added to the flanged connections. Deflection in the pillar concepts was observed under worst case wind loading and not under operational wind loads. Figure 3-23 shows the deflection (in millimetres) for both pillar concepts.
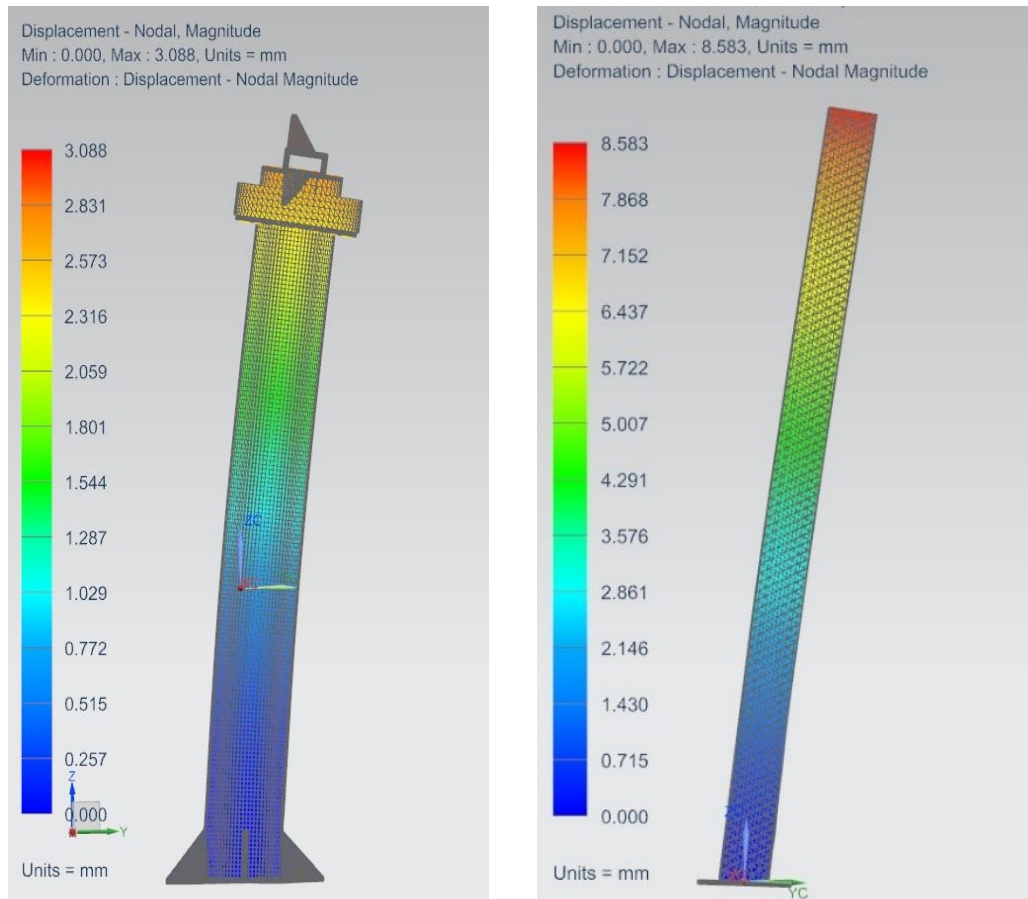
(a) Single steel tube pillar   (b) U-shaped rectangular steel tube pillar

Figure 3-23: Deflection of both pillar designs (10% deflection magnification).

Under a 28 m/s (100 km/hr) wind and the weight of the mirror backing structure, the maximum deflection for the single tube is 3.088 mm, and 8.583 mm for the U-shaped beam. Both design concepts show the same location where maximum deflection occurs; at the pillow block mounting points.

The single pillar design out performs the U-shaped pillar in deflection and provides an added advantage of having the slew drive actuator closer to the centroid of the mirror facet backing structure. This will significantly reduce the amount of bending moment the actuator is subjected to as compared to mounting it approximately 1.5 m away from the fixed foundation, causing a greater lever arm, as it would in the U-shaped concept. The single pillar was therefore shown to be the most suitable in terms of rigidity under a maximal normal loading.

3.6.3 Structural finite element model

A complete FEA model was required to resolve the deflections and stresses occurring throughout the heliostat structure, taking into consideration interactions among its constituent components. The loading schedule for a 100 km/hr wind, based on the Peterka and Derickson (1992) wind loading model associated with a heliostat with an aspect ratio of one, is stated in Table 3-6.

Table 3-6: Wind loading schedule based on the Peterka Derickson model.

Load	Description	Magnitude
F_x	Normal Force acting on heliostat reflective surface.	16 kN
Azimuthal Moment	Moment which causes rotation of the heliostat reflective surface in the azimuthal direction	8 kN.m
Elevation Moment	Moment which causes rotation of the heliostat reflective surface in the elevation direction	7 kN.m

These loads represent the worst-case loading for the most significant wind direction and heliostat orientations. The FEA software package, Siemens NX™, used in this study allows the use of one, two and three-dimensional meshing of geometry, as well as the capability to carry forward component meshes into an assembly mesh. This feature allows the user to mesh each component separately and iterate a sample load case to make sure that there is mesh independence. It was observed that Siemens NX™ provided a fairly accurate estimate of a mesh size which would lead to mesh independence.   Figure 3-24 shows the complete structural assembly with the load being input as a single, effective resultant force vector (in red) acting at the points of contact between the mirror backing frame and the cross beam as well as fixed constraints shown in blue.
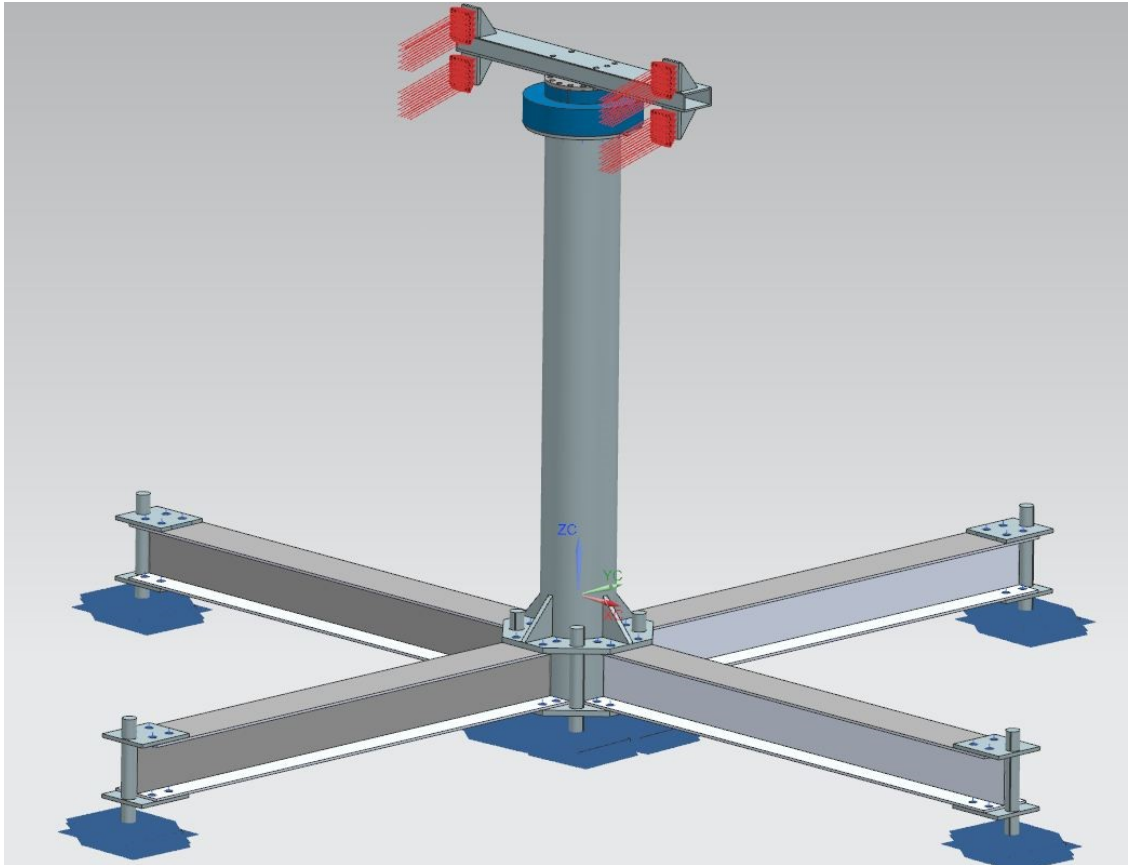
Figure 3-24: Structural FEA model showing load vectors (red) and constraints (blue).

The structural members of the heliostat are primitive shapes and thus void of complex geometries which resulted in there being no need for any mesh refinement techniques. The standard mesh elements suited the model well, apart from the bolt holes. Figure 3-25 shows a magnified view of the mesh applied at the most complex part of the model and Table 3-7 describes the mesh properties used.
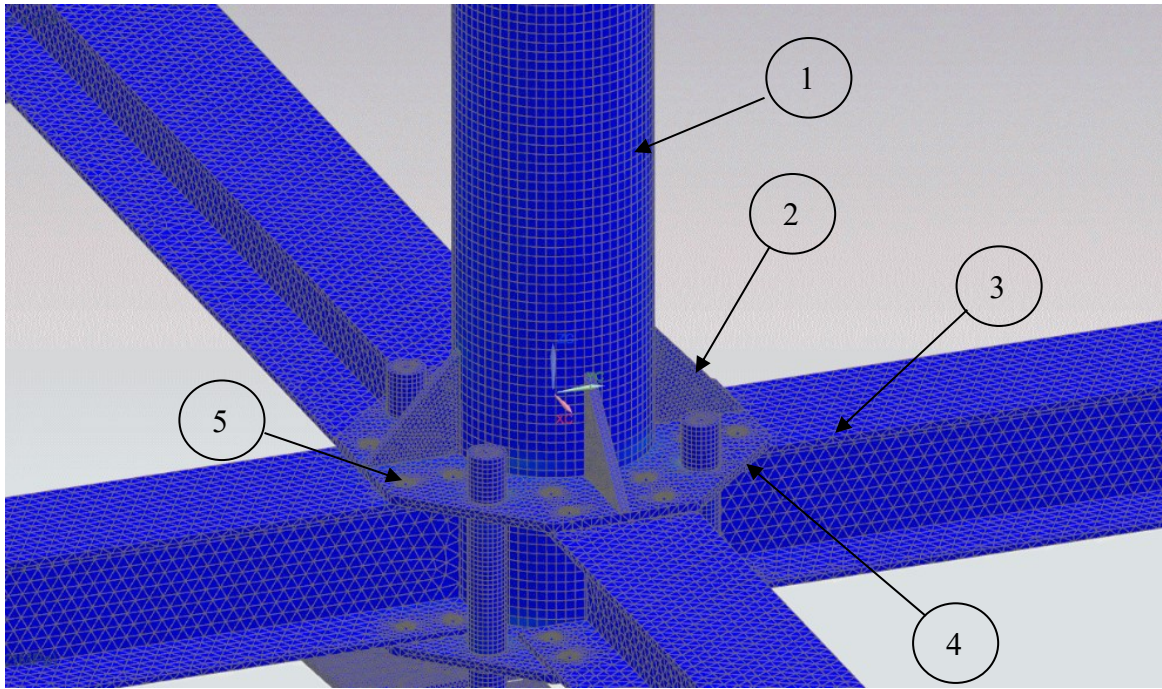
Figure 3-25: Mesh at the junction between I-beams and pillar tube.

Table 3-7: Mesh properties for structural FEA model.

#	Component / Feature	Element Type	Element Size (mm)	Meshing Method	Mesh Refinement
1	Tube Pillar	Quad	15	Sweep	None
2	Ribs	Tetrahedral	3	Sweep	None
3	I-beam	Tetrahedral	15	Sweep	None
4	I-beam Mount Plate	Tetrahedral	10	Sweep	None – except at bolt holes
5	Bolt Holes	Tetrahedral	2	Sweep	Increased number of nodes along inner edge of bolt hole by decreasing local mesh size to 2 mm

Components such as the cross-beam were meshed using a standard swept tetrahedral mesh. Other bolt holes utilised the same mesh refinement method as stated in Table 3-7. The bolts where modelled using one dimensional Type 2 Rigid Body Elements (RBE2) with an associated standard bolt material specification (Class 8.8, quenched and tempered carbon steel).

The use of 2D shell meshes was investigated, however it was observed that there was an insufficient mesh density between the 3D and 2D mesh joins. In this particular case, stresses that were developed in the regions where components are joined were more important to the analysis than that of the stress developed within the components themselves. The decrease in

computational expense was not justified by the decrease in stress capture in these significant regions of the model; hence the entire model was specified to utilise three-dimensional mesh elements.

Structural FEA results

Finite element analysis of the overall structure provided insight concerning the survivability of the bulk of the heliostat structure under 100 km/hr winds, and considered the full wind load model.

The structural components of the heliostat were divided into three major regions and were then analysed. These areas were the cross beam where the primary load force is transmitted from the mirror backing structure, the connection between the I-beams (foundation) and tube pillar upright, and the bolted connections. These three major regions were recognised as the most likely regions in which failure could occur. The rationale here being that the I-beams or steel tube pillar would not directly fail due to plastic deformations or buckling as these components are manufactured and specified for more severe loading applications (civil infrastructure and construction) that may occur when used in the operation of a heliostat, which was later confirmed by the insignificant levels of stress placed on these components.

Viewing the superimposed Von Mises stress plot over entire structural model, as shown in Figure 3-26, high stresses occur in two of the three major regions. The bolted connections are addressed specifically later in this section.
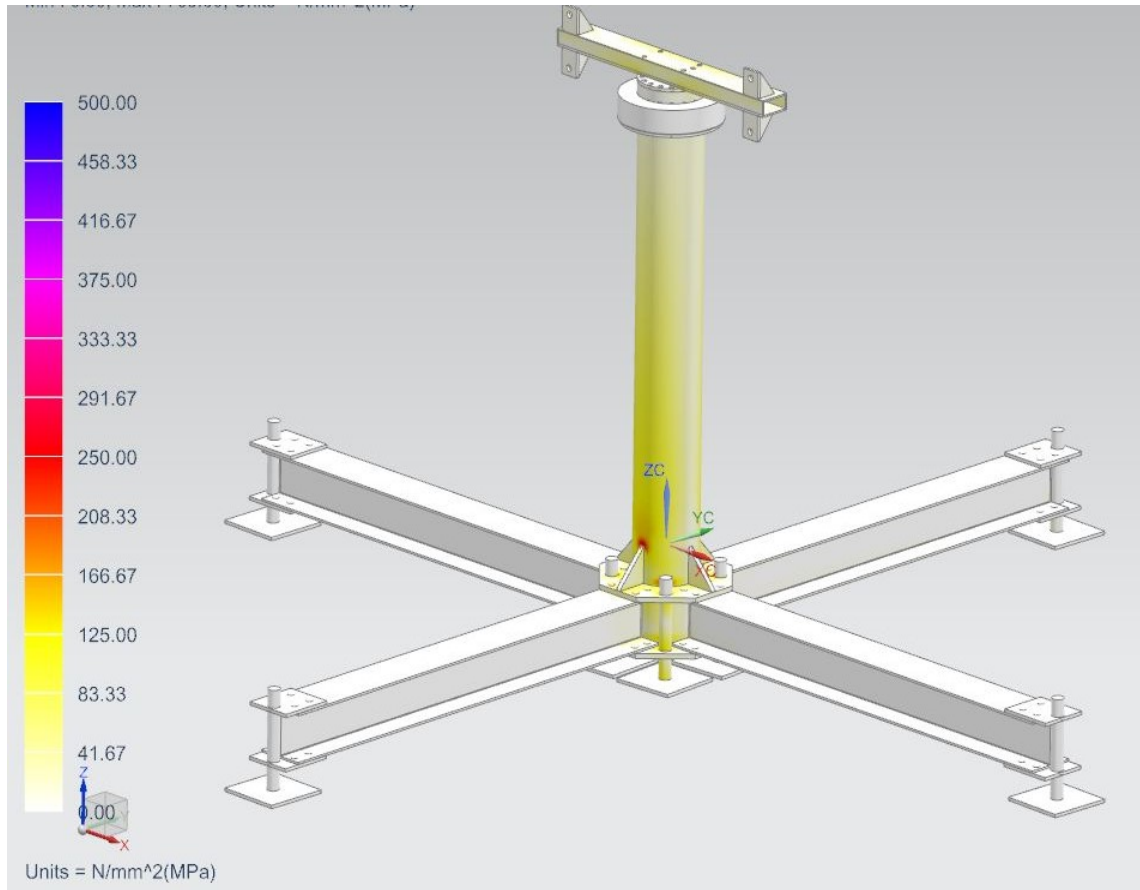
Figure 3-26: Von Mises Stress throughout the entire structural assembly.

It is evident that high stresses develop primarily within the tube pillar and on the cross bar. There is very minimal stress formation in the structural I-beams for the specified loading. Safety factors of approximately 1.5 - 1.8 (based on a yield strength of 355 MPa for the S355 structural steel used in construction of heliostat) are observed over much of the heliostat structure.

The major stress formations can be observed at the base of the pillar, where the I-beams (foundation) are attached to the pillar, as shown in Figure 3-27.
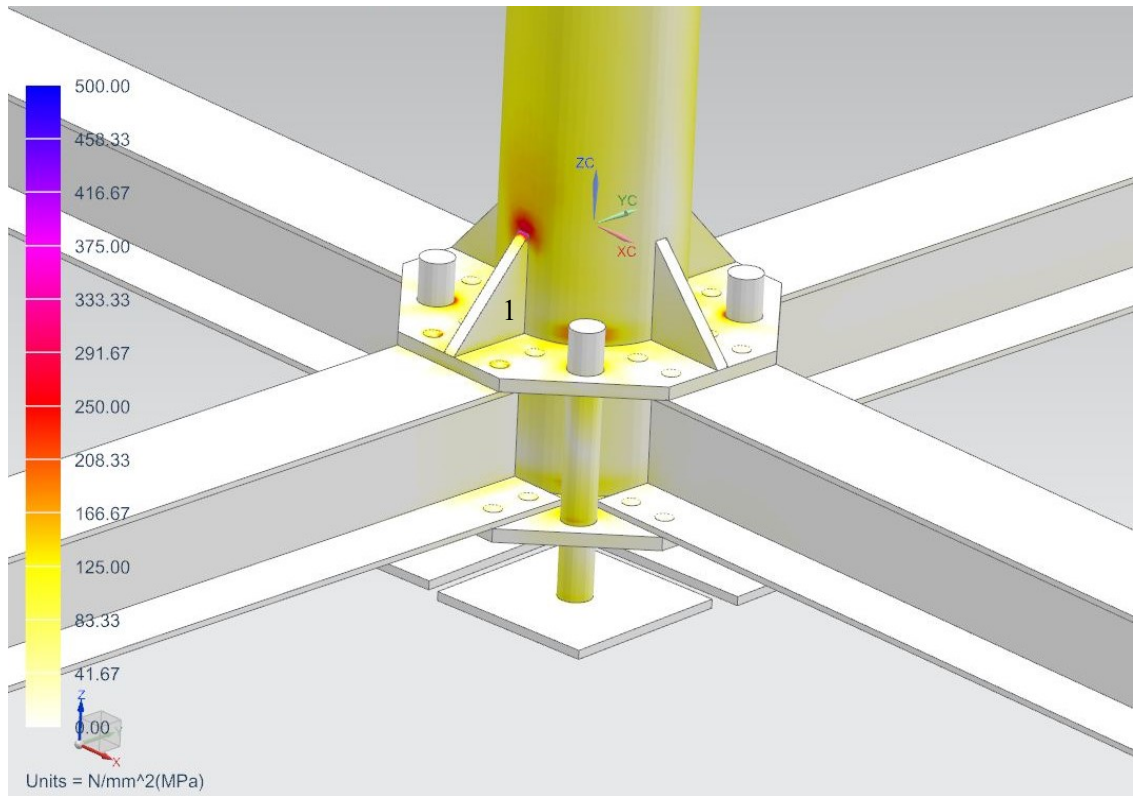
Figure 3-27: Superimposed Von Mises stress plot on connection region between I-beams and pillar.

There are large stress concentrations at the sharp ends of the support ribs on the I-beam mount plate which was expected prior to the FEA analysis. Safety factors of between 1 and 1.2 can be calculated at the upper vertex of the support rib triangle (labelled (1) in Figure 3-27). Changing the design of these ribs significantly was opted against as the stress concentration would not lead to a catastrophic failure of the heliostat structure. Also, one can easily misinterpret the severity of the Von Mises stress plot as it may be an artefact of the solution to the stress equations across any acute elements in the mesh. As such, there were no significant changes to the design after execution of the overall structural FEA.

The region in which catastrophic failure could occur is at the bolted connections between the I-beams and the tube mounting plate. Grade 8.8 carbon steel bolts were chosen due to their wide availability and common use in structural applications. Class 12.9 steel alloy bolts (the next grade up from 8.8) would have been expensive and have an unnecessarily high yield and ultimate tensile strength for this application. The overall FEA model was used to validate the suitability of the selected bolts. Figure 3-28 shows the tensile forces present in each bolt under worst case loading.
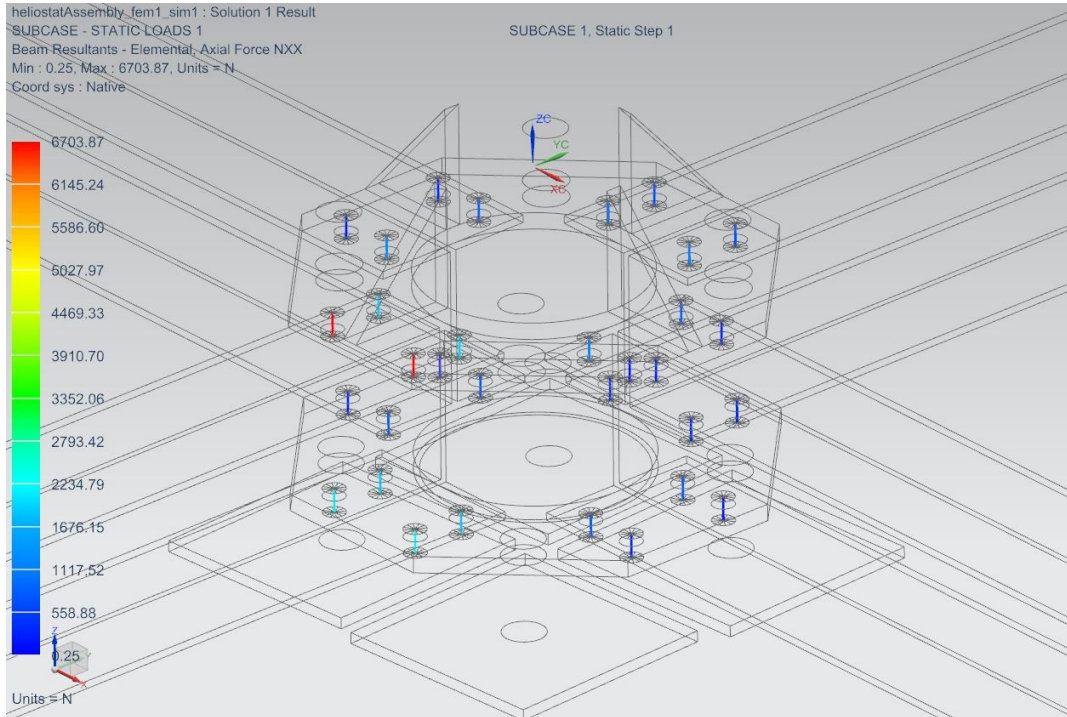
Figure 3-28: Axial force induced in bolts under wind loading.

The maximum tensile force induced in the bolts is approximately 6.7 kN, which equates to a maximum tensile stress of approximately 35 MPa, which is well within the ultimate tensile stress of the bolts. Apart from tensile force, a plot of the compressive force that is present between mating components can be visualised. Figure 3-29 shows a superimposed plot of the compressive force between the mating components.
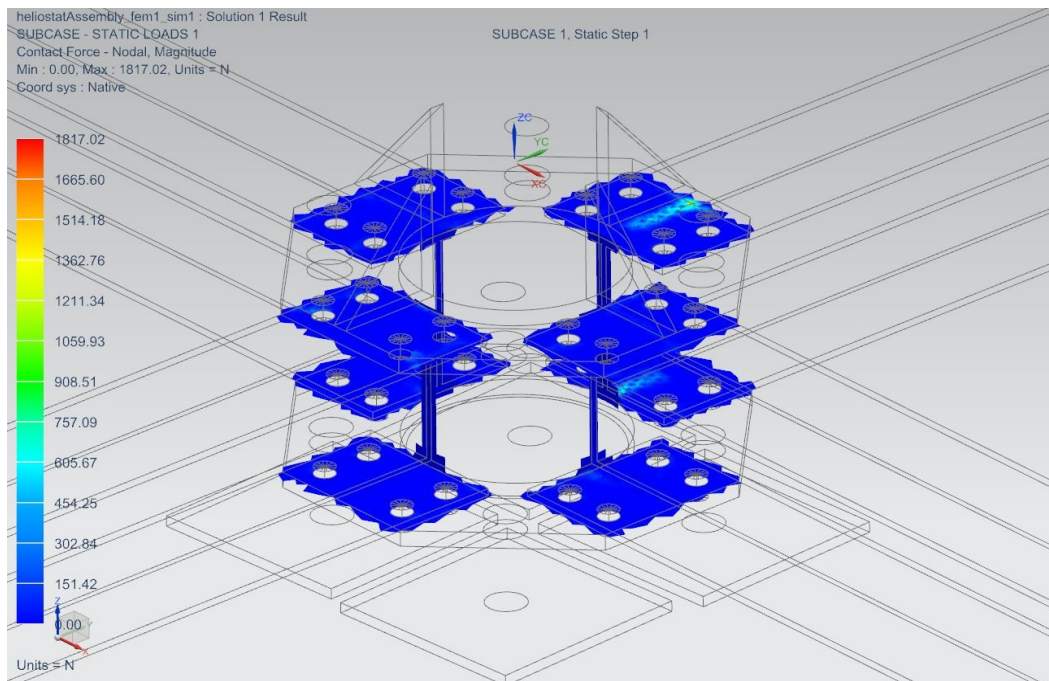
Figure 3-29: Compressive force between mating components.

There are significantly higher compressive forces on the two posterior I-beams directly under the support ribs although these forces would not cause any significant plastic deformation or failure as they are supported by the middle stem of the I-beam.

No significant design changes were made after the FEA was completed. This was partly due to the use of structural load-bearing components that are designed for far greater loads than what was expected in the case of a 9 m² heliostat. Safety loads where observed as low as 1 in very localised areas of the model, especially at the acute corners of the support ribs, however, these are stress concentrations that could be an artefact of the mesh geometry or do not indicate complete structural failure.

3.6.4 Mirror backing frame design and FEA

Traditional heliostat mirror backing structures are typically constructed out of a steel lattice framework. Steel frames are often heavy and require treatment to protect against the elements.

During the concept selection phase (see Section 3.5.3) various conventional and unconventional heliostat mirror frames were analysed as per their desirable traits, and those that were selected satisfied the design constraints associated with this study. It was shown that an aluminium tube backing frame would best suit the need for low weight, low material quantity and rigidity (if extruded in geometrically rigid shapes since aluminium is not often associated with high rigidity). The Aerospace Systems Research Group (ASReG) of the Discipline of Mechanical Engineering had previous experience with a product range that appeared to fit these criteria. The product range in question comprised a variety of standard extruded aluminium profiles of various dimensions. Examples of available extrusions are shown in Figure 3-30.

Figure 3-30: Samples of available aluminium extrusions.

One of the attractive properties of these extrusions, apart from offering a high rigidity-to-weight ratio, is the fact they do not require any welding in assembling a structure. The unique design allows for the extrusions to be attached to one another using standard metal brackets with slotted T-bolts.

There are a few local suppliers aluminium extrusions, however, these extrusions did not offer the quality and tolerances that some of the international suppliers offered. From prior experience using German-made extrusions from Bosch Rexroth™, it was found that this brand offered the highest level of precision and rigidity than other brands. Negotiations with the local distributor of the Rexroth™ range permitted the discounted purchase of the necessary extrusions in cut-to-size and corrosion protected form.

Choosing the dimensions for the extrusions was a key task. Basic space constraints and discussions with the local distributors narrowed down the choices to square cross-sections ranging in size from 40 mm x 40 mm to 50 mm x 50 mm.

A one-dimensional FEA model of the heliostat's reflective surface and backing structure was developed for analysis. The use of linear one-dimensional elements to represent the complex cross-section extrusions allowed for very rapid solution times whilst capturing sufficient stress and deflection information during the solution procedure. One disadvantage of this technique is that it is difficult to model connecting components such as brackets and fasteners, and the only available option to do so is to approximate the joints by means of rigid body elements. In reality, brackets and fasteners can allow for the connected components to move slightly relative to one another due to minute torsional strains, thus, accumulatively there can be significant increases in deflections observed in the structure in the real world. Figure 3-31 shows the FEA model and superimposed deflection plots for a 40 mm x 40 mm and 45 mm x 45 mm extrusions with a 20 km/h wind acting perpendicular to the mirror surface.
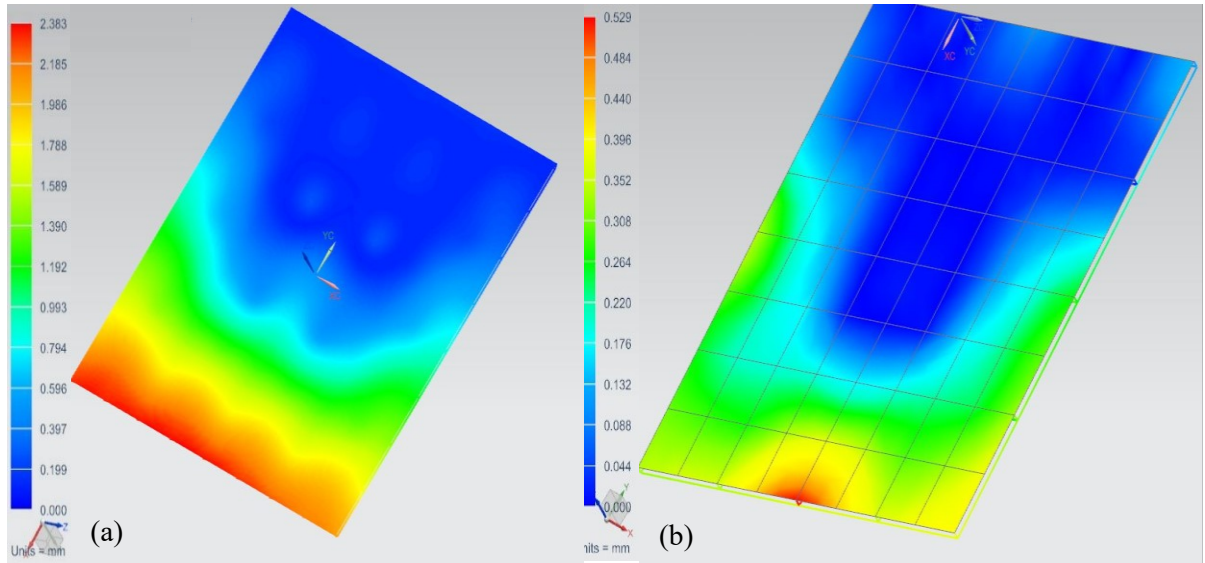
Figure 3-31: (a) Deflection plot for a 40mm side length square cross-section. (b) Deflection plot for a 45mm side length square cross-section.

The degree of deflection for a 40 mm x 40 mm extrusion is greater than that of a 45 mm x45 mm extrusion, as expected. From the model, an approximate maximum deflection of 2.4 mm in Figure 3-31(a) is observed as compared to the 0.53 mm of deflection in Figure 3-31(b). Larger profiles lead to lower deflections however it was concluded that these gains in rigidity did not outweigh the added cost and weight.

The FEA model also incorporated a 2D shell mesh which was representative of the polished aluminium mirror facets bonded onto the aluminium profile frame. This addition added to the overall rigidity of the entire mirror backing frame. Again, it must be noted that there was a limitation in the fidelity of the connecting elements used to connect the 2D shell to 1D elements and this could lead to inaccuracies in regards to the real deflection of the structure. The asymmetry in the stress plot is due to the addition of a rigid constraint which represents the connection between the rigid linear actuator and the mirror backing frame thus making the top half of the heliostat backing frame more rigid than the lower half.

The full wind model was also applied to FEA model for a wind speed of 100 km/h to analyse the survivability of the backing frame under that worst-case load. The stresses developed in the struts was of interest. Figure 3-32 shows the resulting Von Mises stress plot superimposed onto the FEA model.

67
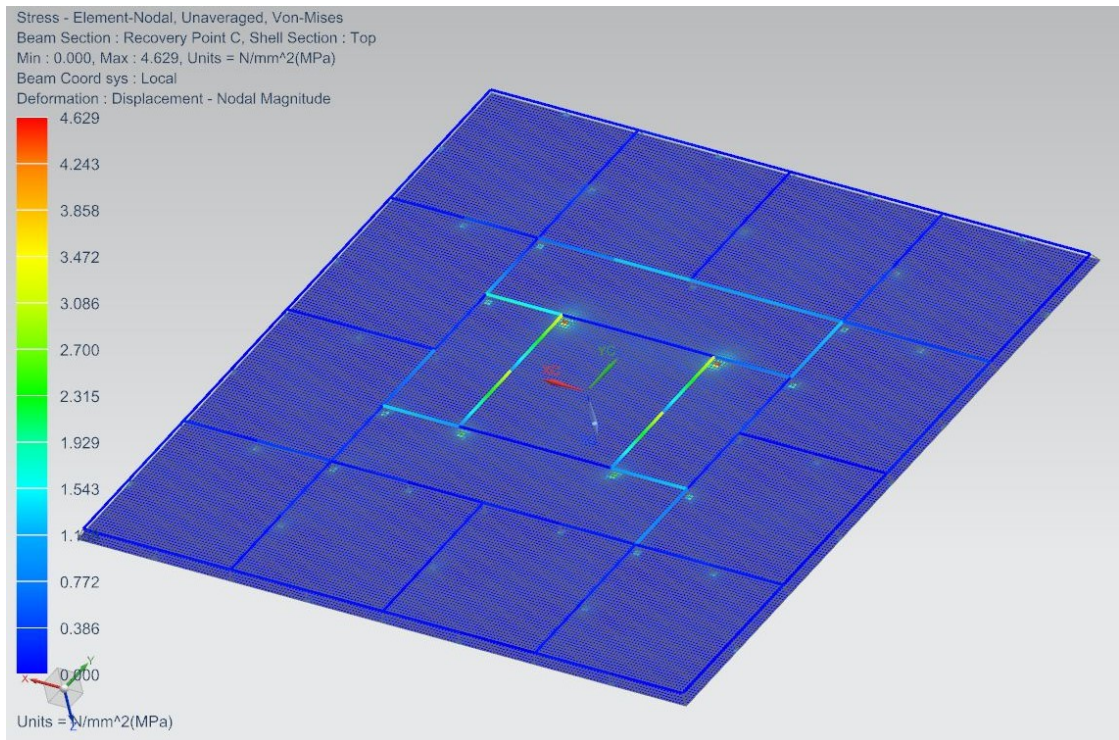
Figure 3-32: Von Mises stress developed in the extrusions during a 100km/hr wind.

The maximum stresses occur at the central struts where the cross beam of the heliostat structural upright attaches to the mirror backing frame. The extruded profiles offer exceptional rigidity and distribute the stress well such that no single member is stressed anywhere near its yield limit.

Although the FEA predicted little out-of-plane deflection, the use of rigid connecting elements within the model to represent the connecting brackets joining extrusions to one another may ultimately lead to discrepancies with reality. However, from a survival point of view, the mirror backing frame was shown to withstand a worst case loading due to 100 km/hr winds. Figure 3-33 shows a CAD rendering of the heliostat structural and backing frame assembly.

Figure 3-33: CAD rendering of heliostat structural components.

3.6.5 Mirror selection

As discussed previously, there are two major optical errors that incur a loss of performance in solar reflectors. It was shown that the sensitivity to slope errors in a mirror increases as the total surface area of the reflector increases. Commercial mirror manufacturers do not usually quote a characterised slope error as a product specification. This makes choosing a mirror based on slope error alone, difficult. On the other hand, reflectivity is a commonly quoted product specification for commercially available mirrors and thus it is not difficult to compare different mirror products based on this parameter.

Mirror selection for the heliostat, apart from optical quality, is largely effected by the design of the mirror backing frame. The backing frame designed for the heliostat is lightweight and does not offer some of the properties in which more traditional steel trussed mirror backing frames offer, such as manifold flat surfaces on which to mount specialised solar reflector films.

A few options where considered for use in the heliostat such as thin film reflectors, traditional silvered glass mirrors (commercial grade) and polished aluminium mirror facets. Table 3-8 lists some of the advantages and disadvantages of the three types of solar reflectors considered.

Table 3-8: Advantages and disadvantages of reflector options.

Reflector Type	Advantages	Disadvantages
Reflective Film	- Very lightweight. - Abrasion resistant/Durable. - Resists delamination due to UV exposure. - Cheaper than traditional glass mirrors.	- Requires rigid substrate to be bonded to. - Substrate bonding process requires specialised equipment and preparations.
Silvered Glass Mirrors	- Low slope errors due to its rigidity. - Does not require a substrate to bond to. - Easily available locally at a potentially low cost.	- Susceptible to cracking and degradation of reflectance under long-term UV exposure. - Low abrasion resistance to airborne particulates carried by higher wind speeds. - Far heavier than thin film and polished aluminium reflectors.
Polished Aluminium Facets	- Capable of high reflectance. - Lightweight. - Does not require substrate to bond to. - Abrasion resistant/durable. - Very little degradation of reflectivity due to long-term UV exposure.	- Can flex if not evenly supported by rigid members. - Not easily available locally.

There are distinct advantages and disadvantages to all three reflector types. However, there are some disadvantages that make the use of a particular type of reflector unsuitable for use with the chosen backing frame design. The thin film reflector's major disadvantage is the need for a substrate to which the film must be bonded. The design of the backing frame does not offer a large flat surface area in which bonding can take place. Adding a rigid substrate to the backing frame design would increase the weight of the structure and thus mitigate the weight savings made by using aluminium extrusions rather than a steel truss lattice. Traditional silvered glass mirrors would also largely increase the total mass of the heliostat mirror assembly.

Polished aluminium mirror facets were an attractive option as they are lightweight and the chosen backing frame design would offer an ideal flat mounting area for such reflectors. GSET could draw on positive experiences and knowledge on the use of polished aluminium mirror facets in similar sized heliostats from collaboration with the Stellenbosch University's Solar Thermal Energy Research Group (STERG). A critical piece of information gained from this collaboration was the discovery of a Slovenian company (SAT-Control) who specialised in manufacturing polished aluminium facets specifically designed for heliostat reflectors.

The facets ordered from this company offered superior rigidity to regular polished aluminium sheets. The facet design included a honeycomb composite material which was sandwiched between two aluminium sheets. The rigidity offered by these facets meant that they could be directly attached to the mirror backing frame. The facets could be easily cut to the lengths required using a large guillotine. The mirror facets have a reflectivity of 88% and a thickness of 4 mm. An epoxy clear coat is added to the surface of the polished aluminium to increase abrasion resistance and protect the polished surface from scratches and degradation due to UV exposure.

3.6.6   Azimuth and elevation actuators

The heliostat was designed to track the trajectory of the sun about both the azimuthal and elevation axes. It thus required two actuators; one per tracking axis. Traditional T-shaped commercial heliostats typically employ slewing drive actuators. The slewing drive actuator is compact and allows for relative motion between columnar structural components. It is also used widely in the actuation of industrial cranes. The design of the present heliostat lent itself well to the use of a slewing drive actuator for its azimuthal tracking axis as it is similar to traditional T-shaped heliostats. Figure 3-34 shows a CAD rendering of the slewing drive considered for use as the azimuthal axis actuator.

Figure 3-34: CAD rendering of the slewing drive actuator.

As with the polished aluminium mirror facets, the collaboration between STERG and GSET allowed for the selection of a reliable slewing drive actuator supplier. STERG has previously purchased slewing drive actuators from the Chinese company H-FANG. The company supplies specialised solar slewing drive actuators at a fraction of the cost of most European suppliers.

In choosing a slewing drive for the heliostat, several key specifications were of importance including the flange diameter, maximum tilting torque, maximum holding torque, output torque and the maximum static axial force. The selected tube pillar diameter for the heliostat design was the defining factor when deciding on the specific slewing drive actuator employed. The tube pillar diameter was 200 mm, thus a tube flange pitch circle diameter (PCD) was designed to meet the specification of the slewing drive that met the torque requirements. Using the full wind loading model and the approximated weight of the heliostat structure, it was possible to set a maximum holding torque and tilting torque requirement. As per Table 3-6, the maximum azimuthal torque and elevation moment under a 100 km/hr wind is 8 kN and 7 kN, respectively. Table 3-9 shows the specifications for two prime candidate slewing drives from H-Fang.

Table 3-9: Slewing drive specifications.

Model	Output Torque	Max. Holding Torque	Max. Tilting Torque	Max. Static Axial Load
PE7A	1.5 kN.m	10.4 kN.m	13.5 kN.m	133 kN
PE9A	6.5 kN	38.7 kN.m	33.9 kN.m	338 kN

The PE9A drive has considerably larger capabilities in terms of output torque, however, both models would be able to actuate the azimuthal axis of the heliostat. Both drives are driven by a single 24 V DC motor and include high resolution quadrature encoders for position control. The PE7A did not fit the dimensions of the tube pillar as its PCD is 203 mm; only 3 mm larger than the steel tube/pillar diameter. The PE9A would prove a better choice as the PCD is 270 mm which would allow it to be seated well on a 270 mm diameter flange welded onto the 200 mm diameter tube/pillar. The capabilities of the PE9A were more than adequate for the use in the present heliostat design, and would allow for the possibility of increasing the overall size of the heliostat surface area in future, if required. This series of slewing drive actuators have been used successfully in STERG's Helio-40 heliostat array (Larmuth et. al, 2014).

The elevation axis did not require the ability to be rotated through an angle of more than 90 degrees. In fact, as shown in Chapter 5, the elevation axis does not rotate through more than 45

degrees. A linear actuator was thus a good candidate for this axis, as this type of actuator typically has high resolution positioning abilities, handles high static loading and can be fitted with high resolution quadrature encoders. Once again, knowledge of STERG's heliostat array actuators made the selection of the linear actuator straight forward, and the same supplier (SAT-Control) used in sourcing the polished aluminium mirror facets was utilised. The two primary specifications for a linear actuator are the stroke length and maximum static load. The stroke length would not exceed half the length of the mirror backing frame (1500 mm). A linear actuator with a stroke length of 900 mm was therefore chosen as this was the minimum stroke length available from the supplier at the time of purchase. The maximum static load capacity was indicated to be 1500 kg, which was more than adequate in terms of supporting and actuating the mirror backing frame. The linear actuator, shown in Figure 3-35, came fitted with high resolution quadrature encoders used for position control.

Figure 3-35: Linear actuator used for actuation of the elevation axis.

3.7 Conclusion

This chapter explains the methodology used in designing SERAFF's heliostat. The methodology was broken down into several aspects. These aspects included: solar tracking, heliostat sizing, optical analysis using ray tracing, actuator selection as well as conceptual and final designs. Astronomical equations where used to approximate the solar position as compared to an opto-mechanical approach. The solar position was utilised in calculating the required heliostat position.

The size of the heliostat is primarily dependent on the size of the primary concentrator. A geometrically based approximation of the maximum theoretical power output of a parabolic primary concentrator was developed. This model was used to calculate the diameter of the parabolic concentrator needed to achieve SERAFF's specified power output. The model was validated against real solar furnaces around the world. It was found that the model approximated the power output for these solar furnaces within 12% of their published power output values. The model suggested that a 3 m diameter parabolic concentrator would be required. Thus, the minimum size of heliostat required would be 3 m x 3 m to allow for satisfactory illumination of the primary concentrator aperture. Following an optical analysis and illumination study, and after

taking into consideration the practical and financial constraints placed on the project, it was decided that a 3 m x 3 m was the most suitable size for SERAFF's heliostat.

Having established the required dimensions of the heliostat, conceptual designs where drawn up. Both, conventional and unconventional heliostat design elements where considered leading to a merger of elements inspired by commercial and research-based heliostats.

Wind loading models where used to determine the wind loads on the heliostat under a 100 km/hr wind speed. This offered good insights into the behaviour and strength of the heliostat structure under worst case loading. These wind loads where also used in determining the type and model of actuators required for both the azimuthal and elevation axes. It was decided that a slewing drive and a linear actuator were to be used for the azimuthal and elevation axes, respectively.

Chapter 4.   Fabrication Process

4.1 Introduction

Fabrication of the heliostat commenced once the final components where designed and the corresponding working drawings where complete.

According to Stone and Jones (1999), there are two dominating sources of geometrical error in a heliostat that ultimately affect its tracking accuracy and optical performance. These are 1) azimuthal/elevation axis tilt, and 2) mirror alignment/canting non-orthogonality errors. The first of these two errors involve the tilting of either of the two rotational axes, most often it is caused by a tilt in the heliostat pedestal/pillar during fabrication (Stone and Jones, 1999). The second error involves misalignment of mirror facets and warpage of the mirror facets themselves (slope error) which can be exacerbated during the fabrication and assembly of the mirror backing structure. These two errors are decreased with an increase in the accuracy of fabrication. Thus, the fabrication processes used were a major consideration in this study.

There is a fully functional workshop at the University of KwaZulu-Natal's Discipline of Mechanical Engineering. The workshop houses multiple lathes, computer numerical controlled (CNC) machines, drill presses and milling machines as well a variety of hand/power tools.

This chapter will describe the fabrication processes used to fabricate all major components of the heliostat as well as its installation at a temporary SERAFF test site. Figure 4-1 shows a CAD rendering of the heliostat with labels describing the core structural components.
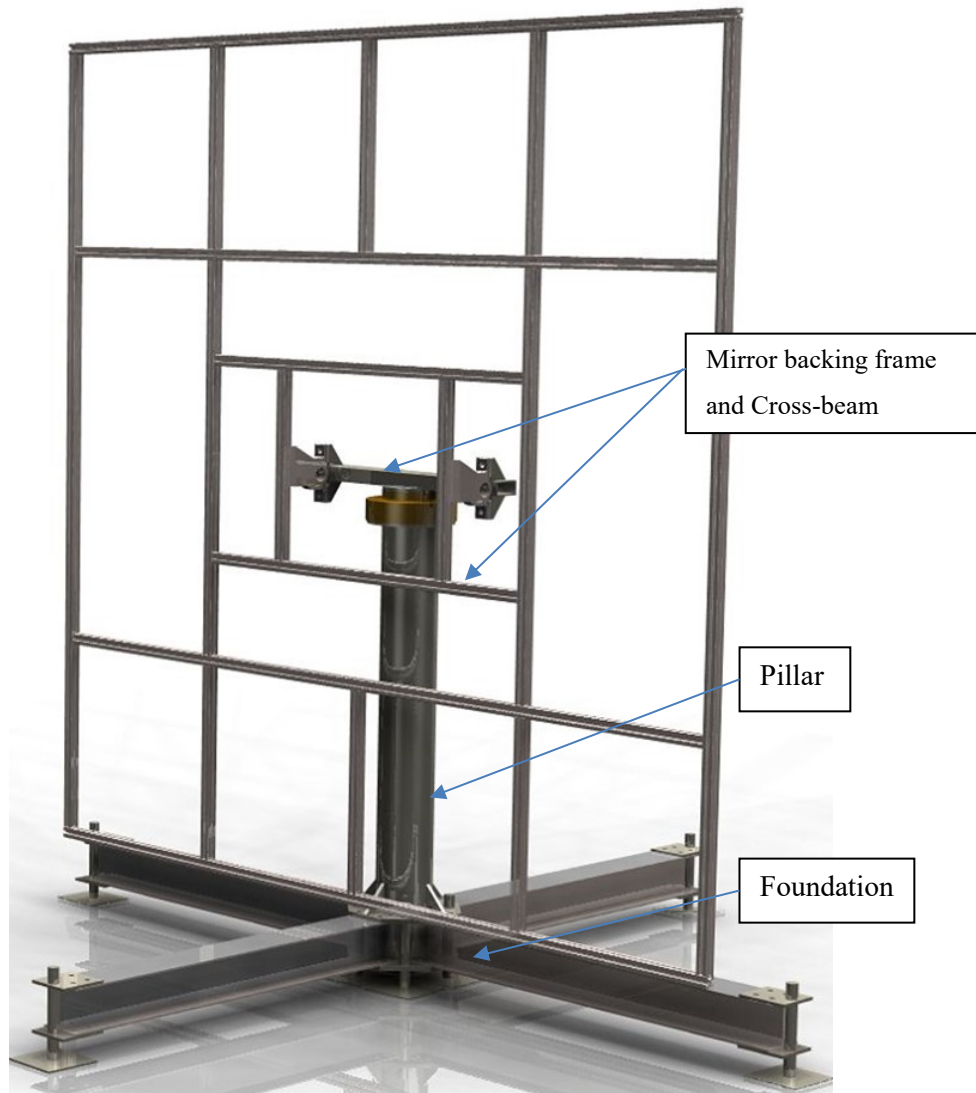
Figure 4-1: CAD rendering of the heliostat showing the core structural components.

4.2 Pillar

The pillar forms the core structural component of the heliostat as all other structural components are either directly or indirectly coupled to it. The pillar was primarily made from a structural steel alloy tube, 219.1 mm in diameter with a wall thickness of 4.5 mm. The tube was purchased as a 5 m length, and cut to the required length by first performing a rough cut using a mobile plasma cutter and a final cut using a horizontal bandsaw.

A particular challenge associated with remaining within the specified fits and tolerances among assembly components was achieving a close fit between the I-beam mounting plate and the pillar tube required for welding. The pillar tube was fabricated by rolling a flat sheet of steel into the required cylindrical shape and welding the free edges together. This process left a seam along the weld bead. This seam caused a deviation from the manufacturer specified tube diameter, thus

interfering with the close fit required. The seam was removed by grinding it flush to the tube surface using a ceramic pencil grinder. The outer diameter at the distal and proximal ends of the tube had to be ground down to achieve a close fit with the I-beam mounting plates and the tube, as illustrated in Figure 4-2a. Figure 4-2b shows the resulting weld bead between the I-beam mounting plates and the tube.
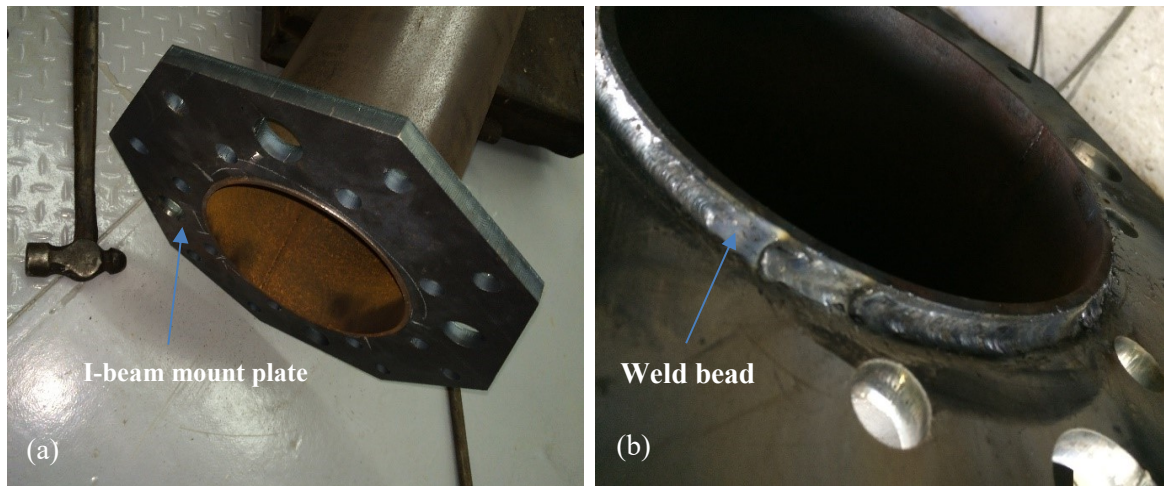
Figure 4-2: (a) Steel pillar tube with first I-beam mounting flange close fitted on slid on. (b) Weld bead after welding.

The fit between the I-beam mounting flange and the tube needed to be a close fit to align the flange perpendicularly to the steel tube, thus minimising play whilst welding. A short section of I-beam (labelled (1) in Figure 4-3a) was used to maintain the correct distance between the two I-beam mounting plates during the welding process, to avoid warpage. The arc welding process was employed using 6013 mild steel welding rods as the electrode. The 6013 welding rods where chosen for their versatility and deep weld penetration when welding structural or mild steel. A motor mounting flange (labelled (2) in Figure 4-3b) was welded onto the top end of the pillar to allow for attachment of the slewing drive.
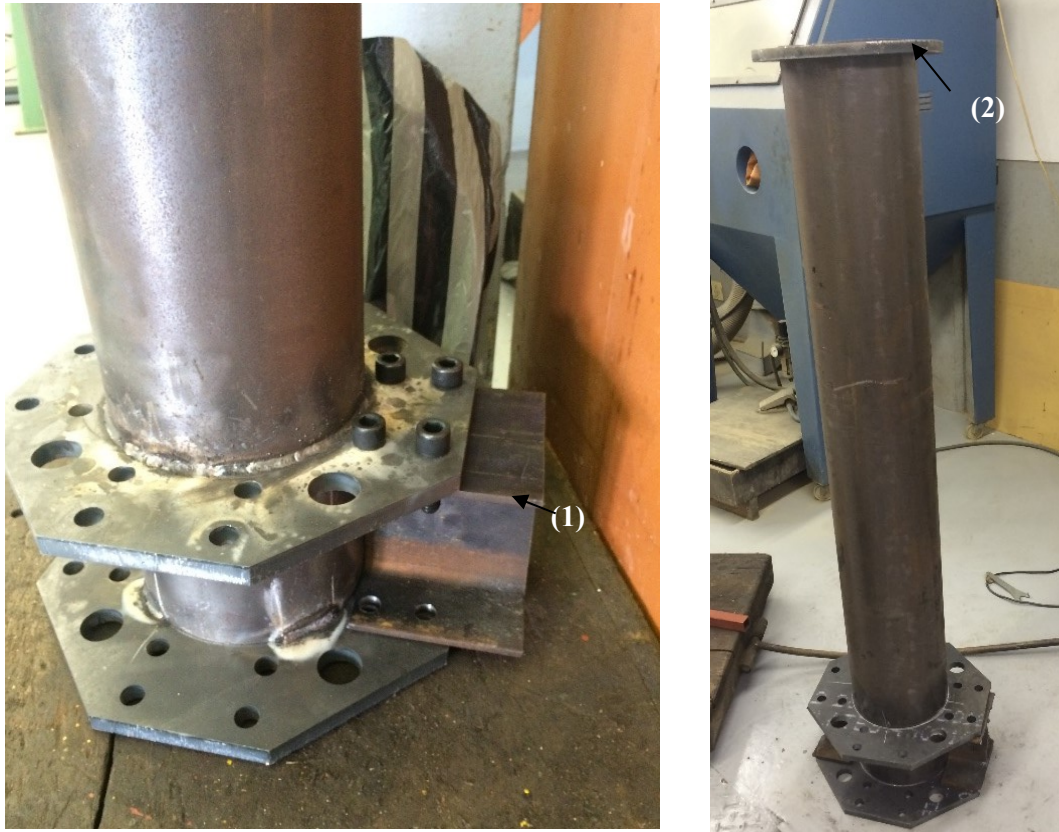
Figure 4-3: (a) Axial and rotational alignment of I-beam mounting plated using an I-beam section spacer (1). (b) Slewing drive motor mounting flange (2).

4.3 Foundation

The foundation was assembled using four lengths of structural I-beam sections which were bolted orthogonally to one another, to the pillar via the I-beam mounting plates. The I-beams where purchased in 6 m lengths and cut to the required lengths of 1.5 m using the horizontal band saw (shown in Figure 4-4a). Four 16 mm holes were drilled into the ends of the I-beams for M16 bolts. The M16 bolts were used to attach the I-beams to the I-beam mounting plate. Figure 4-4b shows a workshop technician cutting an I-beam to length on the horizontal band saw, as well as drilling preparatory pilot holes for the final 16 mm hole.
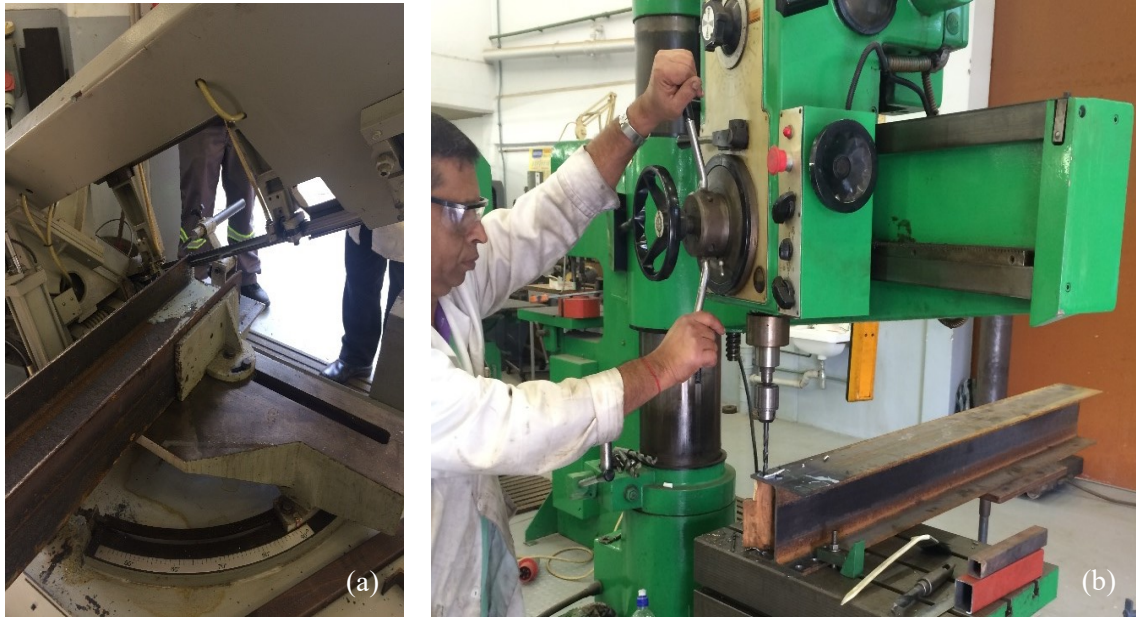
Figure 4-4: (a) I-beams cut to length using the horizontal band saw. (b) Pilot holes being drilled on the drill press.

Once the I-beams were cut and drilled, they could be inserted between the mounting plates and bolted in place. The last components welded to the foundation beams were the grooved steel rollers that enabled the heliostat to roll along a set of rails into and out of SERAFF's housing structure. These rollers were welded into place after the foundation beams where galvanised. Figure 4-5a and b show the rollers being welded to the underside of each foundation beam as well as the foundation and pillar bolted together, respectively. The foundation and pillar components were sent for galvanizing. The galvanizing process used was the hot-dip method which allowed for the inside surface of the pillar to be galvanised. No specific pre-galvanizing treatment/modifications (such as holes for run-off) where required since the components to be galvanised did not contain any closed volumes.

Figure 4-5: (a) Rollers being welded to the I-beams (b) Completed foundation (before galvanizing).

4.4 Backing frame and cross beam assembly

The mirror assembly comprised two primary structural components: the cross beam and the mirror backing frame. These two components where coupled to one another by two pillow block bearings through which 50 mm diameter steel pins were inserted.

The cross beam is a 100 mm x 50 mm steel tube that is cut to a length of 850 mm. Holes are drilled through the cross beam to allow it to be bolted onto the slewing motor. Steel gussets are welded onto the cross beam to mount the pillow block bearings as well as linear actuator brackets. These bearings house the 50 mm pins onto which the mirror backing frame mounts are attached. Figure 4-6 shows the complete cross beam bolted onto the slewing motor.
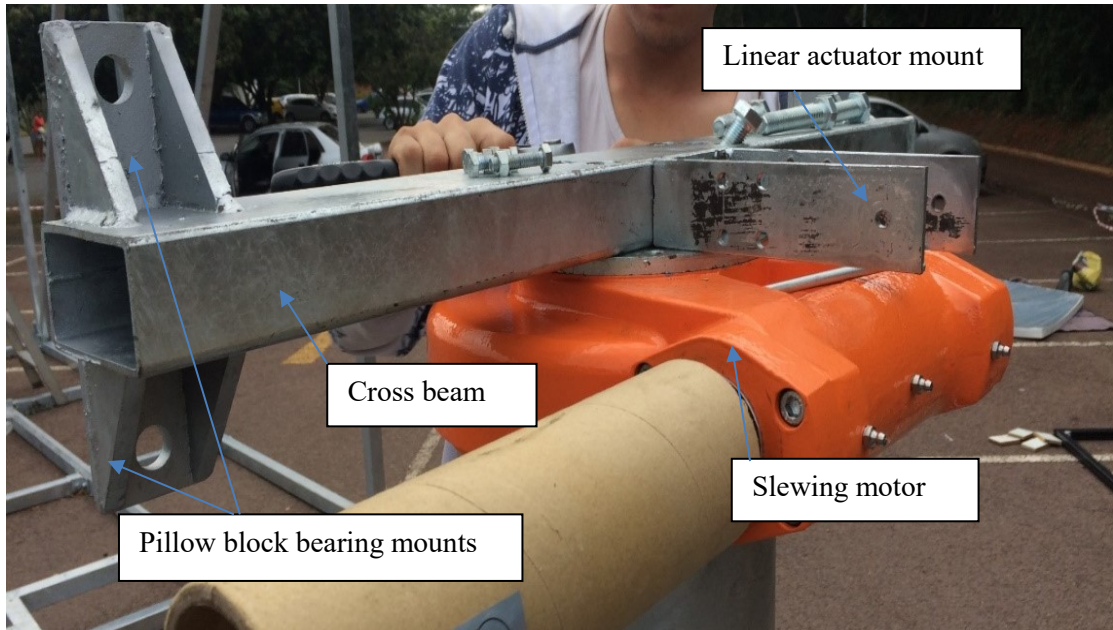
Figure 4-6: Cross beam bolted onto the slewing motor.

The mirror backing frame was constructed using aluminium extrusions that are easily coupled using cast aluminium brackets, thus no welding is required. Figure 4-7 shows the mirror backing frame being assembled.
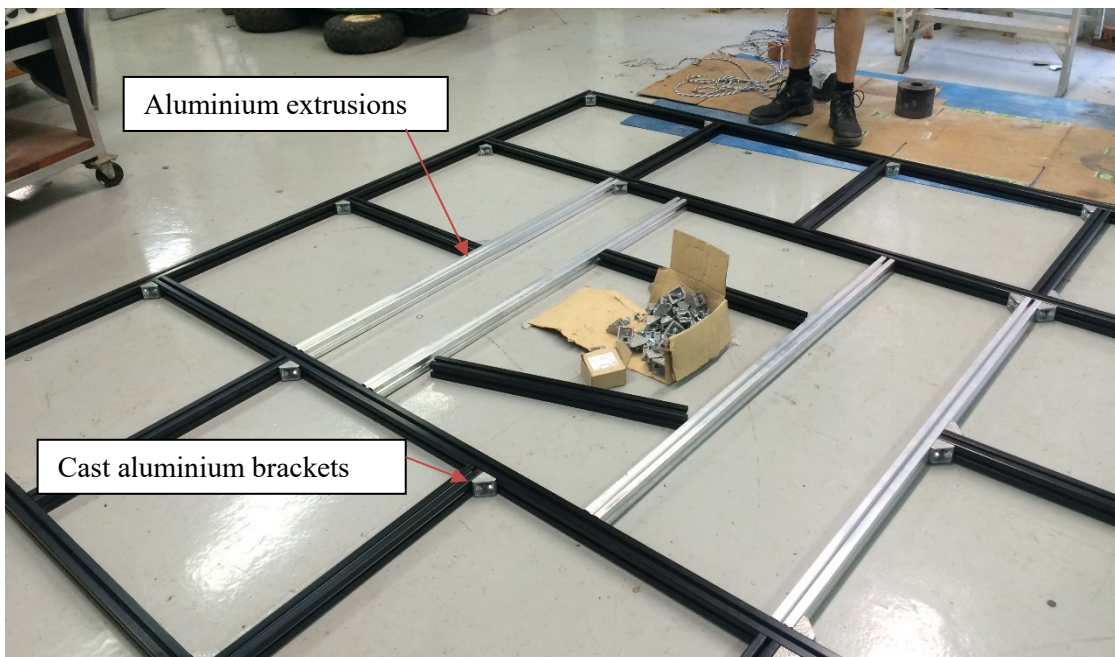
Figure 4-7: Assembling the aluminium extrusions using cast aluminium brackets.

The backing frame was assembled on an open floor space in the mechanical engineering workshop. This floor space was chosen because it had the most level and smooth flooring as compared to other locations within the workshop. Achieving flatness and perpendicularity between each aluminium section was not significantly dependent on the flatness of the floor in which it was being assembled. Rather, an advantage of using the Bosch Rexroth™ aluminium extrusions was that perpendicularity and flatness can be easily achieved through its accurately machined T-slots and flat mating surfaces. Therefore, if one insured the extrusions where perpendicular (using a steel 90° set square) to one another and the mating surfaces where flush, then flatness and perpendicularity is achieved when the cast aluminium brackets are slotted in to the T-slots and tightened correctly. A unique feature of the Bosch Rexroth™ cast aluminium brackets are the positioning tabs which slot into the T-slots which further removed any rotational misalignments between the bracket and the extrusion.

Dimensional accuracy was ensured by having the extrusions cut to the exacting lengths required as well as the high tolerances placed on the edge-to-edge dimensions. The difficulty was in spacing each extrusion apart as per specification since there were no predefined placement markings on the extrusions themselves. It was found that the easiest solution was to measure and mark off lengths of string that where of the specified spacing distances. Twine was used as it did not stretch when taut. The lengths of string where used to mark the centre-to-centre distances required between extrusions.

Figure 4-8 shows the pillow block bearings mounted to the cross beam, steel bracket used to attach the backing frame to the cross-beam, and the pillow block bearings. The linear actuator (shown in Figure 4-8) mechanically couples the cross beam and the mirror backing frame.
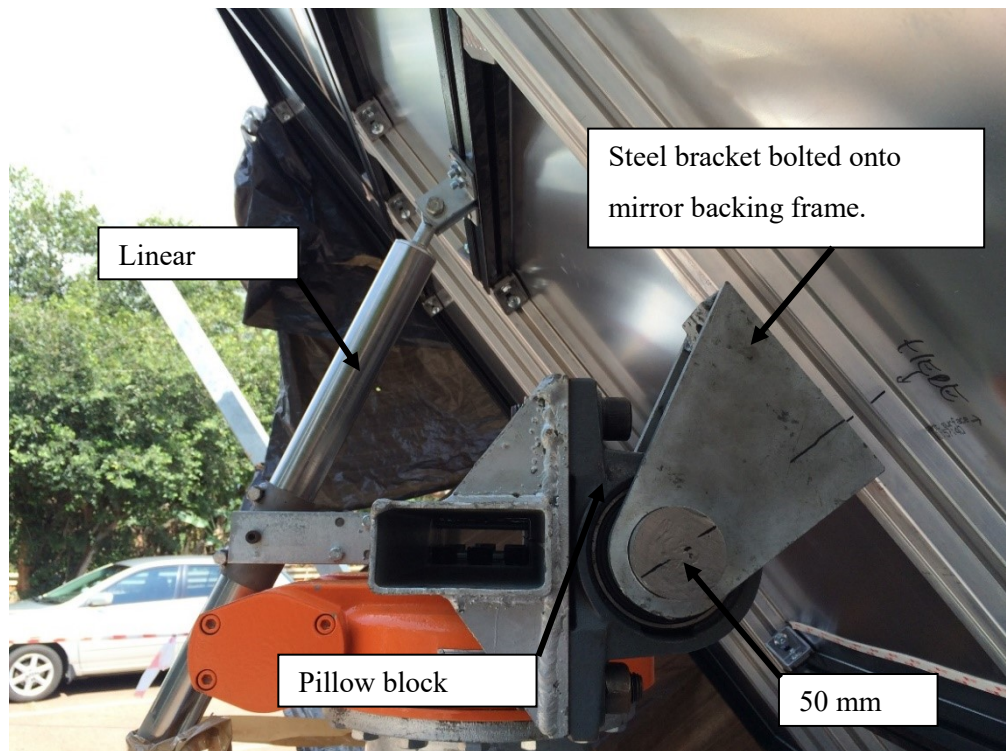
Figure 4-8:Cross beam coupled to the mirror backing frame.

4.5 Mirror attachment

Attaching the mirror modules to the backing frame posed several challenges. The mirror modules were attached parallel to the backing frame so as to avoid any canting errors, that could cause the reflected rays to divert from the ideal angle of reflection. Smaller heliostats, such as one developed at Stellenbosch University's Solar Thermal Energy Research Group (STERG) (shown in Figure 4-9) , utilise steel stand-offs to attach a 1830 mm x 1220 mm (2.2 m^2) glass facet to a backing frame fabricated using square steel tubes. However, for a 9 m^2 heliostat such as the one described in this study, the aluminium mirror must be adequately supported to mitigate macro-surface warpage and sagging over this larger surface area, which would also cause a decrease in optical accuracy. Another reason for not using rigid steel stand-offs was that aluminium mirror facets undergo thermal expansion due to direct solar irradiance. A compliant attachment method would allow for thermal expansion.

Figure 4-9: STERG's 1830 mm x 1220 mm prototype heliostat.

A solution to the above-mentioned challenges was to utilise the flatness of the aluminium extrusions and attach the mirror modules directly to the extrusions using an industrial strength two-way tape. The tape used was the VHB™ 4959 double sided foam tape manufactured by 3M™ (See appendix A for datasheet). The 4959 is of a foam sandwich construction with a thickness of 3 mm and a low modulus of elasticity, which allows for the expansion and contraction of the mirror modules. Figure 4-10 shows a schematic of the attachment method used.
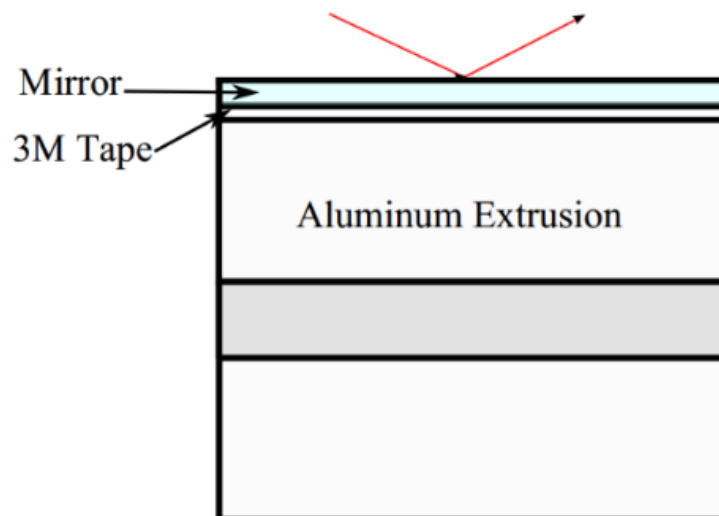
Figure 4-10: Schematic of mirror attachment method.

The mirror backing frame was moved onto site once it was assembled. The tape was then applied to the aluminium extrusions with a roller to ensure even adhesion to the surface of the backing frame. Figure 4-11 shows the tape adhered to the extrusions as well as one of the mirror modules attached. The mirror modules where cut into rectangular sections such that when laid coplanar to one another, form the required 3 m x 3 m square reflective area. To coincide with the cut rectangular mirror sections, the mirror backing frame was sized appropriately such that the outer faces of the aluminium extrusions serve as reference points for the edges of the mirror sections. This allowed the mirror sections to be correctly aligned with the backing frame by mating the edges of the facets flush with the outer surface of the outer most backing frame extrusion surfaces. Flushness was achieved by using a steel machinists set square.

Ensuring flatness of the reflecting surface was a key factor to consider whilst assembling the mirror assembly. Achieving surface flatness was aided by using the flat surface of the aluminium extrusions as well as their coplanarity relative to one another. The difficulty came in when ensuring that the edges of the mirror facets mated flush with one another. A set square was used with great care to ensure that the facet edges were as flush with one another as possible. However, it was important to ensure that if there were any significant alignment errors then they should occur at the edges of the reflective area as compared to the central portions of the reflective area (such as gaps) which would allow for a good quality image to be reflected onto the concentrator aperture.
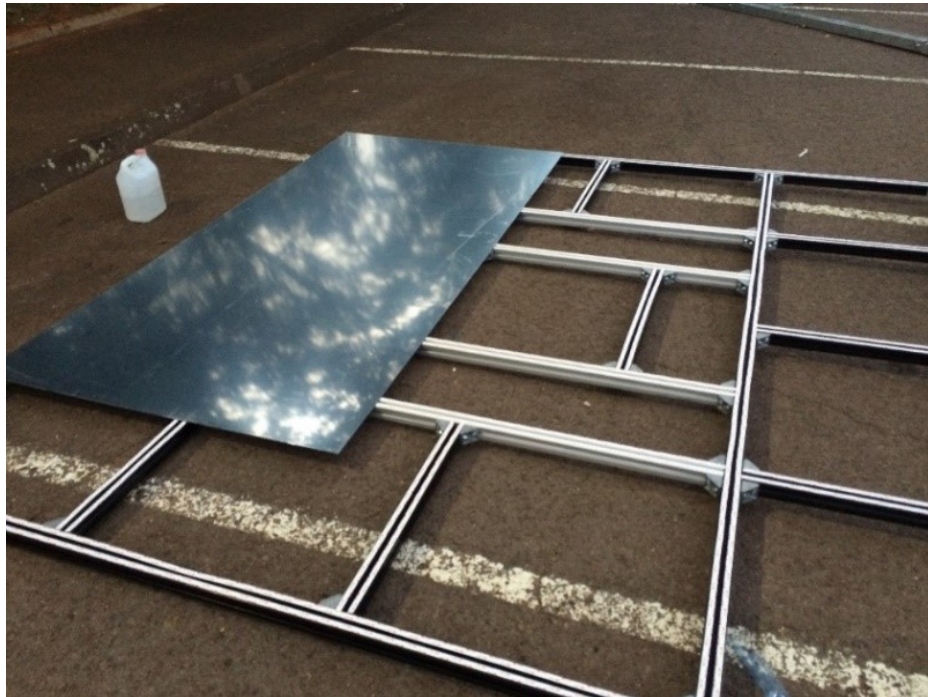
Figure 4-11: Mirror modules being attached to the mirror backing frame with double sided foam tape.

4.6 Final assembly

Final assembly of the heliostat was undertaken at a temporary site on the University campus. An open parking lot was utilised as it provided sufficient space with minimal shading, and was within close proximity of the Mechanical Engineering workshop. Figure 4-12 shows the process in which the heliostat was assembled at SERAFF's temporary installation site.
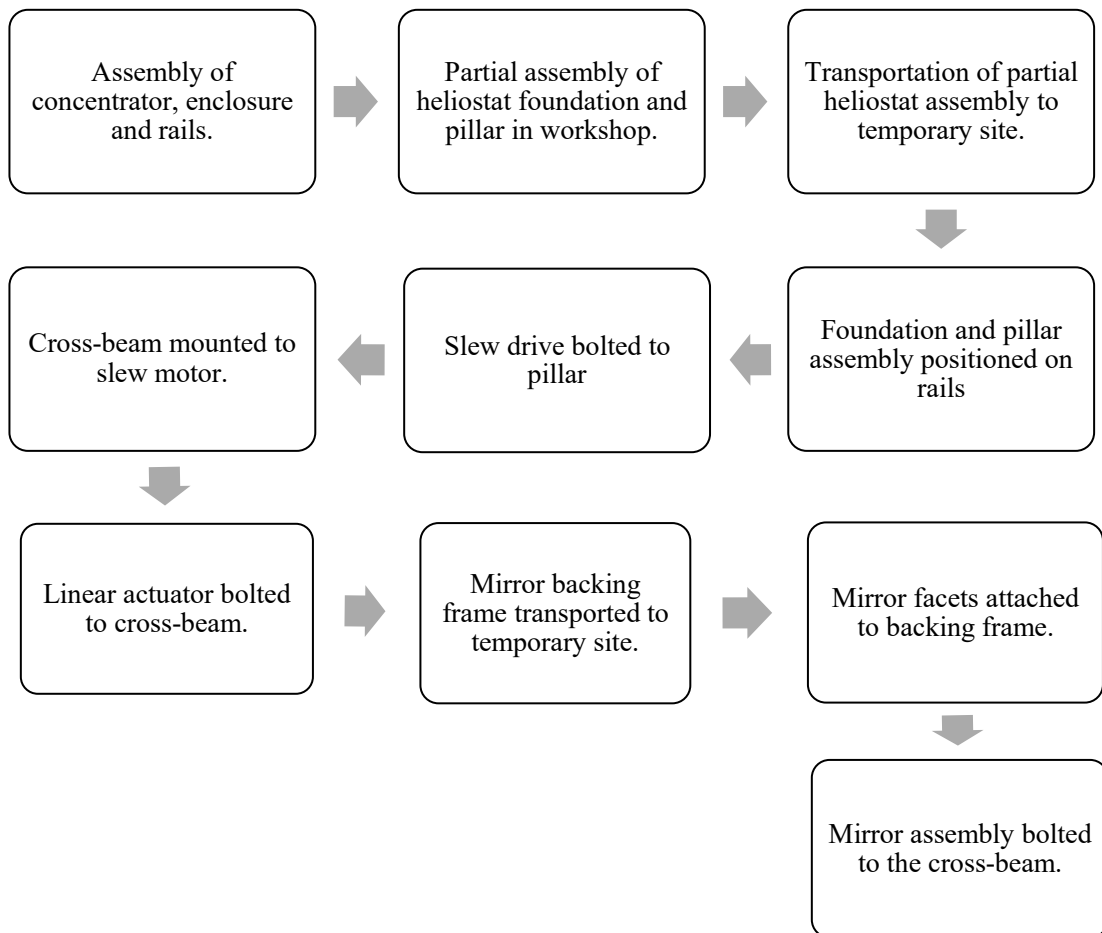
Figure 4-12: SERAFF's final assembly process diagram.

The assembly process began with SERAFF's primary concentrator and enclosure being positioned facing due south (or the back of the concentrator facing due north). The positioning and assembly of the primary concentrator, enclosure and rails are illustrated in Cassim et al. (2015).

The heliostat foundation and pillar assembly was made simpler using a gantry crane to hoist and position the pillar relative to the foundation. The gantry crane was not mobile thus the partial heliostat assembly was completed at the engineering workshop. The partial assembly was hoisted

onto the bin of a pick-up truck and transported to the temporary installation site. The foundation and pillar assembly was manually removed off the pick-up truck with the aid of 10 volunteers. It was then placed onto the rails which were installed prior to the arrival of the partial heliostat assembly on-site.

The heliostat backing frame was assembled in the workshop and transported to site without the mirror facets attached. It was decided that the mirror facets would be unpacked from their shipping crates and attached to the mirror backing frame on site to lower the risk of mirror damage during transportation from the workshop.

The heliostat assembly was complete when the mirror assembly had been bolted onto the cross-beam. The plastic protective layers where kept on the heliostat until required for use to protect the mirror surface from dust and other wind debris.

Figures 4-13 to 4-16 show the final assembled heliostat as well the rest of SERAFF's structural and optical components.

Figure 4-13: Front view of Heliostat in stow position.

Figure 4-14: Rear and front view of heliostat position on the rails.

Figure 4-15: Heliostat position in relation to the parabolic concentrator and housing structure.

Figure 4-16: Heliostat being brought into its stow position within housing structure.

4.7 Heliostat fabrication cost

One of the objectives of this study was to fabricate a cost-effective heliostat. A budget of approximately R85,000 was set aside at the start of the project to fund the fabrication of the heliostat. The total cost to realise the heliostat was R91,655 which meant that the budget was exceeded by R6,655. However, the actual cost of fabrication (which includes cost of materials and components) was R70,353.

The difference of R21,302 was due to the high import taxes paid on the specialised heliostat slewing drive motor (import from China) and the polished aluminium facets (import from Slovenia). Import tax paid on the slewing drive motor accounted for 50% of the total cost for the azimuthal drive. Similarly, import tax paid on the aluminium mirror facets accounted for 27% of the total cost of the mirrors. Together, import taxes paid on both these components accounted for 23.2% of the total cost of realising the heliostat.

The aluminium mirror facets could not be sourced locally because of their specialised nature and the absence of local suppliers (or manufacturers).

4.8 Basic assessment of the heliostat assembly

The heliostat assembly was assessed, upon completion of the assembly of SERAFF, with respect to its own structural integrity and functionality as well as how it fit within the solar furnace facility. These assessments were qualitative.

Starting at the foundation of the heliostat, it was important that there was an absence azimuthal/elevation axis tilt relative to the ground. There was little to no observed tilt in either axis as the steel rollers allowed for no lateral or longitudinal play since four sturdy and accurate points of contact were ensured with the rails. Testing of the heliostat rail system showed that the heliostat could be moved in and out of position with relative ease and efficacy.

The slew drive and linear actuator both actuated their relevant axes smoothly and without any noticeable strain on the motors. Apart from monitoring the actuation visually, an electronic multi-meter was used to monitor the current drawn by the actuators under load. Both the slew drive and the linear actuator drew currents well within their rated specifications.

The mirror assembly did however show some degree of flexion along the corner-to-corner (or diagonal) axes of symmetry. This was understood to be an accumulation of small rotational displacements allowed between the cast aluminium brackets and the aluminium extrusions. At the time of assembly completion, it was decided to assess the effects this would have in the total performance of SERAFF in future studies, which may, result in additional stiffening members being added to the heliostat backing frame.

The total virtual mass of the heliostat was 304 kg. This was calculated using the volumes of each component attained from the three-dimensional CAD model and the relevant mass densities of the materials used. Without physically measuring the mass the heliostat on a scale, the real mass of the heliostat should be very close to the virtual mass of 304 kg as there were no subtraction or addition of material during the fabrication process that would significantly increase the mass of the heliostat assembly.

SERAF was run upon completion of its assembly. The basic test was to qualitatively observe the system at work. Figure 4-17 shows the focal spot of the primary concentrator visible whilst turning a coarse spray of water into steam. Figure 4-18 shows qualitative test after completion of the assembly process in order to gauge the correct alignment of the optical components immediately after installation.

Figure 4-17: Focal spot made visible using a coarse spray of water.

Figure 4-18: Wooden plank being combusted when placed within SERAFF's focal spot.

4.9 Conclusion

The fabrication process of the three core structural components (pillar, foundation and mirror backing frame) and their respective sub-assemblies were illustrated in this chapter. The fabrication processes used will affect the tracking and optical accuracy of the heliostat, thus careful consideration was needed in to this phase of the project. Remaining within the specified tolerances and fits with regards to the pillar and I-beam assemblies was one of the most significant aspects of the build as these components will directly influence the azimuthal/elevation tilt error.

Upon assessment of the final heliostat assembly, it was observed that there was no significant tilt in either of the axes relative to the ground normal.

The azimuthal and elevation actuators remained well within their rated specifications under operational load. To confirm this, a multi-meter was used to measure the current drawn by the actuators during operation.

A foam sandwiched double-sided adhesive was used as a compliant method for attaching the aluminium mirror facets to the mirror backing frame. This compliant attachment method allows for thermal expansion of the mirror facets relative to the backing frame.

Some degree of flexion was observed along the corner-to-corner axes of symmetry. Future studies and testing of the heliostat during SERAFF's operation must be conducted to ascertain whether this flexion severely decreases its thermal performance. These studies may lead to additional stiffening members to be added to the mirror backing frame.

The total cost of fabrication was R91,655 and overshot the budget of R85,000 by R6,655. However, this was due to high import taxes paid on the slewing drive actuator and polished aluminium mirror facets. The actual cost of materials and components was R70,353 excluding the import taxes. SERAFF, after the completion of fabrication and assembly is the first research-based solar furnace facility in South Africa.

Chapter 5. Control System

5.1 Calculating the required heliostat orientation

The function of a heliostat is not to aim directly at the sun, as is the case with direct tracking solar collectors, but rather to reflect light towards a stationary target. This is achieved by means of the law reflection, illustrated in Figure 5-1, which states that the angle at which a light ray is reflected must be equal to the angle of incidence of that particular light ray, assuming ideal reflection.

.
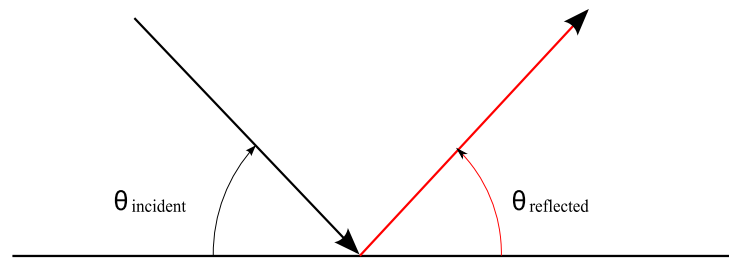
Figure 5-1: Law of Reflection.

For a solar furnace heliostat to reflect an image of the solar disc at a stationary target, three primary vectors must be determined; the solar vector ($\vec{S}$), target vector ($\vec{R}$) and the heliostat normal vector ($\vec{H}$). The target vector is a constant vector describing the direction in which the target (in this case, the concentrator) is positioned relative to the heliostat in three-dimensional space. The heliostat normal vector is a function of the changing solar vector at any point in time. A global coordinate system is needed to describe the solar vector, as shown in Chapter 3, Figure 3-3.

The solar vector ($\vec{S}$) can be calculated once the solar azimuth (A) and elevation angles (α) are known:

$$\vec{S} = \begin{bmatrix} X_s \\ Y_s \\ Z_s \end{bmatrix} = \begin{bmatrix} |\vec{S}|.\cos(\alpha).\cos(A) \\ -|\vec{S}|.\sin(A).\cos(\alpha) \\ |\vec{S}|.\sin(\alpha) \end{bmatrix} \tag{26}$$

It must be noted that the solar azimuth angle for the given coordinate system is subject to following conditions: if $0°<A<90°$ then $A=A$, and if $A>270°$ then $A=A$-360°. The solar unit vector ($\hat{S}$) is simply the solar vector divided by its magnitude.

The target vector ($\hat{R}$) is simply a unit vector from the centroid of the heliostat (origin) to the centroid of the concentrator. This unit vector is given by:

$$\hat{R} = \overrightarrow{HT} = [1 \quad 0 \quad 0] \tag{27}$$

The heliostat normal unit vector ($\hat{H}$), as per the law of reflection, will be the bisecting vector between the solar unit vector and target unit vector as shown in Figure 5-2.
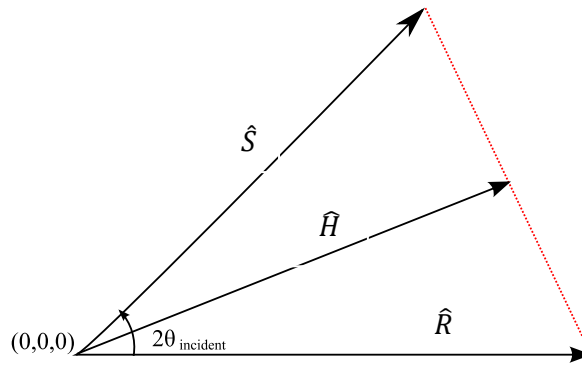
Figure 5-2: Heliostat normal vector diagram

The expression for the heliostat normal unit vector is then:

$$\hat{H} = [X_h \quad Y_h \quad Z_h] = \frac{\hat{S} + \hat{R}}{2.|\overrightarrow{H}|} = \left[\frac{X_s + 1}{2.|\vec{S}|} \quad \frac{Y_s}{2.|\vec{S}|} \quad \frac{Z_s}{2.|\vec{S}|} \right] \tag{28}$$

A more useful representation of the heliostat normal vector is given when transformed into polar coordinates. The required heliostat azimuth (A_h) and elevation ($\propto_h$) angles are finally:

$$A_h = -\tan^{-1}(\frac{Y_h}{X_h}) \tag{29}$$

$$\propto_h = \sin^{-1}(Z_h) \tag{30}$$

Equations 26 – 30 enable the implementation of a control system that utilises the above expressions to orientate the heliostat to its required position.

5.2 Heliostat control hardware

Initially, open-source Arduino hardware was to be used to control the heliostat because it offered the most cost-effective solution. However, during the initial integration between the Arduino microcontroller, quadrature encoders and solar position algorithm it was found that the platform was not able to adequately perform both, real-time tracking and motor control simultaneously. This meant that an alternative software language and hardware was needed. The graphical programming software LabVIEW™ was chosen for this purpose, since it allows for parallel processing which enables the controlling hardware to execute tracking and control algorithms in real-time, robustly and with high speed.

The LabVIEW™ software is developed by National Instruments™ and thus optimised for National Instruments™ hardware. This equipment is, however, expensive. The cost of the hardware initially rendered its use unfeasible, however, various items of National Instruments™ hardware were made available to the project on loan. This allowed for the testing and operation of the heliostat and its control software.

The heliostat operates under a closed-loop control scheme. This means that a controller constantly monitors some form of feedback associated with the heliostat's orientation. In this work, the required feedback took the form of a digital reading from two quadrature encoders, installed within the azimuth and elevation actuators. Figure 5-3 shows the closed loop control scheme implemented to execute full control of the heliostat's motion.
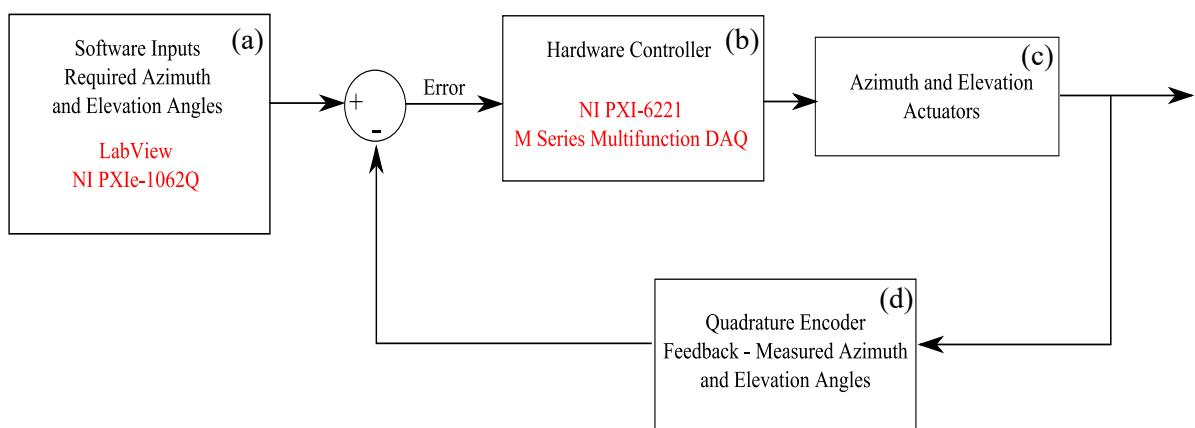
Figure 5-3: Closed-loop feedback schematic.

The heliostat azimuth and elevation actuator control inputs are generated through softwae installed on a dedicated National Instruments™ computer with embedded controllers (NI PXIe-1062Q), as shown in Figure 5-4 . An error signal is generated by comparing the input signal from

software with the feedback signal from the qudrature encoders. The error signal is sent to the hardware controller (NI PXI-6221), also indicated in Figure 5-4, embedded in the NI PXIe-1062Q. The azimuth and elevation actuators are then actuated until the error signal is zero.

NI PXI-6221 M
Series Multifunction
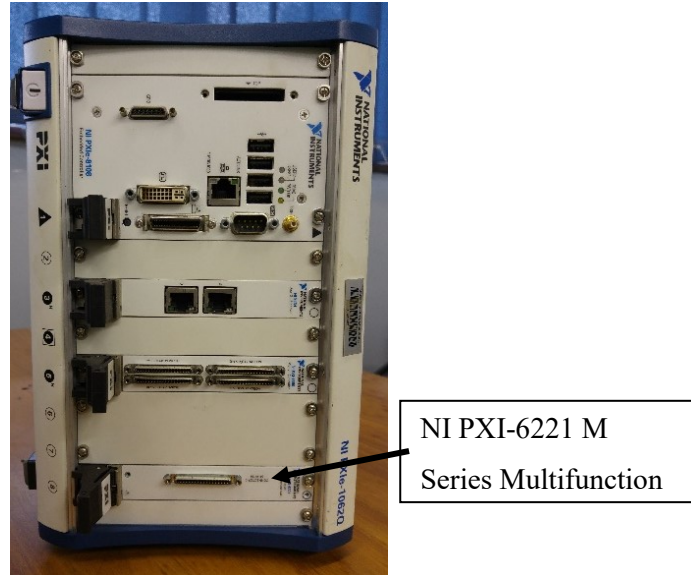
Figure 5-4: NI PXIe-1062Q computer with embedded control modules.

The interface between the hardware controller and the actuators must allow for polarity switching, power distribution and surge protection. For this application, an off-the-shelf motor controller was used. The controller chosen was the Olimex™ BB-VNH3SP30, shown in Figure 5-5. This motor controller is based on a simple H-bridge architecture with additional features such as pulse-width modulation and current sensing. This component is also important because it isolates the controller hardware from high voltages and currents thus protecting them from any electrical shorts or surges. The motor controller is rated to a maximum of 36 V and 30 A, which is well above the actuator ratings of 24 V and 4 A, respectively, making it a suitable choice for this application.
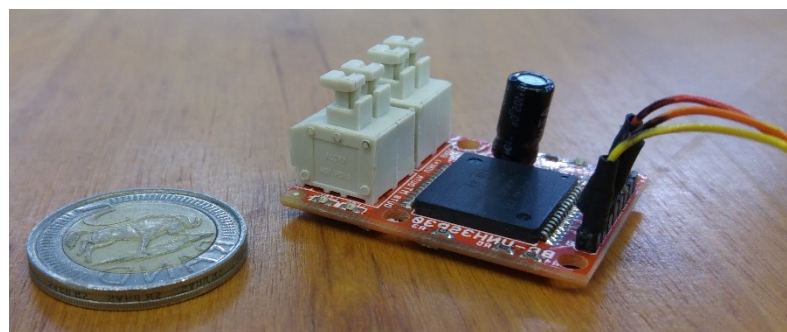
Figure 5-5: Motor controller used to interface hardware controller and actuators

5.3 Heliostat control software

A LabVIEW™ software application was written once the hardware requirements of the control system were met. It was important to understand exactly how the hardware architecture being utilised could be optimised to use the computing resources available efficiently. The software application was designed and programmed to serve as both an executor of the solar tracking and heliostat orientation algorithms, as well as providing a graphical user interface (GUI). This would pose a significant challenge using traditional line-based coding architecture, however, the graphical programming architecture utilised in LabVIEW™ greatly simplifies the task. The implementation of solar positioning algorithms into LabVIEW™ can be found in many open-source archives.

Code execution

The sequence of code execution is pivotal in a graphical programming environment. The most significant advantage of graphical programming is the ability to execute multiple batches of code simultaneously; this is called parallel processing. Thus, it is possible to calculate the solar position vector and required heliostat orientation whilst sending motor commands and monitoring feedback from quadrature encoders.

The sequence of code execution was mapped out using traditional flow diagrams to make the complex task of solar tracking and motor control simpler. It is easier to understand the flow of control if the azimuth and elevation tracking are illustrated using the same flow diagram. This shows the fundamental logic that the control software was built upon. Figure 5-6 shows the execution of the code which governs the operation of the heliostat.
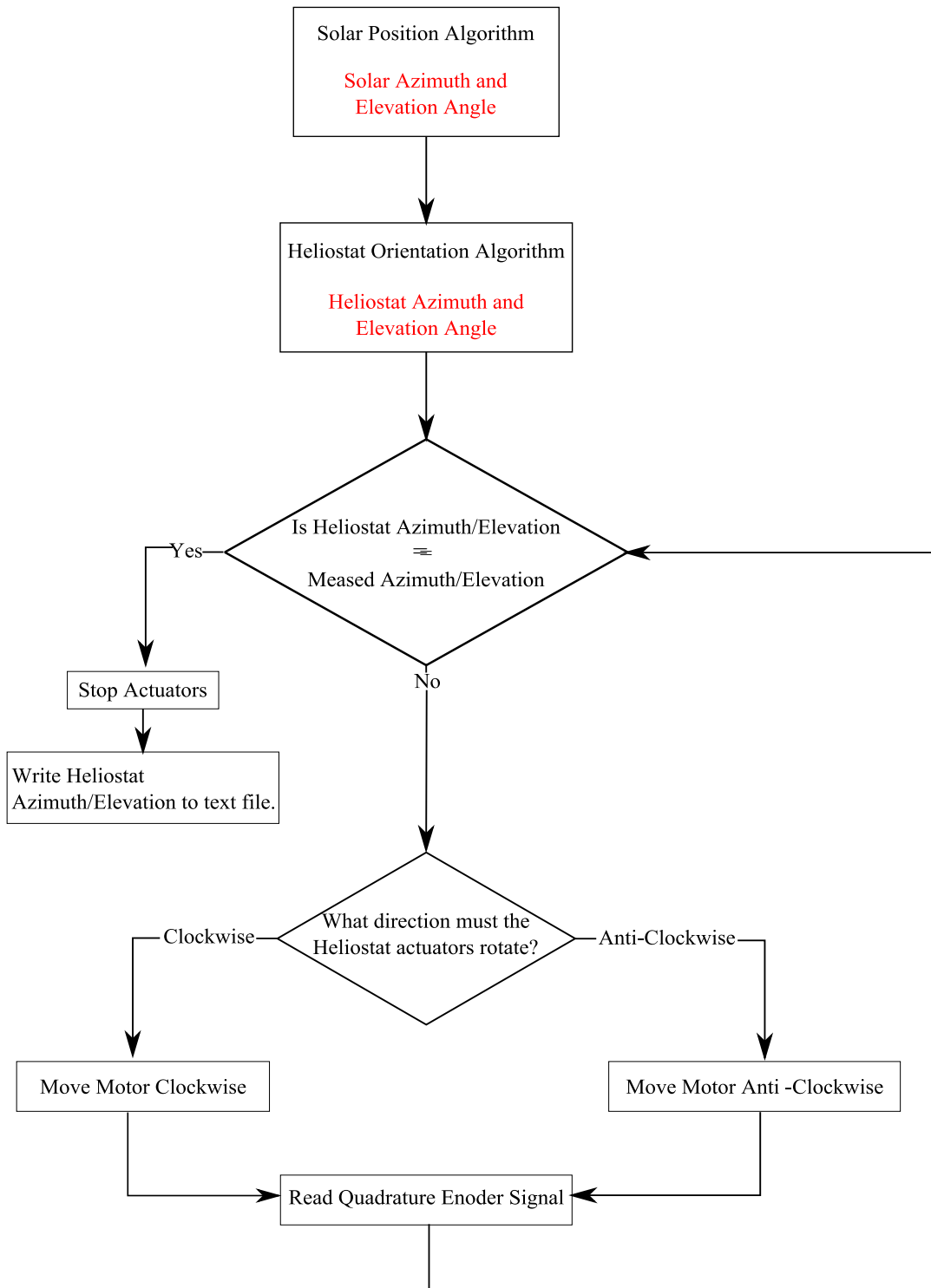
Figure 5-6: Code execution diagram showing fundamental logic in controlling the heliostat's position.

With reference to Figure 5-6, it can be seen that all control commands initiate from the solar position algorithm, which is used for calculating the solar vector. The solar position vector is calculated at a rate of 1 Hz and utilises the radian as its primary calculative unit but is displayed to the user in degrees as this is a more of an intuitive form of angular displacement/position.

Figure 5-7 shows the graphical code used to calculate the solar vector as well as displaying a three-dimensional view of the sun's position relative to the heliostat to the user.
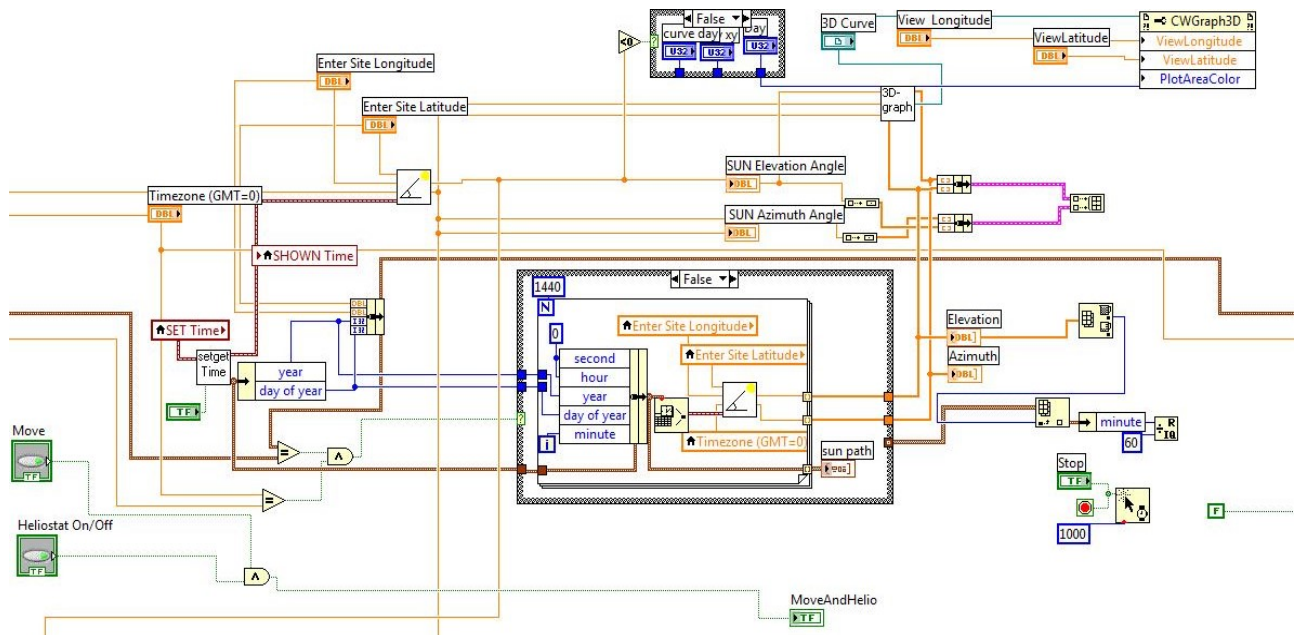
Figure 5-7: Graphical code snippet of the solar position algorithms and 3D solar position viewport.

For a solar furnace, the heliostat does not aim directly at the sun like a photovoltaic tracker would. The heliostat aiming vector is dictated by the algorithm detailed in Section 5.1 of this chapter. The heliostat position algorithm was implemented using graphical code, shown in Figure 5-8, similar to that used for the solar position algorithm.
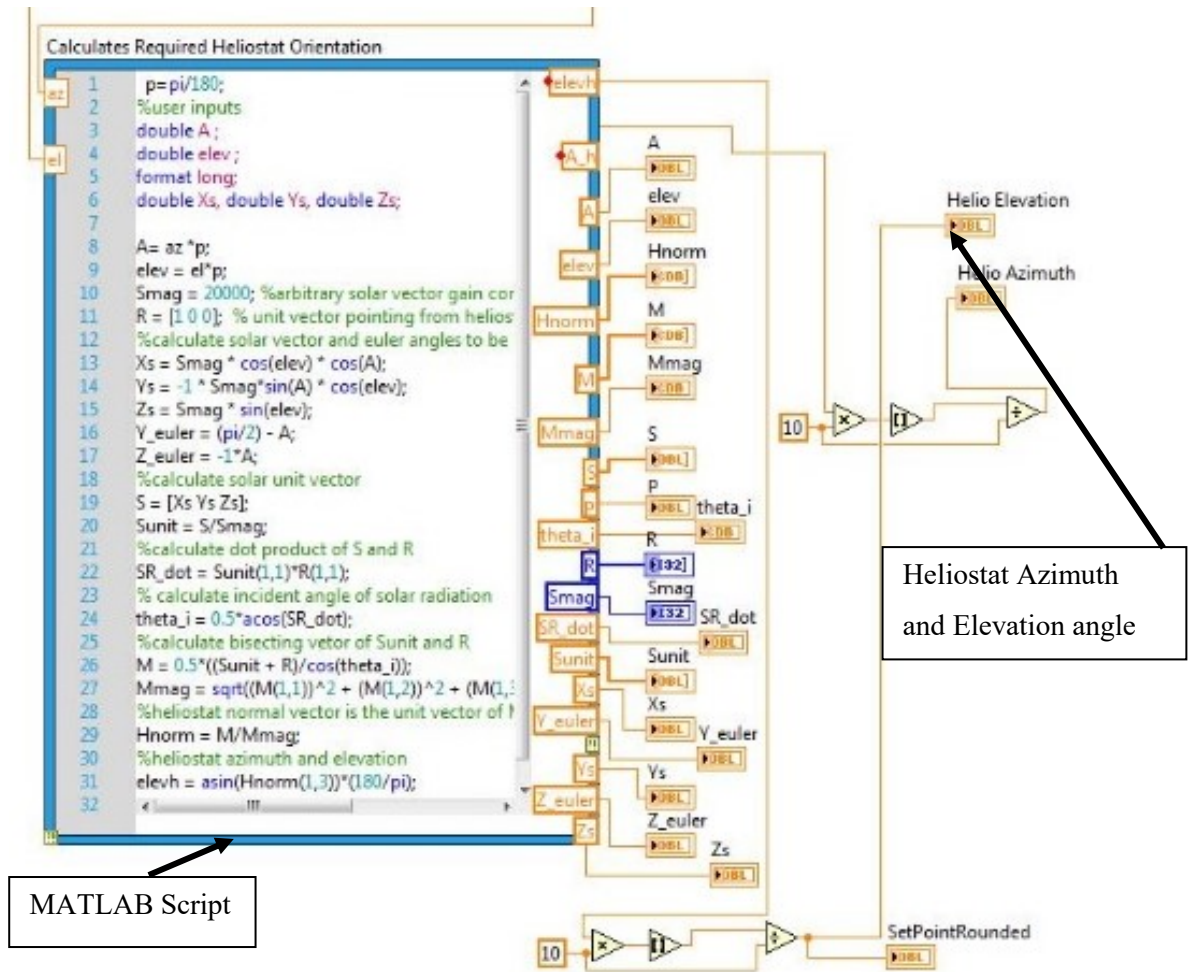
Figure 5-8: Graphical code snippet of the heliostat orientation algorithm.

Analysing Figure 5-8, the implementation of the heliostat position algorithm differs slightly from the implementation of the solar position algorithm. Here, a more conventional line-based code was used but it was implemented using a graphical code block that allows MATLAB™ script language to be utilised. The use of MATLAB™ scripting language largely reduced computational expense, as compared to previous graphically-coded versions of the heliostat position algorithm.

Moving down the code execution diagram, the next logic step was to determine whether the heliostat is in its required position. If not, the control software must decide whether to move the actuators clockwise or anticlockwise while simultaneously monitoring the quadrature encoder feedback. This control logic was easily implemented using true/false case-structures and comparators within LabVIEW™, as illustrated in Figure 5-9, which is an example of the azimuth position control of the heliostat.
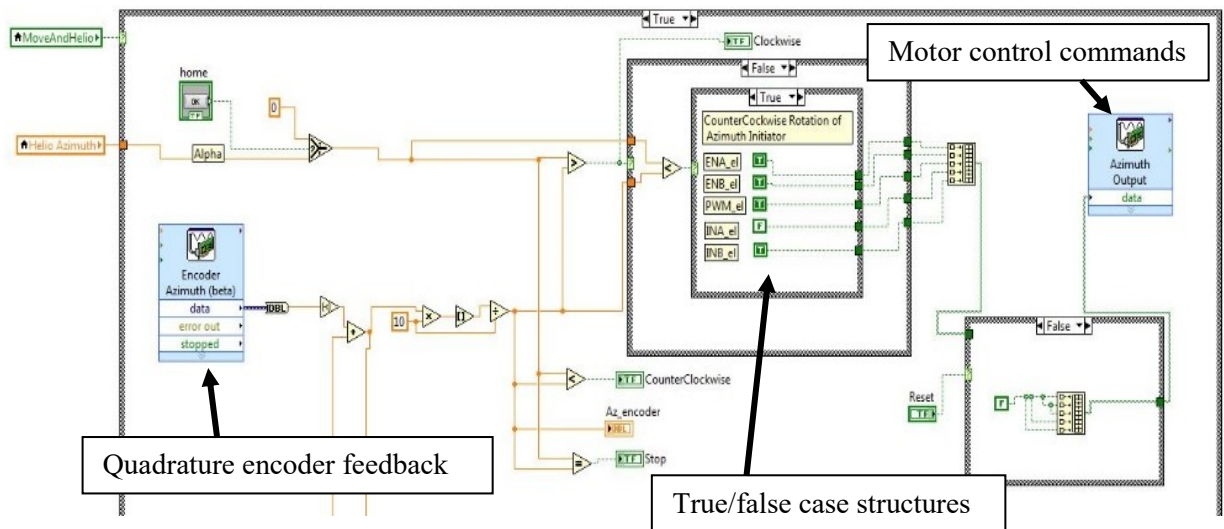
Figure 5-9: Logic control and motor command code snippets.

Each of the graphical code snippets shown provide very particular solutions to the challenges of real-time solar tracking. When these components are executed in parallel, the heliostat position can be fully controlled to track the solar vector.

Graphical User Interface

The graphical user interface allows the user to operate the heliostat easily and intuitively. The GUI should not overwhelm the user with numerous parameters and settings, thus all input parameters are automatically generated by the source code. The user need only input the location, time and date. These parameters are easily input using graphical components such as calendar displays and drop-down menus. Figure 5-10 shows the front GUI which houses all the controls necessary to operate the heliostat.

To prevent accidental or unplanned motion of the heliostat, a safe start up sequence was required. The "Heliostat ON/OFF" button must be pressed to initiate the powering on sequence of the heliostat controllers and actuators, this is done automatically once the button is pressed. The heliostat will not move unless the "Move" button is pressed.
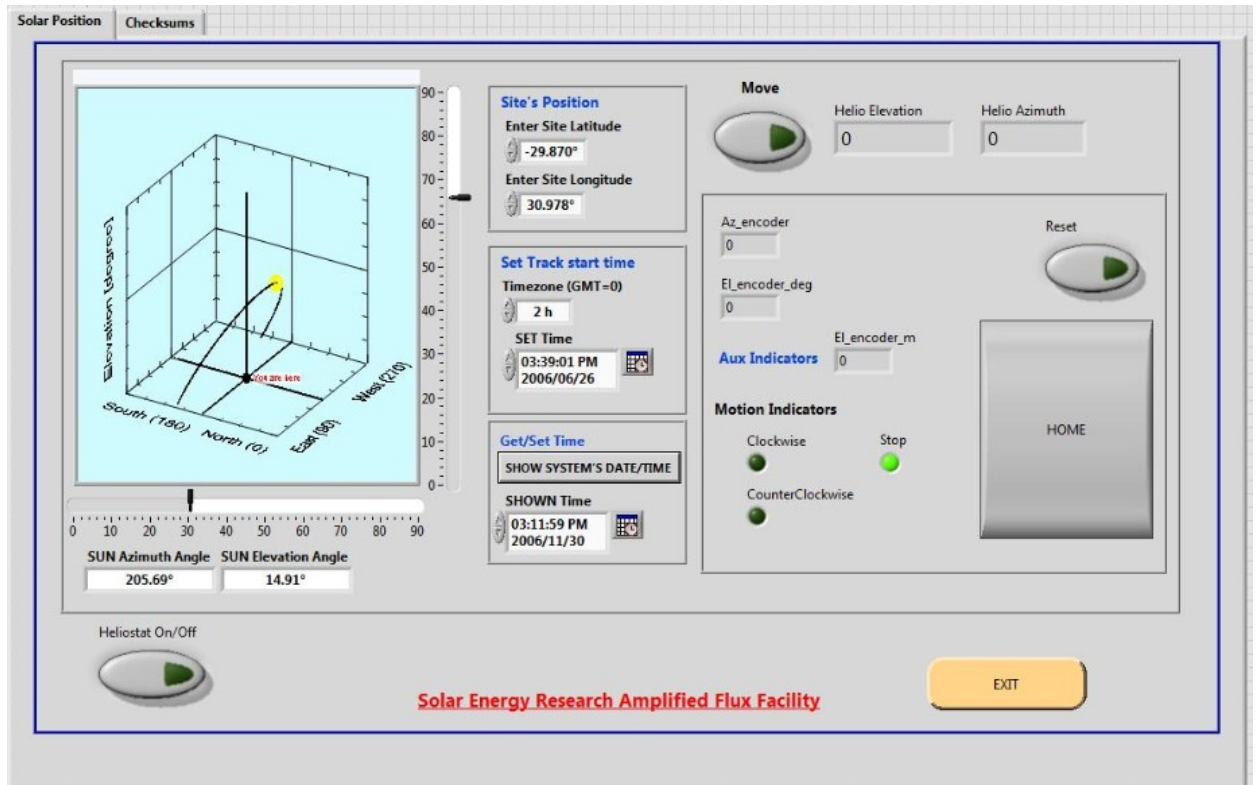
Figure 5-10: Heliostat control graphical user interface.

A 3D viewport is placed in the user interface to allow the user to easily visualise the correct position of the sun and its trajectory over the period in which the experiment is being run. The 3D viewport can be rotated freely by using the scroll bars on the peripheral of the viewport window.

The solar azimuth and elevation angles are calculated and displayed to the user once every second, and are automatically calculated using the computer system time, which avoids erroneous time inputs by the user. Along with the solar position, the required heliostat azimuth and elevation angles are displayed. Also, the current quadrature encoder readings are displayed to allow the user to monitor the heliostats motion. A graphical illustration of these movements could be implemented to make monitoring the heliostat more intuitive, although this was beyond the scope of the project.

Motion indicator lights represent an additional important monitoring aid as they allow the user to know which direction the heliostat is moving in, at any given point in time. The "Home" button allows the user to send the heliostat back to its home position. It is interesting to note that this feature is hardware independent, meaning it does not rely on physical limit switches to dictate the heliostat home position. Rather, the homing of the heliostat is determined by software, where all previous positions of the heliostat are stored in a text file and accessed when the home button is

pressed, so regardless of the position of the heliostat it will always go precisely to a home position such that the last known position of the heliostat tends to zero. This feature allows the user to set multiple home positions without the need to reconfigure any physical hardware.

5.4 Conclusion

The software and hardware used to control the heliostat and give it the ability to track the solar vector have been highlighted. The use of a graphical programming language allowed the development of a GUI and control algorithms to be packaged in one executable file.

The graphical user interface developed could be improved in terms of appearance and the overall user experience. However, the current version of the control application was found to be more than suitable for successful solar tracking and control of the heliostat during solar furnace operation.

Future software inclusions will allow the user to monitor system performance and other important metrics of SERAFF in its entirety. These would likely include the incorporation of a data acquisition system and displays of thermal flux at the target of the solar furnace, for example.

Chapter 6. Conclusion

South Africa has an outstanding solar resource and currently has three operational concentrating solar power plants, namely, Bokpoort (parabolic trough), KaXu Solar One (parabolic trough) and Khi Solar One (power tower). These three large-scale CSP plants have a combined generating capacity of 200 MW. A further four plants are in development and under construction, taking South Africa's total generating capacity to an estimated 600 MW. Solar furnaces can play a vital role in the research and development of technologies utilised in the CSP industry, as well as in other applications as highlighted in Chapter 1.

SERAFF will primarily support the research into CSP receiver technologies, advanced materials and solar process heating application. A 5 kW thermal power output and a peak thermal flux of 3 MW/m^2 were specified to enable such research at the University of KwaZulu-Natal. The object of this research was to design and fabricate a heliostat that would allow SERAFF to achieve its thermal specifications.

The first phase in the implemented methodology was the characterisation of Durban's solar resource. A novel statistical algorithm was proposed in Chapter 2. This algorithm utilised ground-based radiometric measurements to produce a three-dimensional map of the historical trends in DNI for Durban. Similarly, the algorithm was applied to historical data captured in Stellenbosch as a comparative exercise. The statistical model proposed in this study was compared to predictive radiometric models found in literature. A statistical analysis showed that the ASHRAE and tuned Fu Rich models performed best when approximating clear-sky DNI on a daily per-minute basis, estimating values within ±5% for Stellenbosch and ±10% for Durban. However, the same models did not perform as well in predicting seasonal variations of clear-sky DNI, underestimating values by as much as 25% in winter. However, with the aid of the proposed algorithm, it can be concluded that the above models are reasonable for use in preliminary solar concentrating equipment design case studies at sites where there is an absence of ground-based measurement.

An optical design approach was used to size the primary concentrator of the furnace and thus appropriately sizing the required heliostat reflective area. The temporal DNI topograph was used in establishing DNI inputs into the ray tracing simulation model to assess the thermal performance of various sized parabolic concentrators. A geometrical model was used to calculate the concentrator aperture diameter required to achieve SERAFF's thermal power output. The model's validity was proven by using it to estimate the thermal power output for different solar furnaces around the world. The effective concentrator aperture areas and other optical parameters for these

solar furnaces were input into the model. It was shown that the model predicted the thermal power outputs of these solar furnaces within 12% of the values stated in literature. Thus, it was reasonable to conclude that the model was suitable in estimating the required aperture area to achieve the 5 kW thermal output requirement. It was concluded that SERAFF would require a parabolic concentrator with a diameter of 3 m.

A ray tracing simulation was also used to evaluate SERAFF's sensitivity to slope error as a function of heliostat size. It was found that the larger the heliostat reflective surface area, the more sensitive the thermal performance of SERAFF was to slope error. With this finding being taken into consideration, as well as practical and financial constraints placed on the project, it was decided that a 3 m x 3 m heliostat was the most suitable. An illumination study was carried out to further validate the suitability of the chosen heliostat size. It was shown that a 3 m x 3 m heliostat would satisfactorily illuminate the 3 m diameter concentrator aperture throughout SERAFF's anticipated operational windows during clear-sky days.

Heliostat concepts were formulated using both conventional and unconventional design elements from heliostats used around the world in CSP and solar furnace applications. A finite element analysis was used to determine the best performing concept with regards to deflection of the pillar under operational wind loads. It was determined that a traditional T-shaped design (steel tube pillar and cross-beam form the 'T' shape) and a mirror backing frame constructed from aluminium extrusions would provide the most suitable design. A wind load model was used to calculate the forces the heliostat would be subjected to under an operational wind speed of 20 km/hr as well as during the worst-case wind speed for Durban of 100 km/hr for a survivability analysis. A one-dimensional FEA was undertaken to assess the deflection of the aluminium backing frame under the operational wind speed. The FEA results showed a maximum deflection of less than a millimetre. However, the mirror assembly did show some degree of flexion along the corner-to-corner (or diagonal) axes of symmetry when preliminary testing of SERAFF commenced. This was understood to be an accumulation of small rotational displacements allowed between the cast aluminium brackets and the aluminium extrusions. At the time of assembly completion, it was decided to assess the effects this would have in the total performance of SERAFF in future studies, which may, result in additional stiffening members being added to the heliostat backing frame.

Fabrication and assembly of the heliostat took place at a temporary installation site which was in closer proximity to the engineering workshop as well as offered an easier access route than the final installation site atop the municipality reservoir.

The budget of R85,000 was exceeded due to the very high cost of import taxes paid on the slewing drive motor and aluminium mirror facets. The total cost of realising the heliostat, inclusive of import tax, was R91,655 whereas the actual cost of the materials and all components was R70,353. In future, as South Africa's involvement in CSP technology research and development increases, there may be sufficient motivation for establishing local suppliers for specialised solar actuators and reflectors, thus mitigating the cost of importing such components.

Upon the completion of the fabrication and assembly of the heliostat and SERAFF, preliminary operations were conducted to assess the final assembly of the heliostat. Excitingly, there were promising observations that were made. The heliostat cast an image to fully illuminate the parabolic dish and there was a significant amount of thermal flux at the focal plane of the heliostat.

The scope of this study was to design and fabricate the heliostat. This was successfully achieved but future testing into the optical efficiency of the heliostat and tracking accuracy is required to give a quantitative measure to the heliostat performance.

REFERENCES

ASHRAE, "Handbook of Fundamentals - American Society of Heating, Refrigeration and Air-Conditioning", (1972).

Aziz, A. and Gamil, M., "Estimation of Hourly Clear-sky Solar Radiation for PDR Yemen", *Solar & Wind Technology*, 7(2), pp.255-260, (1990).

Bader, R., Pedretti, A., Barbato, M. and Steinfeld, A., "An Air-based Corrugated Cavity-Receiver for Solar Parabolic Trough Concentrators", *Applied Energy*, 138, pp.337-345, (2015).

Bird, R. E. and Hulstrom, R. L., "A Simplified Clear Sky Model for Direct and Diffuse Insolation on Horizontal Surfaces", Solar Energy Research Institution, (1981).

Brender, W., "Final Technical Progress Report: Development of Low-cost Suspension Heliostat", National Renewable Energy Laboratory, (2013).

Brooks, M. J., "Performance of a Parabolic Trough Solar Collector", (MScEng), Stellenbosch University, (2005).

BS EN 12975-1, [Standard], *Thermal solar systems and components. Solar collectors. General requirements.*, (2006).

Cassim, R. S., Deena, A. A. and Levine, G., "Solar Furnace Primary Concentrator", Final Year Project Report, Discipline of Mechanical Engineering, University of KwaZulu-Natal, (2015).

Chuncheng, Z., Hong, L. and Yi, R., "Experimental wind load model for heliostats", *Applied Energy*, 93, pp.444-448, (2012).

Coventry, J. and Pye, J., "Heliostat cost reduction - where to now?", *Energy Procedia*, 49, pp.60-70, (2014).

Davies, J. M. and Cotton, E. S., "Design of the Quartermaster Solar furnace", *The Journal of Solar Energy Science and Engineering*, 1(2-3), pp.17-22, (1957).

Fernandez-Reche, J., Canadas, I., Sanchez, M., Ballestrin, J., Yebra, L., Monterreal, R., Rodriquez, J., Garcia, G., Alonso, M. and Chenlo, F., "PSA Solar Furnace: A facility for testing PV cells under concentrated solar radiation", *Solar Energy Materials & Solar Cells*, 90, pp.2480-2488, (2006).

Fluri, T.P., "The Potential of Concentrating Solar Power in South Africa", *Energy Policy*, 37, pp. 5075 – 5080, (2009).

Fu, P. and Rich, P., "Design and Implementation of the Solar Analyst: an ArcView Extension for Modelling Solar Radiation at Landscape Scales", *In the Proceedings of the 19th Annual ESRI User Conference*, (1999).

Gueymard, C. A., "Temporal Variability in Direct and Global Irradiance at Various Time Scales as Affected by Aerosols", *Solar Energy*, 86(12), pp.3544-3553, (2012).

Hariram, A. V., "The use of CFD for Heliostat Wind Load Analysis", (MScEng), Stellenbosch University, (2015).

Haueter, P., Seitz, T. and Steinfeld, A., "A New High-Flux Solar Furnace for High-Temperature Thermochemical Research", *Journal of Solar Engineering*, 121, pp.77-80, (1999).

Hottel, H. C., "A Simple Model for Estimating the Transmittance of Direct Solar Radiation through Clear Atmospheres", *Solar Energy*, 18(2), pp.129-134, (1976).

Huang, W., Hu, P. and Chen, Z., "Performance Simulation of a Parabolic Trough Solar Collector", *Solar Energy*, 86(2), pp.746-755, (2012).

Johansson, T. B. and Burnham, L., Renewable Energy: Sources of Fuels and Electricity, Island Press, (1993).

Kumar, L., "Modelling Topographic Variation in Solar Radiation in a GIS Environment", *International Journal of Geographical Information Sciences*, 11(5), pp.475-497, (1997).

Kunene, K. R., Brooks, M. J., Roberts, L. W. and Zawilska, E., "Introducing GRADRAD: The Greater Durban Radiometric Network", *Renewable Energy*, 49, pp.259-262, (2013).

Larmuth, J., Malan, K. and Gauché, P., "Design and Cost Review of 2m² Heliostat prototypes", *Proceedings of SASEC 2014*, Port Elizabeth, South Africa, (2014)

Lingamgunta, C. and Veziroglu, T. N., "A Universal Relationship for Estimating Daily Clear Sky Insolation", *Energy Conversion and Management*, 45(15), pp.2313-2333, (2004).

MATLAB, "User Guide Release 2014b", The MathWorks, Inc., Natick, Massachusetts, United States, [online], Available at: http://www.mathworks.com/help/matlab.

Neumann, A. and Grouer, U., "Experimenting with Concentrated Sunlight using the DLR Solar Furnace", *Solar Energy*, 58(4-6), pp. 181-190, (1996).

NREL, "Concentrating Solar Power Projects in South Africa", [Online]. Available at: http://www.nrel.gov/csp/solarpaces/by_country_detail.cfm/country=ZA [accessed 20 November 2016].

Open Nature, Press Release 5-2, [online], Available at: http://www.tourisme-pyreneesorientales.com/Upload/Mediatheque/presse-gb/5-2-EnergieSolaireGB-Web.pdf. [accessed 20 July 2015]

Perumall, P. A., Brooks, M. J. and Pitot de la Beaujardiere, J. P. "An Introduction to the University of KwaZulu-Natal's Solar Energy Research Amplified Flux Facility - SERAFF". *13th International Energy Conversion Engineering Conference, AIAA Propulsion and Energy Forum,* Orlando, Florida, 27-29 July, (2015a).

Perumall, P. A., Brooks, M. J. and Pitot de la Beaujardiere, J. P., "A New Measurement-Based Algorithm for the Temporal Resolution of the Clear-Sky Solar Resource". *R & D Journal of the South African Institute of Mechanical Engineers,* 31, pp.27-34, (2015b).

Peterka, J. A. and Derickson, R. G., "Wind load design methods for ground based heliostats and parabolic dish collectors", SANDIA National Laboratories, (1992).

Pfahl, A., Randt, M., Holze, C. and Unterschutz, S., "Autonomous light-weight heliostat with rim drives", *Solar Energy*, 92, pp.230-240, (2013).

Punatar, M. K., "Solar Furnace Design", (MScEng), Department of Mechanical Engineering, Kansas State University, Manhattan, KA, (1967).

SABS, "SANS 10160-3: Basis of Structural Design and Actions for Buildings and Industrial Structures -Part 3: Wind Actions", [standard], (2011).

Salazar, G. A. and Raichijk, C., "Evaluation of Clear-sky Conditions in High Altitude Sites", *Renewable Energy*, 64, pp.197-202, (2014).

Samanes, J. and Garcia-Barberena, J., "A Model for the Transient Performance Simulation of Solar Cavity Receivers", *Solar Energy*, 110, pp.789-806, (2014).

SANDIA, "National Solar Thermal Test Facility (NSTTF)", [online], Available at: http://www.energy.sandia.gov, (2008).

SAURAN, South African Universities Radiometric Network, [online], Available at: http://www.sauran.net, (2014).

SolarPACES, "Catalog of Solar Heliostats- IEA Solar Power and Chemical Energy Systems Task III: Solar Technology and Applications", Technical Report, (2000a).

SolarPACES, "IEA-Solar Power and Chemical Energy Systems Task III: Solar Technology Applications", SANDIA National Laboratory, (2000b).

SPA,Solar Position Algorithm, [online], Available at: http://www.nrel.gov/midc/solpos/spa.html, (2014).

Spadavecchia, L., Williams, M., Bell, R., Stoy, P. C., Huntley, B. and van Wijk, T., "Topographic Controls on the Leaf Area Index and Plant Functional Type of a Tundra Ecosystem", *Journal of Ecology*, 96(6), pp.1238-1251, (2008).

Spencer, J. W., "Fourier Series Representation of the Position of the Sun", *Search*, 2(5), pp.172, (1971).

Steinfeld, J. I., Coy, S. L., Herzog, H., Shorter, J. A., Schlamp, M., Tester, W. and Peters, W. A., "High-Flux Solar Photon Processes: Opportunities for Applications", The National Renewable Energy Laboratory, (1992).

Stine, W. B. and Harrigan, R. W., *Solar Energy Fundamentals and Design with Computer Applications*, John Wiley & Sons, (1985).

Stone, K.W. and Jones, S.A., "Analysis of Solar Two Heliostat Tracking error sources", *Proceedings of the ASME International Solar Energy Conference*, (1999).

Titan, "Solar Trackers for all Technologies", [online], Available at: http://www.titantracker.com, [accessed 23 January 2015].

Trefilov, I.V., Schur, D.V., Pishuk, V.K., Zaginaichenko, S. Yu., Choba, A.V., Nagornaya, N.R., "The Solar Furnaces for Scientific and Technological Investigation", *Renewable Energy*, 16(1-4), pp.757-760, (1999).

Wendelin, T., Dobos, A. and Lewandowski, A., "SolTrace: A Ray-Tracing Code for Complex Solar Optical Systems", National Renewable Energy Laboratory, (2013).

Woolf, H. M., "On the Computation of Solar Elevation Angles and the Determination of Sunrise and Sunset Times", National Aeronautics and Space Administration Report NASA TM-X-164, (1968).

Yilmaz, I. H. and Söylemez, M. S., "Thermo-mathematical Modeling of Parabolic Trough Collector", *Energy Conversion and Management*, 88, pp.768-784, (2014).

APPENDIX: VHB™ 4959 DATA SHEET